ABSTRACT

DEVELOPMENT OF X-RAY HOLOGRAPHY METHODS FOR STRUCTURE DETERMINATION: APPLICATION OF HIGH SPEED DETECTORS AND NOVEL NUMERICAL METHODS

by
Yuhao Wang

Holographic methods show much promise to enable direct determination of atomic structure with minimal assumptions and approximations. The approach can, in principle, provide three dimensional information on atomic positions. However, significant developments in experimental techniques, instrumentation and in data collection and analysis are needed. A review of the holography method is given with a focus on X-ray fluorescence holography. Methods for analysis of X-ray holographic data are also reviewed. An overview of the detectors relevant to X-ray measurements is also presented. An experimental apparatus for rapid acquisition of X-ray holographs using novel X-ray detectors has been developed. The integration of high speed detectors and the utilization of rapid sampling methods to produce high quality holograms form the core of this work. A new method for direct extraction of the electron charge density based on expansion of the hologram with respect to a spherical harmonic basis is developed. This approach attacks the problem of obtaining the electron density from the hologram by the introduction of periodic constraints (fixed unit cells) while maintaining flexibility by making no assumptions about the positions of atoms within the unit cells. Problems with local or long range distortions can be solved by utilizing cells of the appropriate size. The method makes no other assumptions. Model charge densities derived from this approach are shown to match quite well with the input model crystal structures with no need for heavy filtering typical of the Barton Transform. The

algorithm can be fully automated and hence falls into the class of “Direct Methods”. This new approach may move the method of X-ray holography from the developmental stage to a powerful and routine tool for the solution of single crystal structures relevant to inorganic materials and organic systems.

DEVELOPMENT OF X-RAY HOLOGRAPHY METHODS FOR STRUCTURE DETERMINATION: APPLICATION OF HIGH SPEED DETECTORS AND NOVEL NUMERICAL METHODS

by
Yuhao Wang

A Dissertation
Submitted to the Faculty of
New Jersey Institute of Technology
in Partial Fulfillment of the Requirements for the Degree of
Doctor of Philosophy in Materials Science and Engineering

Interdisciplinary Program of Materials Science and Engineering

January 2012

APPROVAL PAGE

DEVELOPMENT OF X-RAY HOLOGRAPHY METHODS FOR STRUCTURE DETERMINATION: APPLICATION OF HIGH SPEED DETECTORS AND NOVEL NUMERICAL METHODS

Yuhao Wang

Dr. Trevor A. Tyson, Dissertation Advisor — Date
Distinguished Professor of Physics, NJIT

Dr. Jianming Bai, Dissertation Co-Advisor — Date
Research Assistant Professor of Materials Science and Engineering,
University of Tennessee

Dr. Keun H. Ahn, Committee Member — Date
Assistant Professor of Physics, NJIT

Dr. Onofrio L. Russo, Committee Member — Date
Associate Professor of Physics, NJIT

Dr. Zhen Wu, Committee Member — Date
Professor of Physics, Rutgers University, Newark, NJ

BIOGRAPHICAL SKETCH

Author: Yuhao Wang

Degree: Doctor of Philosophy

Date: January 2012

Undergraduate and Graduate Education:

- Doctor of Philosophy in Material Science and Engineering,
  New Jersey Institute of Technology, Newark, NJ, 2012

- Master of Science in Material Science and Engineering,
  The Chinese University of Hong Kong, Hong Kong, P. R. China, 2005

- Bachelor's degree in Physics,
  Beijing University, Beijing, P. R. China, 2003

- Bachelor's degree in Computer Science,
  Beijing University, Beijing, P. R. China, 2003

Major: Material Science and Engineering

Presentations and Publications:

Yuhao Wang, Jianming Bai and Trevor A. Tyson, "Considerations in the Reconstruction of 3D Atomic Structure from X-ray Holography", 2008 March Meeting of American Physical Society, New Orleans, Louisiana, March 2008

Yuhao Wang, Jianming Bai and Trevor A. Tyson, "New Method for Inverting X-ray Holographs", 2009 March Meeting of American Physical Society, Pittsburgh Pennsylvania, March 2009

Yuhao Wang, Jianming Bai and Trevor A. Tyson, "X-ray Fluorescence Holography with a Novel Energy Resolving Detector", 2010 March Meeting of American Physical Society, Portland, Oregon, March 2010

Yuhao Wang, Jianming Bai and Trevor A. Tyson, "Direct Extraction of Quantitative Structural Information from X-ray Fluorescence Holograms Using Spherical Harmonic Analysis", submitted to Physical Review Letters

For
My Parents

ACKNOWLEDGMENT

I would like to thank Dr. Trevor A. Tyson for his enormous efforts taking care of my project and research during all the five years of my Ph.D.'s study. I had relied everything on Dr. Trevor A. Tyson's help that guided me though my 5 years study. Nothing would be possible if it was not with Dr. Tyson's support and guidance. I would also like to thank Dr. Jianming Bai for his patient and detailed instructions that made a difference in my research. Dr. Jianming Bai is a mentor, who did not only give me advice but also showed to me how to carry-out research in practice. It is Dr. Jianming Bai's deep understanding in the area of X-ray fluorescence holography that has enabled much of the advances that we have made. Also, the work in this thesis would not have been possible without the strong collaboration and assistance on the development and use of high count rate detectors provided by Dr. Peter D. Siddons of Brookhaven National Laboratory. The tight collaboration gave me the chance to access the methods and techniques used in construction of our state of art X-ray detectors. Dr. Peter D. Siddons allocated countless invaluable research resources to my research and guided me step by step while I was trying to construct the silicon X-ray detector used in this research. I would also like to thank Dr. Nuggehalli M. Ravindra for editorial assistance on this thesis.

My colleagues Auther Li, Haiyan Chen, Peng Gao, Tao Wu, Tian Yu all helped me and contributed to my research in many aspects.

This work is supported by National Science Foundation (NSF) Material Research Instrumentation Grant DMR-0722730.

TABLE OF CONTENTS

TABLE OF CONTENTS
(Continued)

Chapter **Page**

TABLE OF CONTENTS
(Continued)

Chapter **Page**

TABLE OF CONTENTS
(Continued)

Chapter **Page**

TABLE OF CONTENTS
(Continued)

Chapter **Page**

TABLE OF CONTENTS
(Continued)

Chapter **Page**

LIST OF TABLES

LIST OF TABLES
(Continued)

Table **Page**

LIST OF FIGURES

LIST OF FIGURES
(Continued)

LIST OF FIGURES
(Continued)

Figure **Page**

LIST OF FIGURES
(Continued)

LIST OF FIGURES
(Continued)

LIST OF FIGURES
(Continued)

LIST OF FIGURES
(Continued)

LIST OF SYMBOLS

$\chi(\vec{k})$	Normalized X-ray Fluorescence Holograph
r_e	Classical Electron Radius
$\boldsymbol{\epsilon}$	Direction of the Electric Field in X-ray
k	Wave Vector of X-ray
C. C.	Complex Conjugate
$\rho(\vec{r})$	Electron Density
c_{lm}	Spherical Harmonic Coefficients of $\chi(k^{\rightarrow})$
$A_{sf}(\vec{k}, \vec{r_1})$	Atomic Scattering Factor
$\mu(r)$	Sample Size Distribution Function
$T_{\boldsymbol{r_0}}^{\boldsymbol{k}}$	XFH Transformation Matrix
$Lorenz(\hat{r}, \hat{k})$	Lorentz Factor for X-ray Scattering
$U(r)$	XFH Reconstruction Image
I	Intensity of XFH Diffraction Pattern
SSD	Solid State Detector
SDD	Silicon Drift Detector
PDD	Peak Detector/Derandomizer
PD/TACs	Peak Detectors/Time-to-Amplitude Converters
S/N	Signal to Noise Ratio

CHAPTER 1

REVIEW ON X-RAY FLUORESCENCE HOLOGRAPHY

1.1 Early History of Holography

Holography is a two-step method involving first recording a diffraction pattern from an object with photons or electrons, and second reconstructing the object image with the diffraction pattern. The first hologram was produced in 1947 by Physicist Dennis Gabor (Figure 1.1) as an unexpected result of research into improving electron microscopy [1]. Gabor received the Nobel Prize in Physics for this work in 1971. The technique is now known as electron holography and is still used in electron microscopy [1].

Figure 1.1 Photograph of Dennis Gabor.
Source: [2]

Figure 1.2 is the illustration of Gabor's original technique for electron holography, where he put the sample under a coherent electron beam to record the Fresnel diffraction pattern directly. A detailed discussion of electron holography is presented later in this review.

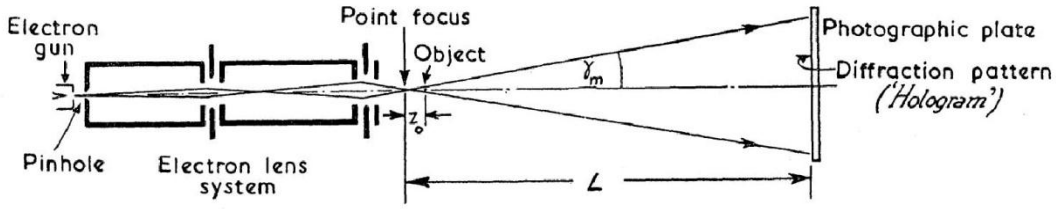

Figure 1.2 Technique of electron holography Gabor proposed in his original work.

Source: [1]

Early holography based on optical light was advanced in 1960's when lasers became available. The first optical holography that recorded 3D images was made in 1962 by Denisyuk [3] and also by Leith and Upatnieks [4].

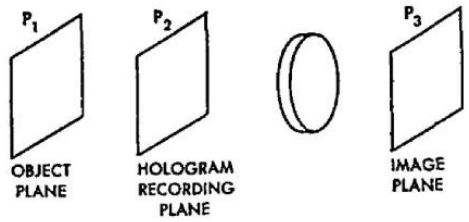

Figure 1.3 Optical holography setup.

Source: [4]

Figure 1.3 is the setup of optical holography from Reference [4]. The hologram plane records the Fresnel diffraction pattern from the object plane where no lens is required. Light transmitted from the holograph plane is then reconstructed with ordinary lenses to from the real image.

The theory of holography is explained in detail in Reference [4]. When coherent light from the laser shines upon the object plane, the light amplitude at the object plane is:

$$s\exp(i\omega t) = [S_b + S_r(x,y)]\exp(i\omega t) \qquad (1.1)$$

Where s is the overall amplitude, s_b is the background amplitude of the laser, s_r is the scattered wave from the object plane.

At the hologram plane, a Fresnel pattern is formed from the object plane due to signal in s_r.

$$\chi(x,y) = S_b + i(\lambda z)^{-1} \iint S_r(\alpha,\beta) exp\left[-i2\pi\lambda^{-1}\sqrt{z^2 + (x-\alpha)^2 + (y-\beta)^2}\right] d\alpha\, d\beta$$
$$= S_b + S_r * f \tag{1.2}$$

where z is the position of the hologram plane. The * operation denote convolution, as shown in Equation 1.3:

$$(f * g) = \int_{-\infty}^{\infty} f(T) g(t-T) dT \tag{1.3}$$

where f is given by $exp\left[-i2\pi\lambda^{-1}\sqrt{z^2 + (x-\alpha)^2 + (y-\beta)^2}\right]$.

The wave amplitude is recorded on the hologram plane by photographic methods, while phase information is lost in the recording process. The recorded amplitude represents the function:

$$\chi\chi^* = [S_b + S_r * f][S_b + S_r * f]^*$$
$$= |S_b|^2 + S_b{}^*(S_r * f) + S_b(S_r * f)^* + |S_r * f|^2 \tag{1.4}$$

Reconstruction of the hologram in [4] was done by coherent light illuminating the hologram, producing $S_b{}^*(S_r * f)$ and $S_b(S_r * f)^*$ wave front on the hologram plane. The wave front is a reconstruction of the light wave in the original optics and can be focused by lenses to form a real image on the image plane.

The method as shown in Figure 1.3 is also called in-line holography [4]. For that, all optical components are arranged on a single optical axial. In-line holography suffers a twin image problem that both $S_b{}^*(S_r * f)$ and $S_b(S_r * f)^*$ terms in reconstructed image

overlap each other and result in blurred image. Leith et al. had also discussed an off axis holography method [4], where $S_b{}^*(S_r * f)$ and $S_b(S_r * f)^*$ are separated in space to avoid blurring.

Figure 1.4 is an illustration of off line holography. Back ground wave s_b and object wave

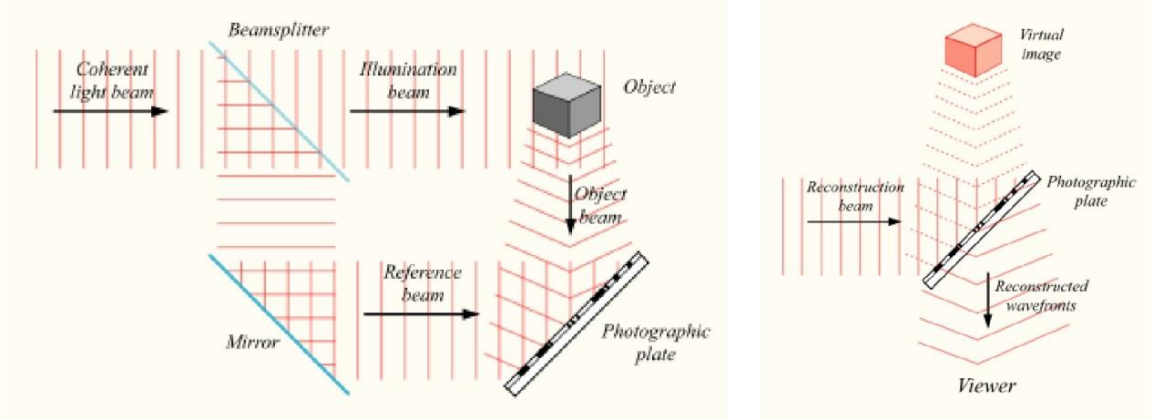

Figure 1.4 Method of recording holograms from an object (left) and reconstructing holographic image (right).

Source: [5]

$S_r * f$ are placed on different optical axes and interference at holography plate. When reconstructed, $S_b{}^*(S_r * f)$ and $S_b(S_r * f)^*$ do not overlap. The background wave S_b is also controlled to have comparable magnitude with the object wave sr. So that $S_b{}^*(S_r * f)$ and $S_b(S_r * f)^*$ are comparable to $|S_b|^2$ term. The hologram has better contrast than in-line holography. For more detailed review of many setups for off-line holography, see References [6-8].

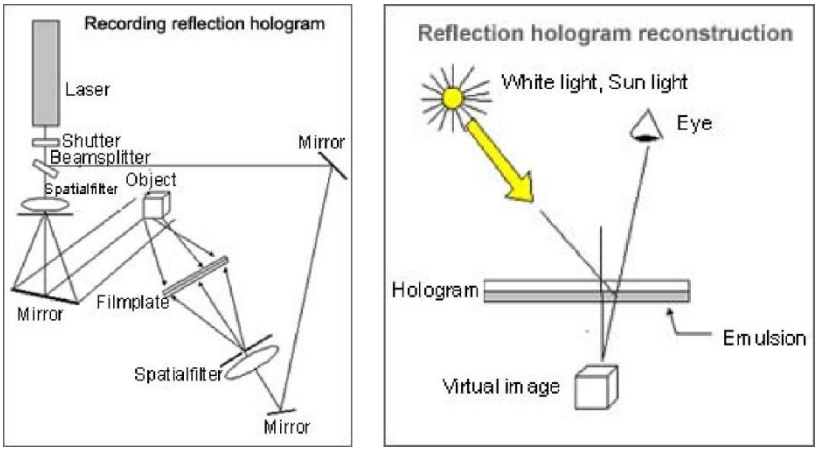

Figure 1.5 Method for recording hologram in reflection holography (left) and reconstructing holographic image in reflection holography (right).

Source: [9]

Figure 1.5 shows the method of recording and reconstructing hologram in reflection hologram scheme, proposed by Denisyuk in 1963 [10]. While recording, object wave S_r is placed on the opposite direction of the reference wave S_b and the two waves produce maximum contrast in interference pattern, allowing easier recording of holograph pattern [10]. If the hologram is made of reflective material, the hologram can also be reconstructed by reflected light, using white light as illumination. This type of holography is often mentioned as 'colored holography' for multi-colored image are made possible with this scheme. For more detailed introduction of colored holography and its application, refer to [7].

Figure 1.6 is a sample reconstructed high quality holograph image taken in 1976 when high quality photographic films became available [11].

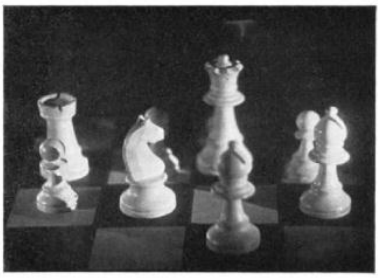

Figure 1.6 A sample holograph image.
Source: [11]

1.2 Electron Holography in TEM

Although electron holography was presented as early as in Gabor's 1947 paper [1], its development was much slower than optical holograph. Theory of electron holography is described with the same equations as of the optical holography except that the hologram was formed with an electron beam.

Gabor's original proposal of electron holography was aimed at improving resolution by using no optics other than the electron gun and the object, as shown in Figure 1.2, thus avoiding distortion from the imperfect electron optics at that time. The lack of strong coherent electron source made this method impractical. In 1950, Haine and Dyson proposed a transmission method of electron holography [12], which inserted electron optics in between the object and photographic plate, which is optically equivalent to the setup in Figure 1.3, but 12 years earlier. This set up is more easily achievable and requires less intensity from the coherent electron source. The twin image problem of the in-line setup of transmission mode is minimized by recording the hologram in the Fraunhofer condition, where $z >> d/\lambda^2$, z is distance from the object to photographic plate, and d is distance from object to electron source, as proposed by Thompson et al. in 1966 [13], The first examples of successful application of 3D reconstructions using TEM were published in 1968 [14-16].

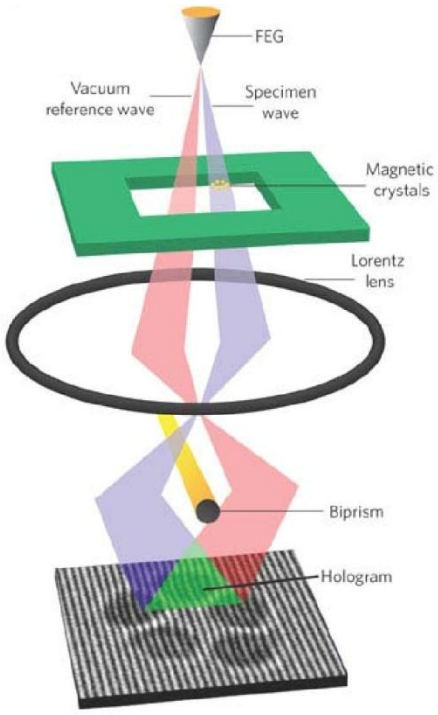

Figure 1.7 An illustration of the image-plane off-axis holography setup in modern TEM. Source: [17]

For the period before the late 1980's, research with electron holography was limited to a handful of groups who were very experienced with coherent electron sources, until the emergence of the field emission gun. Development of electron holography method was slow but steady, namely about 20 different holographic scheme have been proposed, and reviewed by Cowley at 1992 [18]. While most of the holography schemes were less intensively studied, the most popular setup used for contemporary electron holography by far is image-plane off-axis holography. Figure 1.7 is an illustration of this setup as used in Midgley et al.'s paper in 2009 [17].

The arrival of the commercial TEMs with field emission guns in early 1990's greatly enabled research with electron holography into research group worldwide. Field emission guns provided coherent electron beams with enough brightness sufficient for

many holographic studies to be performed in ordinary TEMs. In Figure 1.7, the coherent electron beam is emitted from the field emission gun and split into a reference wave and specimen wave. The spacemen wave component transmits through the spacemen and then both beams are focused by Lorentz lens and brought together with a Mollensted-Duker biprism. These two waves form an interference pattern at photographic plate.

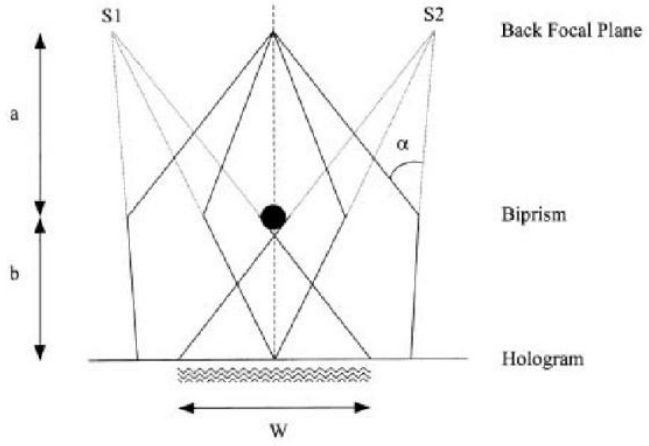

Figure 1.8 Role of biprism in hologram.
Source: [19]

Figure 1.8 is an illustration of the role that the biprism plays in holography, the picture is taken from Midgley's review paper of electron holography in 2001 [19]. The biprism is a thin glass fiber coated with metal, and mounted on a biprism mounter in TEM optics. The mounter allows charging in the biprism with positive and negative bias, and allows adjustment of the biprism position both translational and rotational. The bias voltage in the biprism bends the electron beams for both reference wave and spacemen wave thus is the equivalent of an optical biprism. The position of the electron source is displaced to position S1 and S2, and their beam interference under the biprism. Adjustment of bias voltage and position of the biprism affect the deflection angle.

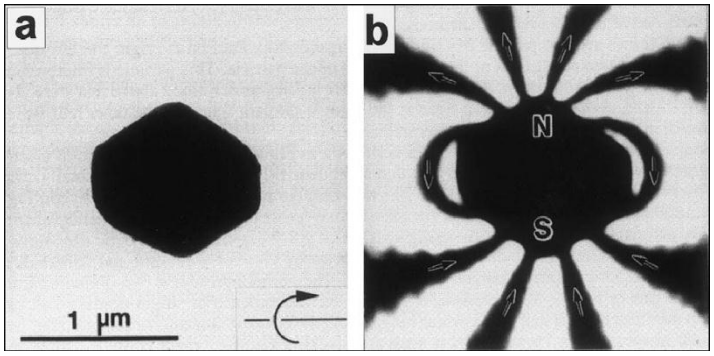

Figure 1.9 Bright field image (left) and interference micrograph (right) showing the magnetic flux linkage from a barium ferrite particle in a single domain state.

Source: [20]

Electron holography is especially suitable for observing phase contrast in spacemens, i.e. electric and magnetic fields that could not be detected easily by conventional electron microscopy. Figure 1.9 is a comparison of bright field image and interference in electron holography showing magnetization in a barium ferrite particle.

Figure 1.10 is the result of direct observation of Aharonov-Bohm (AB) effect with electron holography as reported by Tonomura in 2005 [21]. The shift of interference fringes in the center space shows a phase difference as compared with the outer-space. The phase contrast comes from pure quantum effects but not electric or magnetic fields.

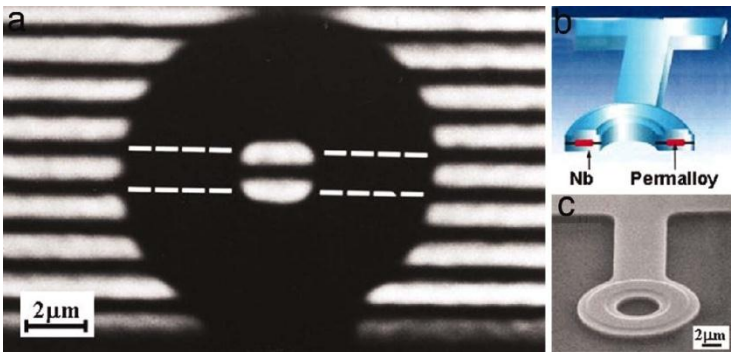

Figure 1.10 Direct observation of Aharonov-Bohm (AB) effect with electron holography.

Source: [21]

For more example applications and observations with electron holography, see Midgley's review [19].

1.3 Photoelectron Holography, Holographic LEED and Holographic Interpretation of Other Diffraction Patterns

While the field emission gun has provided expanded availability of the electron holography in late 1980's, several common interference patterns, which do not involve the use of coherent electron source, have also gained interest and have been interpreted as holographic interference. Soceke [22] first suggested electron microscopy by photoelectrons or Auger decay electrons. Then, Barton [23] suggested in theoretical analysis that intensity distributions of photoelectrons from a single crystal surface can be considered to be a hologram.

The method of photoelectron holography makes use of the coherent property of photo-electrons, when photo emitted electrons find more than one way of arriving at a photographic plate, an interference pattern called photoelectron diffraction arise. The theory and experimental method was suggested early in 1974 by Liebsch [24] as shown in Figure 1.11. When photoelectrons are emitted from single crystal surface, strong diffraction occurs at Bragg like condition, i.e. $2a \cdot \sin\theta_f = n\lambda$. The diffraction occurs not because photoemission from different atoms is coherent, but because the photoelectron is scattered by local environment of the emitter and strong interference between scattered wave and the direct photoelectron wave occurs.

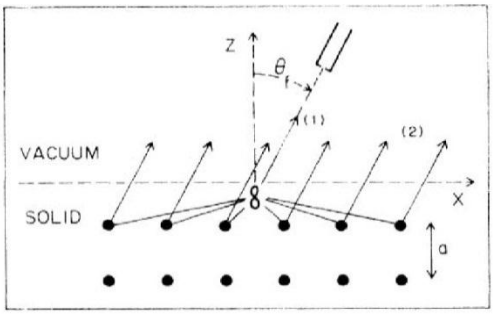

Figure 1.11 Method to record angular resolved photoelectron diffraction.
Source: [24]

Barton explained the phenomena as a hologram, where the photoelectron wave is a coherent reference wave and the electron scattered by the emitter's local environment is the object wave:

$$\Psi = \Psi_b + \sum_j \Psi_{s,j} \tag{1.5}$$

where Ψ_b is photoelectron wave as background reference wave. $\Psi s,j$ is the scattered wave from j^{th} atom. Rewrite $\Psi_{s,j}$ in detail, one has:

$$\Psi = \Psi_b + \sum_j \left[F_j exp\left(ikr_j - i\boldsymbol{k}\cdot\boldsymbol{r_j} + i\phi_j\right)\right] \tag{1.6}$$

Consider Ψ is proportional to the background wave, where F_j and φ_j are the amplitude and phase part of scattering factor of the j^{th} atom respectively. Thus one has:

$$\Psi = \Psi_b \left[1 + \sum_j \left[F_j exp\left(ikr_j - i\boldsymbol{k}\cdot\boldsymbol{r_j} + i\phi_j\right)\right]\right] \tag{1.7}$$

$$\begin{aligned} I &= \Psi \times \Psi^* / \left(\Psi_b \cdot \Psi_b{}^*\right) \\ &= 1 + \sum_j \left[F_j exp\left(ikr_j - i\boldsymbol{k}\cdot\boldsymbol{r_j} + i\phi_j\right)\right] + \sum_j \left[F_j exp\left(-ikr_j + i\boldsymbol{k}\cdot\boldsymbol{r_j} - i\phi_j\right)\right] \\ &\quad + \sum_{ij} \left[F_i exp(ikr_i - i\boldsymbol{k}\cdot\boldsymbol{r_i} + i\phi_i)\cdot F_j exp\left(-ikr_j + i\boldsymbol{k}\cdot\boldsymbol{r_j} - i\phi_j\right)\right] \end{aligned} \tag{1.8}$$

where, I is the intensity of photoelectron diffraction pattern. The equation is virtually a Fourier transform of the local atomic structure. The last term is neglected in the weak scattering limit. A numerical inversion of I–1 could reveal the position of local scatters.

$$U(r) = \iint_s (I-1)exp(\mathrm{i}\boldsymbol{k}\cdot\mathbf{r})d\Omega_k \tag{1.9}$$

This numerical method of reconstructing the hologram is commonly referred as Barton's algorithm. Soon after Barton's statement of holography with photoelectrons, other common interference phenomena were also studied as holograms. Saldin proposed interference from LEED as a holograph [25], traditional electron holography with a field emission gun placed very close to spacemen is also proposed at 1990 [26], the method of tradition electron holography was very similar to photoelectron holograph.

The first successful experimental reconstruction of photoelectron holography was presented in 1989 by Hong Li and Tonner [27]; Harp et al. gave the first Auger-electron diffraction holography at 1990. Figure 1.12 is auger-electron holography and reconstructed image of Cu (100) surface in Harp et al.'s report [15, 28].

The method of photoelectron holography is an in-line holographic method that suffers from the problem of twin images. In the recorded holograph, the second two terms in Equation 1.8, $\sum_j\left[\mathrm{F}_j exp\left(ikr_j - \mathrm{i}\boldsymbol{k}\cdot\boldsymbol{r_j} + i\phi_j\right)\right] + \sum_j\left[\mathrm{F}_j exp\left(-ikr_j + \mathrm{i}\boldsymbol{k}\cdot\boldsymbol{r_j} - \mathrm{i}\phi_j\right)\right]$ add on top of each other. The numerically reconstructed image will contain both images from the $\sum_j\left[\mathrm{F}_j exp\left(ikr_j - \mathrm{i}\boldsymbol{k}\cdot\boldsymbol{r_j} + i\phi_j\right)\right]$ term and the $\sum_j\left[\mathrm{F}_j exp\left(-ikr_j + \mathrm{i}\boldsymbol{k}\cdot\boldsymbol{r_j} - \mathrm{i}\phi_j\right)\right]$ term.

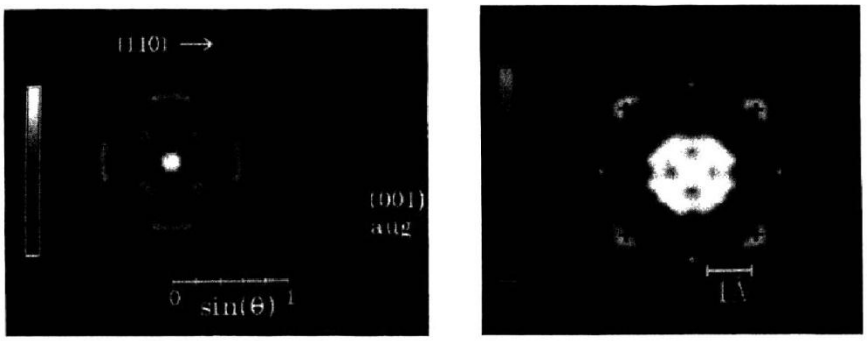

Figure 1.12 Auger electron holography measured on Cu (100) surface (left) and reconstructed image of the hologram with atomic resolution (right).

Source: [28]

In 1991, Barton [23] suggested the twin image problem can be solved by using multiple energy photoelectrons. The reconstructed image for single energy photoelectron holography is given by:

$$U(r) = \frac{1}{2\pi R^2}\iint_s (I-1)exp(\mathrm{i}\boldsymbol{k}\cdot\mathbf{r})d\Omega_k$$
$$= \frac{1}{2\pi R^2}\sum_j \iint_s \mathrm{F}_j\left[\exp(ikr)exp\left(-\mathrm{i}\boldsymbol{k}\cdot\boldsymbol{r_j}+\mathrm{i}\boldsymbol{k}\cdot\mathbf{r}\right)+\exp(-ikr)exp\left(\mathrm{i}\boldsymbol{k}\cdot\boldsymbol{r_j}+\mathrm{i}\boldsymbol{k}\cdot\mathbf{r}\right)\right]d\Omega_k$$
$$= \frac{1}{2\pi R^2}\sum_j \mathrm{F}_j\left[\exp(ikr)\delta\left(\boldsymbol{r}-\boldsymbol{r_j}\right)+\exp(-ikr)\delta(\boldsymbol{r}+\boldsymbol{r_j})\right] \quad (1.10)$$

Where the $\delta(r - r_j)$ term is the reconstructed image and $\delta(r + r_j)$ is the twin image. Barton suggested that holograms with multiple electron energies should be taken and combined to rebuild the real space image:

$$U(r) = \frac{1}{2\pi R^2}\sum_k \exp(-ikr)\iint_s (I-1)exp(\mathrm{i}\boldsymbol{k}\cdot\mathbf{r})d\Omega_k$$
$$= \frac{1}{2\pi R^2}\sum_k \iint_s \sum_j \mathrm{F}_j\left[exp\left(-\mathrm{i}\boldsymbol{k}\cdot\boldsymbol{r_j}+\mathrm{i}\boldsymbol{k}\cdot\mathbf{r}\right)+\exp(-2ikr)exp\left(\mathrm{i}\boldsymbol{k}\cdot\boldsymbol{r_j}+\mathrm{i}\boldsymbol{k}\cdot\mathbf{r}\right)\right]d\Omega_k$$
$$= \frac{1}{2\pi R^2}\sum_j \mathrm{F}_j\left[\delta\left(\boldsymbol{r}-\boldsymbol{r_j}\right)+\sum_k \exp(-2ikr)\,\delta(\boldsymbol{r}+\boldsymbol{r_j})\right] \quad (1.11)$$

For a large number of different energies, the $\sum_k \exp(2ikr)\delta(\boldsymbol{r}+\boldsymbol{r_j})$ twin image term will tend to cancel each other and result in much lower intensity than the real image. The introduction of multiple energy holographs have greatly improved the quality of reconstructed image in photoelectron holography. Tong et al. first realized a high quality reconstructed image of multiple energy holography [29]. Figure 1.13 is the image of Co monolayer of atoms on Cu (111) surface from Tong's report.

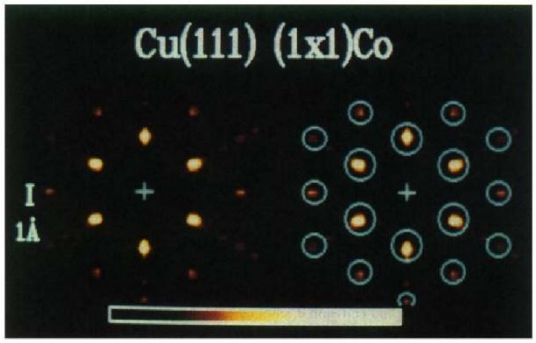

Figure 1.13 Image of Co monolayer as reconstructed by multiple energy holographs. Source: [29]

Despite the success of multiple energy holographs, photoelectron holography has many limitations. Electron have strong interaction with matter, and the single scattering or weak scattering assumption is too crude to fit experimental data. Strong interaction also results in very anisotropic scattering, resulting in forward-peaked scattering factor. Many efforts have been devoted to study these limitations after photoelectron holography was born. Thevuthasan et al. [30] have reported both multiple scattering and forward peaked scattering could result in 0.5-1.0 Å distortion of reconstructed real space image. An algorithm to compensate the anisotropic scattering factor before reconstruction is shown to improve image quality and reduce distortion [30, 31]. Tong et al. also reported distortions caused because of phase-shifts when electron is scattered [32], and different

methods to correct the phase-shift distortions are also reported [32-34]. Special algorithms to correct the distortion from multiple scattering are also reported [35].

The many corrections required in photoelectron holography have made it hard to determine the accuracy and noise level in reconstructed real space images. Since many problems have arisen from strong interaction between the electrons and atoms, consideration of using X-ray photons to replace electrons as interference media became more attractive.

In 1991, Tegze et al. [36] first studied from a theoretical perspective the possibility of holography using X-ray fluorescence photons. Len et al. [37] have a comparative study about the strength and weakness of X-ray fluorescence holography and electron-emission holography. The weak interaction of photons with materials makes it ideal for holographic structure study, but the experimental requirements are much more stringent.

1.4 The Development of X-ray Fluorescence Holography

X-ray Florescence Holography is a relatively new technique for structural studies with sub-atomic resolution. In 1988, Barton [23] suggested using photoelectron diffraction as atomic scale holography and gave the Fourier transformation's algorithm for real space reconstruction. Holographic techniques with electrons as the imaging wave was first studied and realized in early 1990s [25, 28]. Compared to electron, X-ray has weaker interaction with matter. Thus X-ray holography suffers from less distortion from wave-material interaction, but the diffraction pattern is less intense and more difficult to measure. As powerful synchrotron X-ray sources became available in recent years, X-ray fluorescence holography is becoming practical and efficient. In 1996, Tegze et al. [38]

first realized a X-ray holography using the inside source scheme and Gog et al. [39] realized a multiple energy X-ray holography with the inside detector scheme. As synchrotron X-ray sources were rapidly developed from 1990's. X-ray holography soon attracted attention from many research groups. Figure 1.14 is an example reconstructed image of a NiO sample with image of oxygen observable.

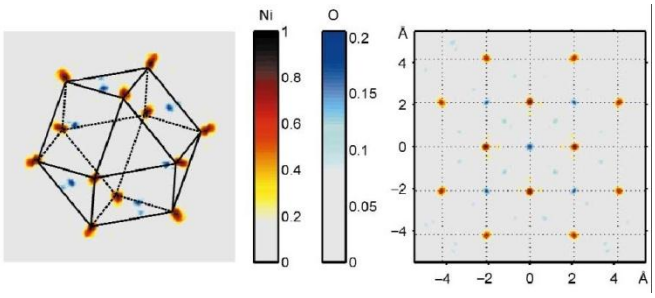

Figure 1.14 An example reconstructed image of NiO.

Source: [40]

1.4.1 Inside Source and Insider Detector

Figure 1.15 illustrates experimental setup schemes for inside source and inside detector methods. The pictures are taken from Gog's paper [39]

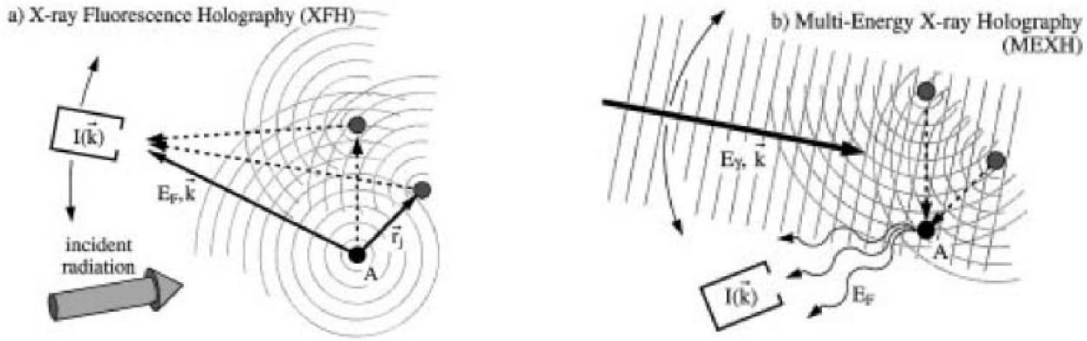

Figure 1.15 Illustration of the inside source scheme (left) and inside detector scheme (right).

Source: [39]

In the inside source scheme, the incident radiation beam passes through at fixed position relative to sample. The detector is scanned across all available solid angle for the fluorescence energy. The measured signal from this setup will be interference pattern from unscatterd florescence X-rays and florescence X-rays scattered by atoms in the neighborhood of the absorbers.

In the inside detector scheme, the measuring X-ray detector is placed in fixed direction relative to the sample, while the incident beam is scanned across all available solid angle. Since the X-ray field intensity on the fluorescent center depends on interference of incident beam and scattered beam from sample structure, the emitted florescence will be an indication of the interference pattern. Thus the florescent center is used as a detector of X-ray field intensity in the interference. The benefit of using the inside detector scheme is that it allows for using multiple energy X-rays as the interference wave, rather than only the florescent wavelength of the exited atom for the inside source scheme. Another notable difference is that inside source scheme is interference of unpolarized X-ray while inside detector scheme usually uses polarized X-ray from synchrotron.

For either case and with reasonable approximation, the interference pattern for X-ray can be written as:

$$\chi = r_e \iiint \rho(\boldsymbol{r}) \cdot Lorenz(\hat{r}, \hat{k}) \frac{\cos[kr(1 - \hat{r} \cdot \hat{k})]}{r} d\boldsymbol{r} \qquad (1.12)$$

Where $\rho(r)$ is the electron density of the local structure inside the sample, r_e is electron scattering cross section. $Lorenz(\hat{r}, \hat{k})$ is the Lorentz factor for X-ray scattering depend on polarization of the incident beam. The detail of the above equation is explained in the following sections

For polarized X-ray radiation:

$$Lorenz(\hat{r}, \hat{k}) = 1 - (\boldsymbol{\epsilon_k} \cdot \hat{r})^2 \tag{1.13}$$

Where $\boldsymbol{\epsilon_k}$ is unit vector for electric field in X-ray polarization.

1.4.2 Reconstruction

Numerical reconstruction algorithms were given as early as Barton's paper in 1988 [23]. The algorithm is essentially a Fourier transform and has been widely mentioned as Barton's algorithm. For the reconstruction of single energy holograph:

$$U(r) \propto \iint \chi(\hat{k}) \cdot \exp(\mathrm{i}\boldsymbol{k} \cdot \mathbf{r})\, d\Omega_k \tag{1.14}$$

Gog proposed reconstruction algorithm for the multiple energy X-ray holography in his 1996 paper [39], given by:

$$U(r) \propto \sum_k \exp(-ikr) \iint \chi(\hat{k}) \cdot \exp(\mathrm{i}\boldsymbol{k} \cdot \mathbf{r})\, d\Omega_k \tag{1.15}$$

1.5 Theoretical Considerations and Simulations

X-ray signals measured in the detector are a sum of three terms: the florescence wave squared, the scattered wave squared, and the interference term from the florescence wave and scattered wave. The reason that X-rays have been preferred over electron holography is that X-ray has small interaction with mater and thus the scattered wave is very small compared to fluorescence wave itself. For small crystalline sample, the florescence wave square is uniform and much larger than the other term. The scattered wave squared term is negligible when compared to the interference term. Thus any pattern in the detected signal can be approximately considered to be the interference pattern itself.

For very large crystalline samples however, multi scattered X-ray waves became dominant and dynamic diffraction theory is the method need to describe the behavior of the scattering. In this case, the square of scattered wave can be larger than the interference pattern. Patterns from X-ray detectors may not be a close approximation of the interference pattern

1.5.1 Absorption

In a real X-ray experiment, the X-ray signal is damped when it travels in a material. The damping is caused by atomic absorption of the photons. Figure 1.16 is the absorption spectra of X-rays in CuAu [41]. As a result, the further a scattering center is located from the emitter, the lower the intensity of diffraction pattern the scatter contributes to the holograph.

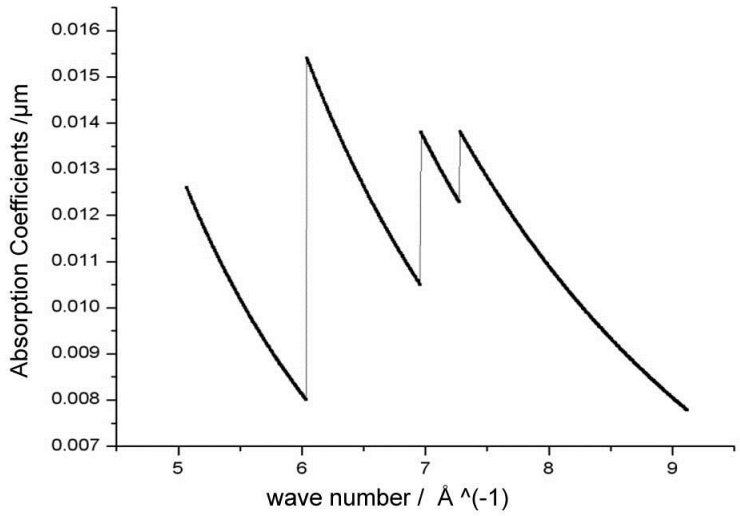

Figure 1.16 Absorption spectra of X-ray in CuAu.

Thus the hologram can be rewritten as.

$$\chi = r_e \iiint \rho(\boldsymbol{r}) \cdot Lorenz(\hat{r}, \hat{k}) \frac{\cos\left[kr\left(1 - \hat{r} \cdot \hat{k}\right)\right]}{r} \exp(-\delta r) d\boldsymbol{r} \qquad (1.16)$$

Where δ is the damping factor as the X-rays travel from emitter to scatter. When multiple energy X-ray holography schemes are employed, different wave lengths have different damping factors. If only the emitter's local environment is concerned, the difference caused by damming is negligible. If the far field environment is considered, the difference of damping can be used to distinguish the far field holographic signal from the local field. In 2001 Omori et al. used the difference in absorption power at different wavelength to selectively image Fe and Ne atoms in XFH experiment [42]. They have named this the Resonant X-ray Fluorescence Holography (RXFH) method.

Figure 1.17 is the Figure from Omori's report [42] showing the structure of the FeNi specimen, as compared to image from multiple energy X-ray holograph, and image from the RXFH method. While MEXH is showing only electron density in the emitter's environment, RXFH distinguishes Fe and Ni atoms by their different X-ray absorption.

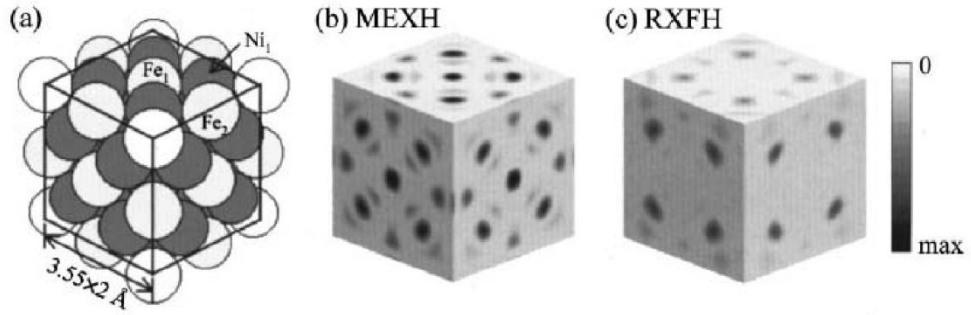

Figure 1.17 Structure of FeNi specimen (a), image from MEXF (b) and image from RXFH (c).

Source: [42]

Takahashi et al. [43] also proposed a method, in simulations, to utilize the RXFH method with three energies around the scatter's absorption edge. The method provides an alternative method to solve the twin image problem other than the multiple energy method.

1.5.2 Standing Waves

Multiple scattering for X-ray is much smaller than electrons in materials. Yet careful discussion of its influence has been presented by many research groups. Korecki et al. [44] have given a focused discussion on extinction effect in XFH imaging in 2004. Several papers discussed the possibility of removing the effect of standing wave by applying a low pass filter to hologram before reconstruction [45-48].

In 2002 Kopecky et al. reported X-ray holography measured by transmission mode [49, 50]. However the measured signal can be dominated by standing waves with this method [50]. Figure 1.18 is the illustration of Kopecky's X-ray absorption holograph.

In any case, standing wave or extinction effect is an unwanted part of the holographic signal and should be minimized in a careful experimental setup.

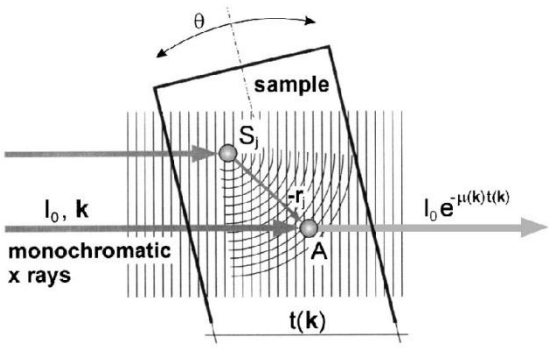

Figure 1.18 Transmission mode X-ray absorption holography.
Source: [49]

1.5.3 Atomic Scattering Factor and Near Field Effect

The expression of the X-ray hologram as a function of electron density $\rho(\boldsymbol{r})$ can also be considered as function of each atom. Thus the following equation is found:

$$\chi = r_e \iiint \rho(\boldsymbol{r}) \cdot Lorenz(\hat{r}, \hat{k}) \frac{\cos\left[kr\left(1 - \hat{r} \cdot \hat{k}\right)\right]}{r} \exp(-\delta r) d\boldsymbol{r} \qquad (1.17)$$

Equation 1.17 can be written in the form:

$$\chi = r_e \sum ASF_r(k, \hat{r}) Lorenz(\hat{r}, \hat{k}) \frac{\cos\left[kr\left(1 - \hat{r} \cdot \hat{k}\right)\right]}{r} \exp(-\delta r) \qquad (1.18)$$

Where $ASF_r(k, \hat{r})$ is the atomic scattering factor for atom at position **r**. The sum is over all scatter atoms. Here the atomic scattering factor represent scattering for electron density associated with an atom. Since X-rays propagate from an emitting center and form a spherical wave before scattering, the atomic scattering factor here is slightly different from the standard atomic scattering factor in XRD experiment. The difference can be simulated accurately in detail. In Bai's report on 2003 [51], the atomic scattering factors from spherical wave are compared with atomic scattering factor in XRD and around 10% to 20% reduction of the scattering power is found to result from the spherical correction to the wave front.

1.5.4 Lorentz Factor, Consideration of Vectorial Nature

Lorentz factor could be a poor approximation when considering spherical wave front of the scattering and the vectorial nature of X-ray. The poor approximation causes about 1% deviation in amplitude from simple models [51-54].

1.6 Special Experimental Methods and Results

Even with powerful synchrotron beams, XFH data acquisition is slow and easily takes up to 10 hours per single energy per sample. An efficient data collecting method is essential to acquire holograms with reasonable quality and resolution. The requirement is more stringent when studying dilute sample or small spacemen. Special experimental

techniques have been employed in XFH experiment. These methods include special monochromatic crystal [55], fast X-ray detector with energy resolution [56], and using filters to replace crystals analyzer [57].

Using special reconstruction methods to reduce required number of multiple energy holography has also been studied. Examples of these method include matrix solving technique [52, 58, 59], and choosing the energy cleverly in MEXH for maximum efficiency in twin image cancelation [60].

1.6.1 Special Monochromatic Crystal

One way of improving data acquisition speed is increasing the acceptance angle which is the solid angle a detector can detect fluorescence photon. Marchesini et al. [61] in 2000, Kouichi et al. [62] in 2005 and Kusano et al. [55] in 2006 all reported using very large monochromatic analyzing crystal that collected fluorescence photons from all possible directions.

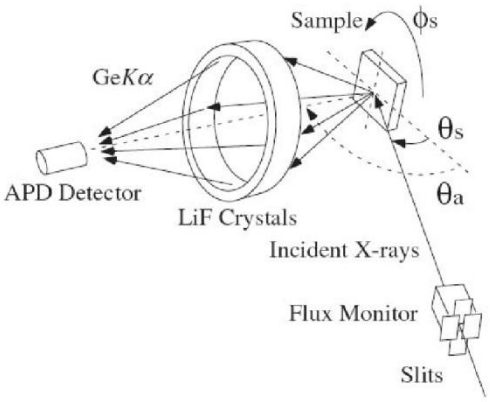

Figure 1.19 Experimental setup with circular monochromatic analyzing crystal in XFH experiment.

Source: [55]

Figure 1.19 is the experimental setup with cylindrical monochromatic analyzing crystal in Kusano et al.'s report [55]. The crystals form a ring and focus fluorescence photons into an avalanche photodiode detector.

1.6.2 Fast X-ray Detector with Energy Resolution

Using a crystal analyzer on the detector side will usually require 1m's distance between sample and detector and thus notably reduces the efficiency for detecting fluorescence photons. One alternative method is using energy dispersive silicon drift detectors [63] at close location to the sample. In 1998, Adams et al. reported measurement of XFH on Cu_3Au sample with energy dispersive silicon drift detectors [56]. The reconstructed real space results from Adams et al. shows copper and gold atoms with great quality. Their hologram may have suffered from elastic scattering signals as noise on top of holographic signal. The Bragg peaks in hologram are low enough, thus do not distort the reconstructed real space image. Figure 1.20 is the hologram and reconstructed image from Adams et al.'s report [56].

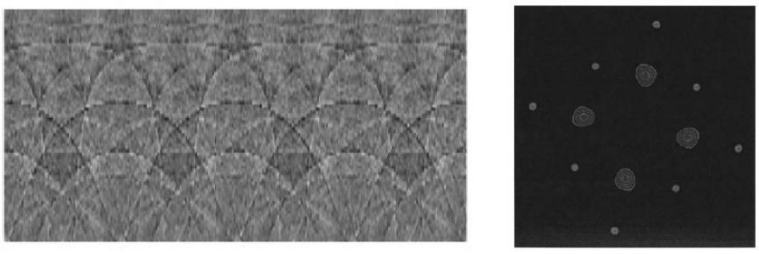

Figure 1.20 Hologram measured from energy dispersive silicon drift detector (left) by Adams et al. and real space image (right) reconstructed from multiple energy holographs.

Source: [56]

1.6.3 XFH with Laboratory X-ray Source

Modern development of laboratory X-ray equipment has resulted in powerful X-ray source that are strong enough to allow for limited XFH measurement without using synchrotron source. Takahashi et al. have successfully demonstrated a XFH measurement on an Au single crystal sample with X-ray source from a 21 kW rotating-anode X-ray generator and A cylindrically bent graphite crystal [64]. A solid state detector with 200 eV energy resolution is used to collect photon counts from sample fluorescence. Mo K_α radiation (17.44 keV) from X-ray generator and Au L_α, L_β, L_γ fluorescence are used to make a multi-energy XFH reconstruction.

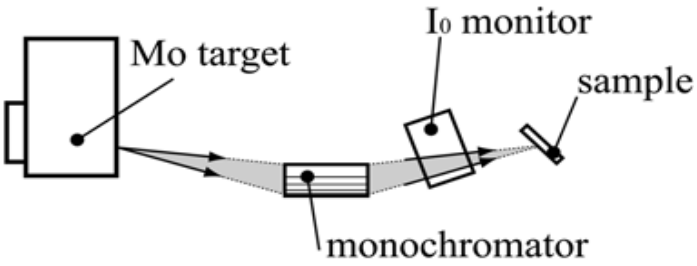

Figure 1.21 Schematic for measuring XFH with laboratory X-ray.
Source: [64]

The demonstration experiment took 10 days to measure 4 holograms on the Au sample. Figure 1.21 is the schematic for measuring XFH with a laboratory X-ray source by Takahashi [64].

1.6.4 Other Special Setups and Summary

Many other special approaches/configurations are being studied in order to improve efficiency and preference in XFH experiment equipment and setup. Table 1.1 is a summary of these special methods.

Table 1.1 Special Techniques used in XFH Experiment

Author	Year	Special Method
Admas et al.	1998	Fast silicon detector with energy resolution [56]
Busetto et al.	2000	Use zinc foil filter to separate Fluorescence from background [57]
Marchesini et al.	2000	Cylindrical crystal analyzer for large acceptance angle[65]
Omori et al.	2001	Resonant XFH selectively image different element [42]
Kouichi et al.	2001	Using multi-element solid state detector (SSD) [66]
Kopecky et al.	2002	Transmission mode X-ray Holography for enhanced contrast [49]
Nishino et al.	2002	Two-energy twin image removal by selected XFH energies [40, 60]
Takahashi et al.	2003	Complex X-ray holography that uses three selected energy to provide resonant XFH with twin image removal [43]
Takahashi et al.	2004	XFH with laboratory X-ray using large bent crystal monochromator [64]

1.7 Advanced Reconstruction Method with Steepest Descent Algorithm

Although the straightforward Fourier transformation method, also known as Barton's algorithm, was accepted as the most popular reconstruction method in many research papers [23, 40, 67], several advanced reconstruction methods attempt to provide better accuracy than the Barton's algorithm.

1.7.1 Modification to Barton's Algorithm

Chukhovshii et al. [52] considered vectorial property in X-ray interference and derived a reconstruction method from Maxwell's equation, taking into account for correction of the Lorentz factor and also polarization effects. The result is an expression of electron density directly formulated from XFH holography [52].

The inverse scheme multi-energy holography with Lorentz factor $Lorenz(\hat{r}, \hat{k}) = (1 + \hat{r} \cdot \hat{k})$ is given by:

$$\chi = r_e Re\left[\int \exp(-i\boldsymbol{k}\cdot\boldsymbol{r})\left(1+\hat{r}\cdot\hat{k}\right)\frac{\exp(ikr)}{r}\rho(r)d\boldsymbol{r}\right] \tag{1.19}$$

The exact solution is obtained, in [52], as:

$$r_e\frac{\rho(r)}{r} = \int\left[\cos(\boldsymbol{k}\cdot\boldsymbol{r}-kr)\left(1+\hat{r}\cdot\hat{k}\right)-\frac{\sin(\boldsymbol{k}\cdot\boldsymbol{r}-kr)}{kr}-2-2\hat{r}\cdot\hat{k}\right]\chi(\boldsymbol{k})d\boldsymbol{k} \tag{1.20}$$

As compared to Barton's method, the exact solution is free from the influence of the Lorentz factor and thus gives more accurate intensity in the electron density.

1.7.2 Scattering Pattern Matrix Method

The Scattering Pattern Matrix method was proposed by Matsushita at 2004 [68]. The method is an alternative method to the simple Fourier transform method. The method uses matrix solving techniques to solve the structure that generates the measured holograph. The benefit is that one can directly apply non-negative constraints in matrix solving so that the resulting electron density does not have negative regions. The non-negative constraint makes it possible to solve the real space image beyond the accuracy limit of the Fourier transform. Several groups have proposed similar matrix solving technique in XFH experiment [52, 69].

The hologram generated from XFH measurements can be expressed mathematically as a matrix transformation of real space electric density function $g(r,\theta',\varphi')$ into a reciprocal space holograph $\chi(\theta,\varphi)$.

$$\chi(\theta,\varphi) = T\cdot g(r,\theta',\varphi') \tag{1.21}$$

where $T = T(r,\theta',\varphi',\theta,\varphi)$ is the transformation matrix, which is known from the physics of XFH experiment:

$$T(r,\theta',\varphi',\theta,\varphi) = r_e\, Lorenz(\hat{r},\hat{k})\,\frac{\cos(\boldsymbol{k}\cdot\boldsymbol{r}-kr)}{r} \tag{1.22}$$

For a given hologram $\chi(\theta,\varphi)$ it is possible to find a solution real space electron density $g(r,\theta',\varphi')$ which satisfies Equation 1.21 by the Steepest Descent Algorithm [70]. This method is referred as the Scattering Pattern Matrix Method [68].

The Steepest Descent Algorithm is a method commonly used in least square fittings. It solves the matrix Equation 1.21 by first starting from a guess solution or zero. Then it finds a direction which could reduce the square of difference and goes from the last guess toward that direction. Iteration is performed to find the minimum the difference in the two sides of Equation 1.21.

The steepest descent algorithm offers theoretically better preference than the Fourier transform method since a non-negative constraint can be added to the solution of the electron density [70]. While Fourier transformation method results in electron density function with negative value in certain region, non-negative solution will be closer to real electron distribution inside the experimental sample [69].

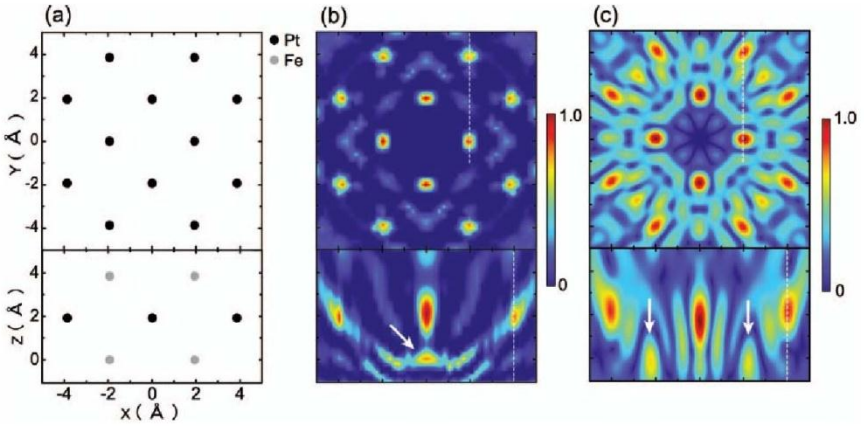

Figure 1.22 Structure of experimental FePt sample (left) , reconstruction by steepest descent algorithm (middle) and by reconstruction fourier transformation algorithm.

Source: [69]

Figure 1.22 is the result presented in report of Yukio et al. [69]. Contrast of the real space image is greatly improved with the steepest descent algorithm. Note the elimination of negative electron density also resulted in elimination of positive ripple peaks in real space image.

1.8 Application of XFH Method in Structural Studies

XFH methods are relatively immature in many aspects for applications. Data acquisition usually is performed only on the most powerful synchrotron radiation source, and yet takes hours or days for data collection. The structural information is easily available through other techniques. Nevertheless, many research groups have found the XFH method's unique usefulness in special circumstance.

Possibly, Marchesini et al. first successfully applied the method in local atomic structure study [65], which differs from the XRD method by the capability of the method to separate local structure around Mn atom from overall averaged crystal structure. Similar studies were later performed to study local structure around dopant atoms [55, 66, 71, 72].

Although most studies with XFH experiments were performed to improve the method itself, the advent of powerful synchrotron X-ray source and fast detectors with very high dynamic range have made the technique more accessible to experiments that come with more structural interests.

The ability of XFH method to distinguish trace or dopant elements from solid solution opened the possibility for monitoring local structure around a certain type of dopant, including distortions [55, 71] and formation of dopant clusters [72].

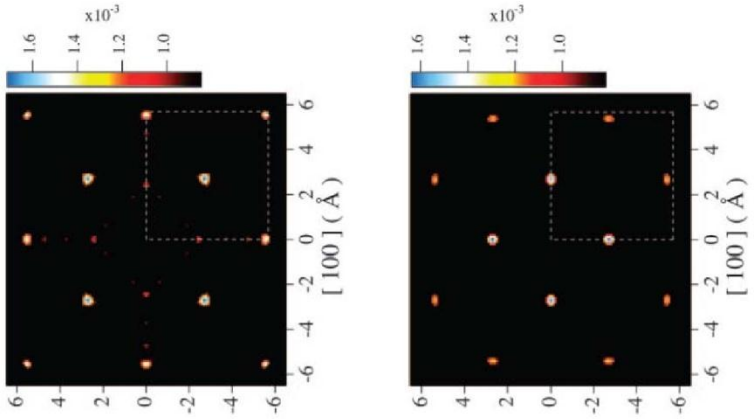

Figure 1.23 Local structure for germanium doped in silicon in the plane of dopant (left) and layer above germanium dopant (right).

Source: [55]

Figure 1.23 is an example of application of XFH method to study distortion of silicon structure around a germanium dopant. Distortion of the atomic position of silicon atom in dopant atomic plane and above the dopant shows a clear mismatch. The mismatch is explained as a result of dopant caused distortion.

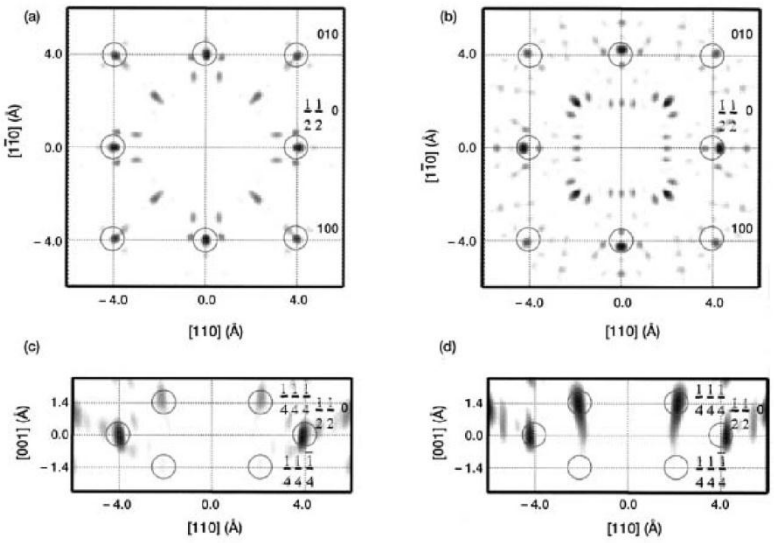

Figure 1.24 Local structure for germanium doped in silicon in $Si_{0.8}Ge_{0.2}$ (left) and structure in germanium crystal as contrast (right).

Source: [72]

Figure 1.24 is an example of direct measurement of germanium cluster formation in $Si_{0.8}Ge_{0.2}$ sample. The intensity of the nearby electron density from the germanium fluorescence center is compared with pure germanium sample. The intensity is found to be stronger than what the silicon atom could produce. The deviation is explained as the formation of Ge clusters. Table 1.2 is a summary of applications of XFH on practical problems.

Table 1.2 Some Applications using XFH Method

Author	Year	System Studied with XFH
Tegze et al.	2000	Oxygen in Nickel Oxide is observed [40]
Marchesini et al.	2000	Local atomic structure study of $Al_{70.4}Pd_{21}Mn_{8.6}$ [65]
Hayashi et al.	2001	Local structure around Zn dopant in GaAs crystal [66]
Hayashi et al.	2003	Cluster formation of Ge in $Si_{0.8}Ge_{0.2}$ [72]
Hayashi et al.	2005	Local structure around Cu in silicon steel [73]
Kusano et al.	2006	High resolution local structure around Ge in Si crystal [55]
Hosokawa et al.	2007	Tetrahedral symmetry around Ge in fcc $Ge_2S\ b_2Te_5$ [71]
Hosokawa et al.	2009	Local structure around Ga in $In_{0.995}Ga_{0.005}Sb$ [74]
Hu et al.	2009	Dopant cluster phase transition in $Ti_{0.50}Ni_{0.44}Fe_{0.06}$ [75]
Hosokawa et al.	2009	Structure around Zn in $Zn_{0.4}Mn_{0.6}Te$ mixed crystal [76]
Happo et al.	2009	Local structure around Mn in $Cd_{0.6}Mn_{0.4}Te$ [77]
Happo et al.	2010	Local structure around Zn in $Cd_{0.96}Zn_{0.04}Te$ [78]
Happo et al.	2011	Local structure around Mn in $Ge_{0.6}Mn_{0.4}Te$ [79]
Hayashi et al.	2011	Local structure around Mn in $ZnSnAs_2$:Mn [80]

XFH is now used as a tool to study crystal structures in very specialized problems in crystallography. Much application research was conducted with XFH since 2009. Hosokawa et al. [76] studied local structure around dopant Ga fluorescent atoms in $In_{0.995}Ga_{0.005}Sb$ and also studied the structure around Zn in $Zn_{0.4}Mn_{0.6}Te$ mixed crystal [74]. Hu et al. [75] observed a phase transition in clusters formed by Fe dopants in $Ti_{0.50}Ni_{0.44}Fe_{0.06}$.

Happo et al. used XFH to study fluorescent atom local structure in various samples including Mn in $Cd_{0.6}Mn_{0.4}Te$ [77], Zn in $Cd_{0.96}Zn_{0.04}Te$ [78] and Mn in $Ge_{0.6}Mn_{0.4}Te$ [79]. Hayashi et al. [80] studied the local structure around Mn dopant atoms in $ZnSnAs_2$ crystal. These studies are all similar in that they observe distortions and structure directly with the XFH method and measure bond-length and atom position shifts with the same method as shown in Figure 1.23.

CHAPTER 2

REVIEW ON SEMICONDUCTOR DETECTORS FOR X-RAY DETECTION

2.1 The Advent of Semiconductor Detectors

When X-rays were discovered in 1895, methods of detecting X-rays as well as other high energy particles were based on photographic plate or photo-fluorescent plates. Figure 2.1 is an example Wilhelm Roentgen's first "medical" X-ray image, taken with a photographic plate.

Figure 2.1 Wilhelm Roentgen's first "medical" X-ray, of his wife's hand, taken on 22 December 1895.

Source: [81]

Photographic material is still used today in medical diagnosis, while studies with ionization radiation switched to gas or liquid based detectors in the 1910s and 1920s. These detectors work by observing interaction of ionizing radiation with gas or liquid filled in a container. The gas filled radiation detector was invented by Hans Geiger while

working with Ernest Rutherford in 1908 [82]. Figure 2.2 is original design of Geiger's gas based counter in 1908 paper.

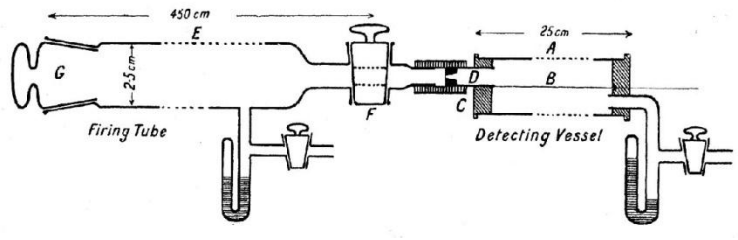

Figure 2.2 The original design of Geiger counter.
Source: [82]

A similar device was later redesigned by Geiger and Mueller in the 1920s and resulted in a portable and compact radiation detector known as the Geiger counter or a G-M counter. Figure 2.3 is a photograph of a commercial Geiger counter.

Figure 2.3 Photograph of a commercial Geiger counter.
Source: [83]

When ionizing radiation interacts with a working gas inside the Geiger counter, the gas is ionized and produces charged particles. A pair of charged electrodes around the working gas collects charged particle and generates a detectable electric current signal. The signal is then read out by a read out circuit. A Geiger counter uses gas as a

partial stopping medium and charged electrodes to collect ionization signal. The structure is essentially identical to the state of the art semiconductor detectors.

Silicon and other semiconductor detectors were first demonstrated to be able to work with low-amplitude signals and a noisy environment by the Joint Institute for Nuclear Research (JINR) in 1965 [84]. The advent of semiconductor detectors revolutionized the method of radiation detections soon after. Many different types of silicon and other semiconductor detectors have been devised and used. Research on semiconductor detectors has grown enormously. Development of semiconductor detectors is described in several review papers [85-88]. Due to the large volume of material on the topic, this review is limited to the introduction of a few types of silicon detectors.

2.2 Operation of Semiconductor Detector under Radiation

Similar to the Geiger counter, a semiconductor detector operates by detecting ionization charge between two biased electrodes. For a diode under reverse bias, the two electrodes are charged to form a high electric field across a high resistivity region. When ionization radiation produces an electron hole pair ionized in the high field region, the electron hole pair can be separated by the electric field, and thus be detected by a electric read out circuit before they recombine. Figure 2.4 is an illustration of photon generated electron hole pairs under an applied electric field in a diode detector.

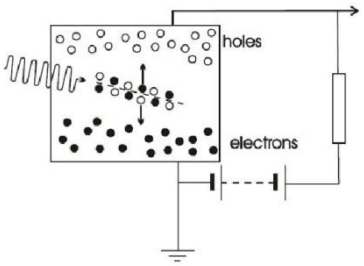

Figure 2.4 Principle of semiconductor detector under radiation.
Source: [89]

When an X-ray photon is absorbed in silicon, the energy deposited in silicon is hν where h is Plank constant, and ν is frequency of the photon. The number of electron hole pairs generated is, in most X-ray experiment except the limiting case of soft X-ray, proportional to energy of the incident photon and can be related by [90].

$$N_e = \frac{E_\gamma}{w} \tag{2.1}$$

Here N_e is number of generated electron-hole pairs, E_γ is the energy of the absorbed photon and w is pair creation energy required to generate electron-hole pairs by the photon. w was considered a constant and verified to be independent of radiation energy for a long period of detector operation [86, 91-93]. The average energy used for the creation of electron-hole pair in silicon is W_{Si} = 3.6 eV and in germanium is W_{Ge} = 2.9 eV [94].

When a semiconductor detector is used for detecting charged particles, the Bethe-Bloch equation holds and gives the rate of ionization loss of a charged particle in matter [95]:

$$\frac{dE}{dx} \propto \rho \frac{Z}{A} \frac{z^2}{\beta^2} \left[\ln \left(\frac{2m_e \gamma^2 v^2 W_{max}}{I^2} \right) - 2\beta^2 \right] \tag{2.2}$$

Where ρ is the density of the medium; Z is atomic number of the medium; A is the atomic weight of the medium; z is the charge of the particle with velocity v; $\beta = v/c$, $\gamma = 1/(1 - \beta^2)^{1/2}$; W_{max} is the maximum energy transfer in a single collision; I is the effective ionization potential averaged over all electrons.

The amount of energy that is deposited in silicon detector can be calculated with the Bethe-Bloch formula in Equation 2.2. The deposited energy is proportional to the number of created electron-hole pairs [94].

Although ionization radiation can be captured in any part of the semiconductor, only electron hole pair generated inside an electric field will travel in opposite direction and form the signal to be detected by read out circuit. So the design of a semiconductor detector has to provide a large volume of sensitive regions, which is accessible to radiation. The following properties of materials have to be considered [96] in semiconductor detectors:

1. High resistivity, which allow for high electric fields that give complete charge collection in a short interval of time.
2. High carrier mobility, needed for rapid charge collection.
3. Low trapping rate, to avoid recombination, leakage current etc.
4. Low energy gap, which give more electron-hole pairs for same deposited energy.
5. High stability chemically and structurally, for prolonged operation under radiation exposure.

Silicon with high resistivity can be achieved with high purity silicon, or silicon doped with compensated donors to form near intrinsic carrier concentration, or use depletion region in a diode.

Another important parameter in semiconductor design consideration is noise level. There are three major noise sources from semiconductor materials [96]:

1. Thermal noise, also mentioned as 'Johnson noise', is the thermal fluctuation of electrons inside detectors. The equivalent current of this noise is given by [96]:

$$\overline{i^2} = 4kT \cdot G \cdot \Delta f \tag{2.3}$$

Where G is conductivity of the detector and Δf is the bandwidth.

2. Current noise, also called 'shot noise', is the statistical fluctuations in the number of moving charge carriers that form an electric current. The equivalent current of this noise is given by [96]:

$$\overline{i^2} = 2eI \cdot \Delta f \tag{2.4}$$

3. Flicker noise is not yet well understood. The equivalent current of this noise is given by [96]:

$$\overline{i^2} \propto 1/f \cdot \Delta f \tag{2.5}$$

Flicker noise's power spectrum mostly resides at low frequency, thus for the design of fast semiconductor detector, Flicker noise is not an important noise for consideration. A low noise detector is achieved in low conductivity material, with minimum leakage current and suitable bandwidth. State of the art silicon detectors have resistance reaching or over 10 GΩ in the best specimens [88]. Thus thermal noise and leak current are negligible. The dominant noise source comes from current and resistance in the preamplifier input circuit [88].

2.3 Surface Barrier Detectors and P-n Junction Detectors

2.3.1 Structure

Surface barrier detectors and p-n junction detectors have a depletion region as their active region. Depletion regions can be formed with many technologies. These techniques for building of a surface barrier detector and p-n junction detector have been intensively studied since the advent of semiconductor detectors in 1950s and 1960s [97-101].

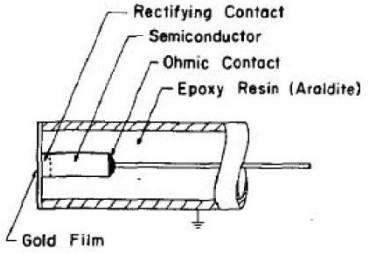

FIG. 3. Cross section of a surface barrier diode (schematic).

Figure 2.5 Structure of surface barrier detector in 1950's.

Source: [97]

Figure 2.5 is a schematic of a surface barrier detector as presented in Mayor's 1959 paper [97]. Surface barrier detectors use a low doped high resistivity wafer.

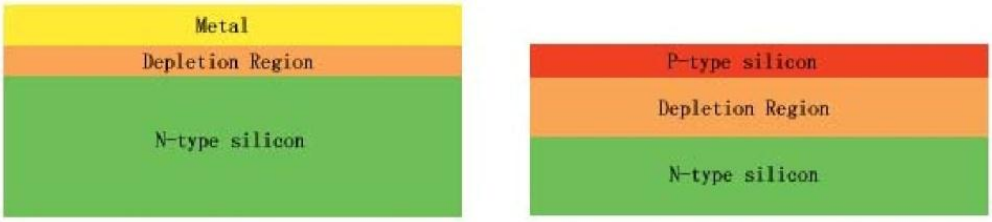

Figure 2.6 Doping profile of Schottky diode (left) and p-n junction diode (right).

Figure 2.6 is a doping profile of a Schottky diode and a p-n junction diode. Depletion region is formed at interface between metal and low doped silicon in a Schottky diode, and at interface of p-n junction in p-n junction diode. The process of

depletion region formation is described by drift-diffusion model. When charge carriers in semiconductor drift through a semiconductor-metal interface, or a p-type-n-type interface, no charge carrier is left inside the diffusion region of the semiconductor, thus a depletion region forms. Although detectors based on p-type substrate can also be made with success [102], most semiconductor detectors are produced with n-type silicon substrates [88].

2.3.2 Principles

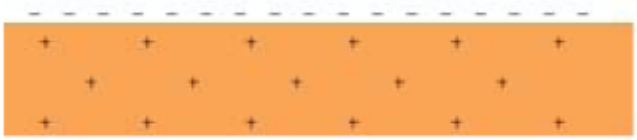

Figure 2.7 Charge distributions in depletion region.

When a Schottky diode detector or p-n junction diode detector are under reverse bias, an electric field is established across the depletion region, as is shown in Figure 2.7. Charge concentration in the depletion region is identical to the dopant concentration $q = e N_D$ and is uniformly distributed. Thus electric filed can be written as:

$$\varepsilon(y) = \frac{e}{\epsilon\epsilon_0} N_D \frac{y}{d} \tag{2.5}$$

Where N_D is dopant concentration, y is position in depletion region, d is depletion region thickness. Potential difference across the depletion region is:

$$V_D = \frac{1}{\epsilon\epsilon_0} \frac{eN_D d}{2} \tag{2.6}$$

Thus, one has the active region thickness, i.e. depletion region thickness:

$$d = \frac{2\epsilon\epsilon_0}{e}\frac{V_D}{N_D} \tag{2.7}$$

Active region thickness is an important parameter that determines the detector's over all capacitance C and resistance R. Results in later sections show that the detector's capacitance is a major factor to determine system signal to noise ratio. It also determines energy deposition efficiency for high energy particles. Larger active region thickness sustains higher bias and is achieved by lower doping level.

2.3.3 Technology

Techniques for building a Schottky diode or a p-n junction diode are simple, since they have simple structure and doping profiles. Schottky diode detector starts from low level doped silicon. A rectifying Schottky junction is formed by evaporating a thin layer of metal on the surface of silicon. P-n junction detectors are typically formed by phosphorus diffusion or implantation.

2.3.4 Performance

Industrial silicon based surface barrier detectors are also called Silicon Surface Barrier (SSB) detectors. P-n junction detectors made of diffusion technology are called Diffusing Junction (DJ) detectors. Both techniques were heavily employed and studied in the 1960's and 1970's [96]. For application of X-ray detection in synchrotron radiation researches, these detectors are now mainly replaced by planar technology [88]. SSB detectors has gained applications in heavy ion detection [103, 104]. An example detector of this type is reported by Cywiak et al.. These detectors are fabricated on 0.27 ~ 0.28 mm thick N-type ultra-pure silicon with a diameter of 5 mm. The detector is operated to detect particles at 4.2 MeV with resolution a of 35 keV [105].

For that SSB and DJ detectors are made form a whole silicon wafer, their active region and junction area are exposed at the surface. Careful surface treatment has to be performed to reduce influence from surface states [105].

2.4 Detectors Based On Planar Technology

Today's most semiconductor detectors are produced with p-n junction structure with planar technology [94].

2.4.1 Structure and Technology

Figure 2.8 is an illustration of the process to produce a p-n junction detector.

Modern planar technology uses n-type silicon with impurity amounts down to 10^{12} cm^{-3} [88]. The purity is high enough to form a thick near intrinsic silicon region in the detector. Planar technology adapted to modern integrated circuit manufacture facility. In the planar technology, boron is doped from one side of ultra-pure silicon to form p-type region. Arsenic is doped from the other side to form n-type region. A PIN junction is formed directly and has p-type and n-type regions on each side, and a near intrinsic silicon region in between. Planar technology is capable of producing multiple detectors on a single substrate.

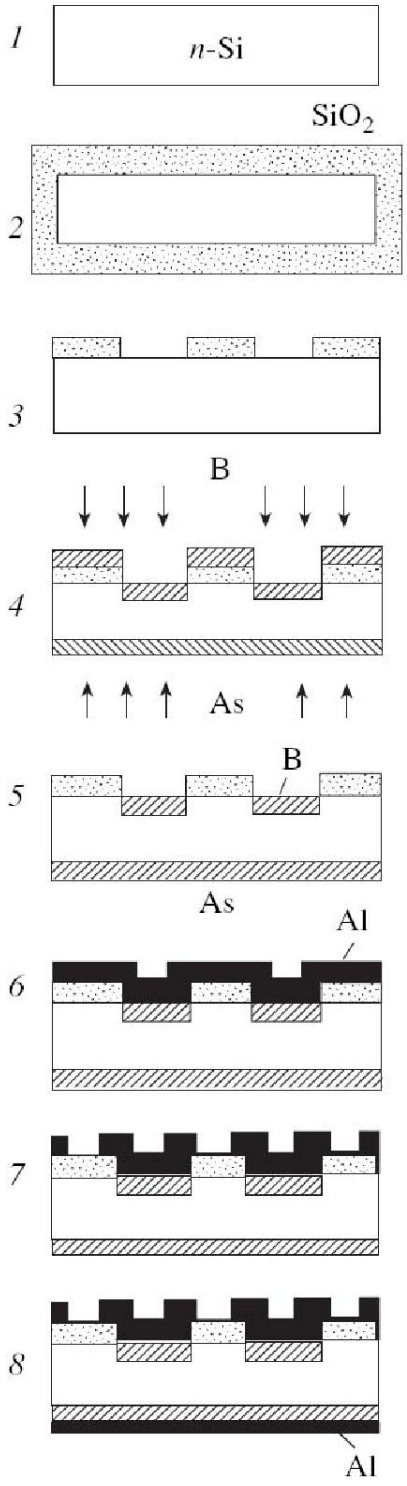

Figure 2.8 Planar technology for making p-n junction detector.

Source: [88]

2.4.2 Performance

Figure 2.9 Planar technology silicon detector of Canberra Industries, Inc.
Source: [106]

Figure 2.9 is a silicon detector manufactured with planar technology. The X-series detector from Canberra Industries, Inc. has 5 mm^2 active areas and 0.5 mm thickness. It has resolution better than 190 eV in its working energy range from 1 to 30 keV [106].

2.5 Electronics for Read-Out Function

The read out circuit is a charge sensitive amplifier. A detector is capacitive and its charge is generated from ionization radiation which is proportional to energy of the ionization particle.

$$E \propto Q_s = \int i_s(t)dt \tag{2.8}$$

Figure 2.10 is the model of the charge sensitive front amplifier connected to detector, which is capacitive in nature.

The input capacitance of the frontend amplifier is connected in parallel with the detector, thus the voltage on the input side V_i of the amplifier is determined by ionization charge and total capacitance.

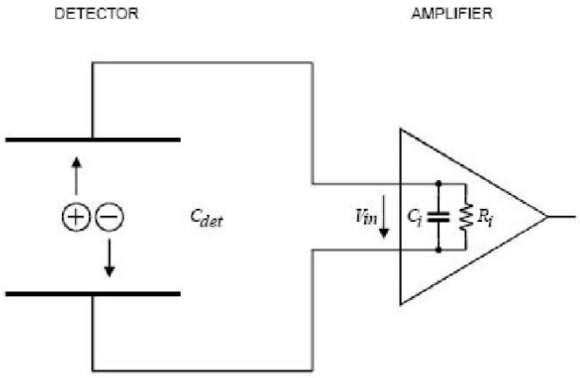

Figure 2.10 Detector and amplifier.

Source: [107]

$$V_i = \frac{Q_s}{C_d + C_i} \tag{2.9}$$

Where C_d is capacitance of the detector and C_i is the capacitance of the frontend amplifier. Assuming that noise generated from the detector and amplifier is a constant only depending on temperature. The signal to noise ratio is then given by:

$$S/N = \frac{V_i}{V_N} \propto \frac{1}{C_d + C_i} \tag{2.10}$$

Noise can be suppressed by reducing input capacitor as shown in the above equation. However, the overall noise potential after the frontend amplifier is still large compared to the signal. To further improve signal to noise ratio, band filters are applied after the frontend amplifier. The idea is that noise has a wide spectrum, while the signal

from the detector can be processed with a reduced sensitivity spectrum. By reducing the sensitive band, noise at outside of the band pass filter can be removed and give an improved signal to noise ratio.

Figure 2.11 is a illustration of the band pass filter, usually called a shaper in detector read out circuit. The RC differentiator and RC integrator form a high pass and low pass filters respectively and together form a band pass filter. A real shaper in detector read out circuits may contain multi-stage filters and may use different filter design strategies, like gyrators, to form more ideal filter property. The result of the shaper is reduced noise at the cost of maximum speed of detector operation. For a detector designed with a fast count rate, it is necessarily to have an amplifier channel with sufficient band pass, which inevitably result in higher noise.

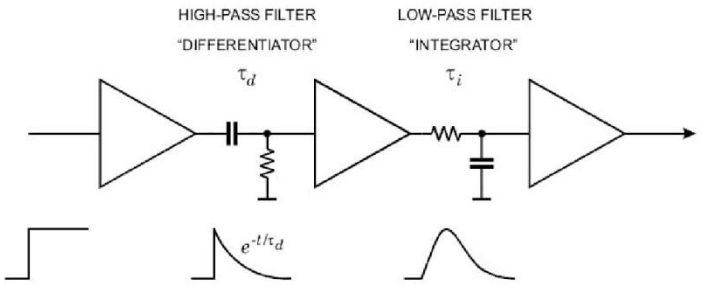

Figure 2.11 A shaper with high-pass filter and low-pass filter.
Source: [107]

The output signal of the shaper is a well-defined pulse whose height represents the energy deposited in the detector. This signal is usually used as an output of the frontend read out circuit and is guided to a MCA or other type of counter. This signal can also be further processed on a read out circuit chip with either digital circuit or analog circuit. The BNL HERMES based ASIC readout circuit uses an on-chip 14 bit analog to

digital convertor (ADC) to process and store the output signal. The fast ADC is achieved by flash ADCs which have 2^{14} comparators connected to analog input and directly produce digital correspondence to the analog signals. The digital data can be later read out from the digitized circuit. The BNL Maia based ASIC uses VLSI Analog circuit with Switch-current technology or Switch-capacitor technology to process the output analog signal and store the signal. The stored analog signal can be read out later with a timed analog circuit.

Figure 2.12 is a very simple illustration of analog memory cell realized in the switch current technique. The current through the MOSFET is only dependent on the gate charge, when the gate is put into high resistivity state as to other circuit, current through MOSFET is recorded.

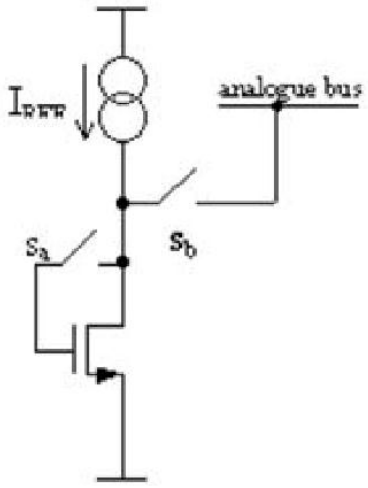

Figure 2.12 A very simple illustration of analog memory cell realized in switch current technique.

Source: [108]

For a more detailed reference of the switch current technique, as well as analog VLSI mixed signal processing technique, refer to Reference [108].

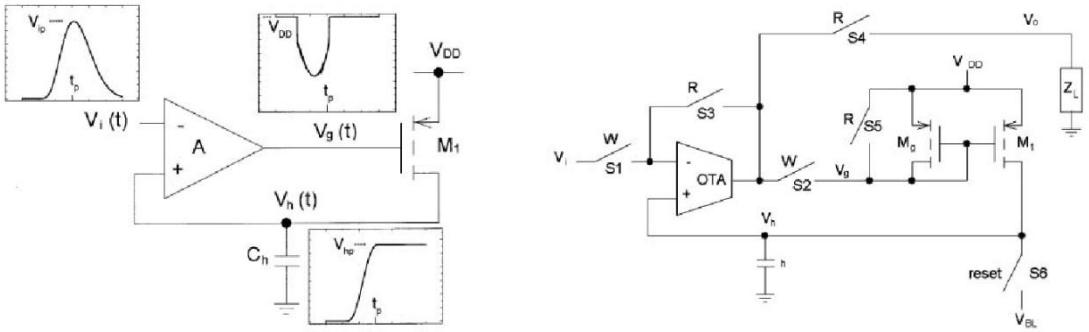

Figure 2.13 Operational principle of a peak detector (left) [109] and a practical two phase peak detector with switch current technology (right) [110].

Source: [109, 110]

Figure 2.13 is electric schematic of the peak detector used in fast signal processor for the detectors. The peak detector captures and holds the maxim pulse height of the incoming pulse to provide sufficient time for digitization. A practical two phase peak detector separates current in write phase and read phase [110].

2.6 Lithium Drifted Silicon Detectors

A special type of p-n junction diode is the lithium-drifted silicon detector.

2.6.1 Structure and Technology

Figure 2.14 is a simplified process for making lithium-drifted silicon detectors. A lithium-drifted silicon detector has the same structure as diffusion junction detector but use lithium as a p type dopant in silicon with n type impurity. The detector starts with high purity n-type silicon. Lithium is coated on one side and diffuses into the silicon wafer at elevated temperature and applied voltage. Figure 2.15 is an illustration of lithium doping profile in diffusion profile and drift process. The doping profile of lithium in the drift process is controlled by electric fields, thus drifted lithium will

compensate the doping profile of the n type silicon and form uniform and near intrinsic region in the drift region. Thus a thick PIN junction structure can be achieved with the technology.

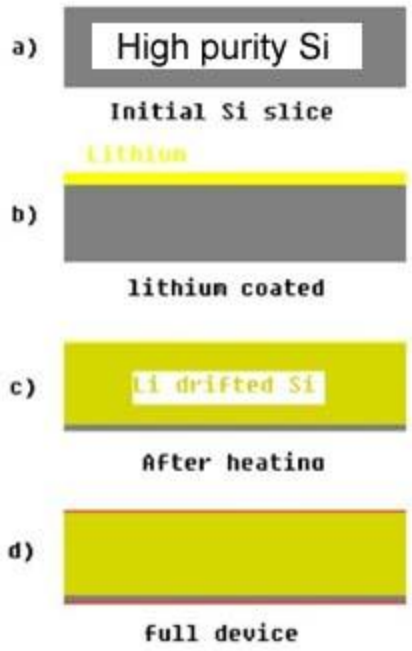

Figure 2.14 Process to build lithium-drifted silicon detector.

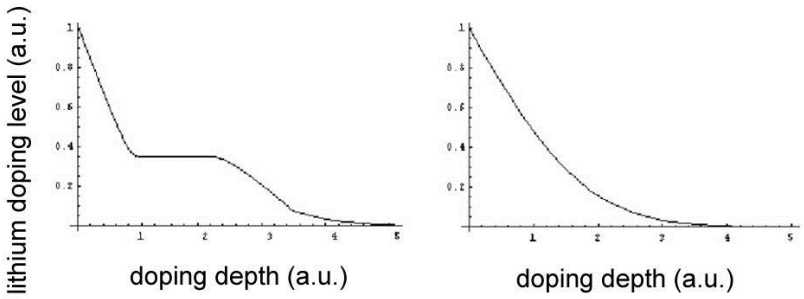

Figure 2.15 Sketch of lithium doping profile in diffusion (right) and drift (left) process.

2.6.2 Performance

Lithium drift detectors are widely employed in X-ray spectroscopy application for it good energy resolution. Figure 2.16 is an example CANBERRA Si(Li) detector system, cooled with liquid nitrogen used as a coolant.

Figure 2.16 CANBERRA Si(Li) detector.
Source: [106]

The CANBERRA Si(Li) detector can achieve 120 eV energy resolution at Mn Kα line (6.5 keV) at low count rates.

2.7 Avalanche Photodiodes

2.7.1 Structure and Technology

An avalanche photodiode (APD) is a reversely biased diode with electric field in its depletion layer strong enough to cause multiplication of signal charges. Figure 2.17 illustrate the typical structure of an APD.

Typical APDs consist of a thin highly doped n-type layer on top of a moderately doped p layer. The extra p layer as compared to normal PIN structure is for electric field control. When this structure is reversely biased, a strong electric field present on the n+ top layer junction, together with the lower field across the intrinsic region. The strong electric field gives an amplification of the signal charge as multiplication occur in this region.

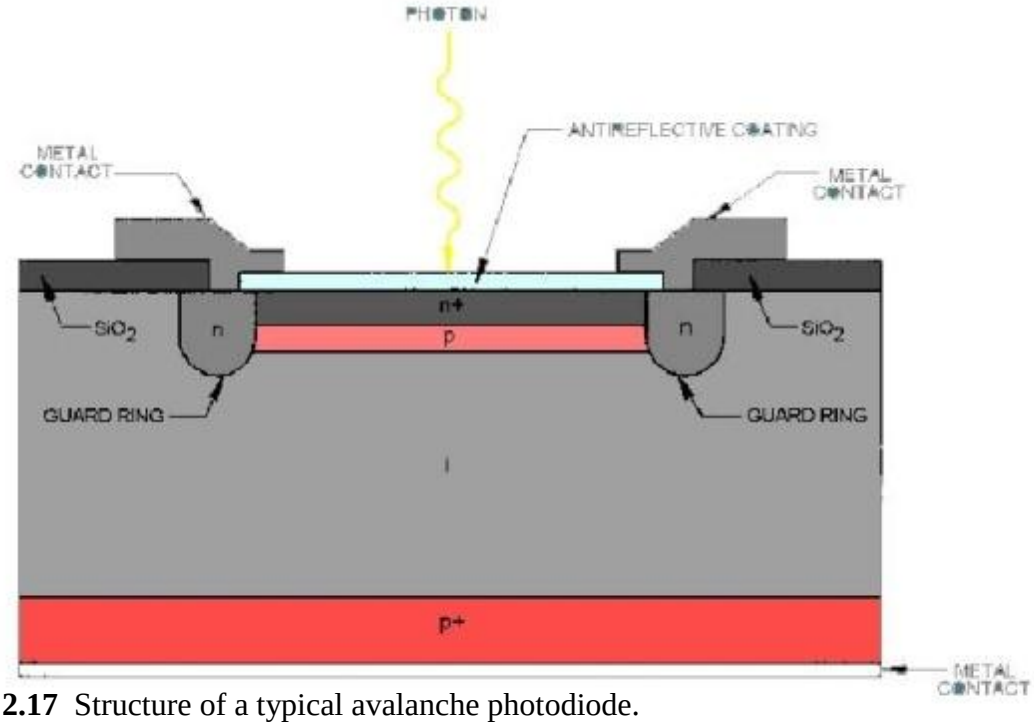

Figure 2.17 Structure of a typical avalanche photodiode.

Source: [111]

2.7.2 Performance

Different operational modes are available for APDs. At low voltages, APD can be used as ordinary PIN diode detectors with no intrinsic amplification of charge signals. For higher supplied voltage, electrons become sufficiently accelerated to produce multiplication pairs. The amplified signal is proportional to the ionization signal, with some noise is added by the multiplication process. APDs operated in this mode have

linear response to photo energy and thus can be used as energy resolving detectors. The extra noise is called excess noise and is purely caused by statistical randomness. At even higher applied voltage, holes and secondary electron-hole pairs begin to produce multiplication. A highly nonlinear response could appear in this condition. APDs could be used for single photon detection at this mode.

Although APDs are demonstrated capable to directly detect X-rays from 1 to 30 keV energy range with energy resolution [112], general APDs only operate on visible light and infrared with acceptable noise [112]. APD have gain popularity in laser rangefinders and long range fiber optic telecommunication. Because of APD's internal amplification alleviates the requirement of amplifier circuits, APD can provide high speed and high sensitivity unmatched by PIN detectors [112], visible light and infrared radiation. PerkinElmer Inc. demonstrated APD with > 70% photon detection efficiency at 633nm photon wavelength with pulse width of only 20 ns. When an APD is used to detect X-rays without energy resolution, or coupled to scintillator crystals to detect X-ray, the narrow pulse width of only 20 ns give APD power to detector photon at 50 MHz speed, while amplifier circuit for PIN detectors usually operate a 1 MHz.

2.8 The Charge Coupled Devices

2.8.1 Structure and Operational Principle

Charge-coupled devices (CCDs) were first proposed by Boyle et al. as detectors of optical images in 1970 [113]. When used in the detection of X-ray, CCDs performed as well as in digital camera.

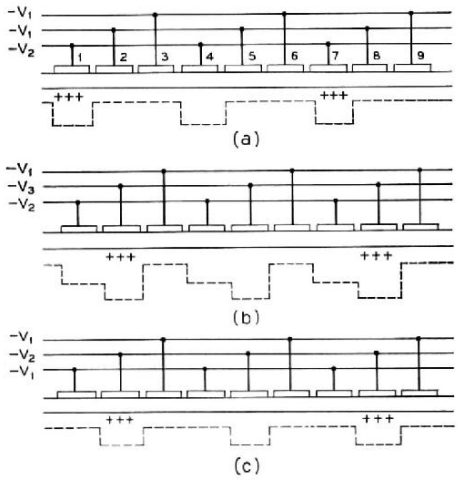

Figure 2.18 Operational principle of charge-couple devices (CCDs) as proposed in Boyle's 1970 paper.

Source: [113]

Figure 2.18 is the illustration of the CCDs' working principle as stated in Boyle's 1970 original report [113]. The CCDs store a charge signal in its capacitive detector arrays, the charge signal can be transferred from one pixel to another by controlling potential difference between neighboring pixels. All pixels are partitioned into three groups and the voltage applied on the three groups change alternatively. Thus the whole array of charge signal can be read out one by one as the charge is migrated to one side of the read out circuit.

In order to avoid noise current between neighboring pixels while migrating, modern CCD devices have pixels partitioned into more than three groups and charges move with more complex patterns, the principle is however identical to the original report.

2.8.2 Performance

CCD devices do not have energy resolution and are designed to work with visible light. When CCDs are used to detect X-ray, a scintillator crystal is required to convert X-ray photons into visible light.

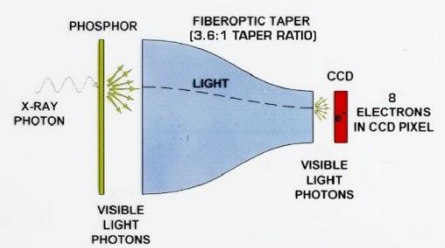

Figure 2.19 CCD with scintillator crystals and fiber optic demagnifier.
Source: [114]

Figure 2.19 is an illustration of a CCD working with a scintillator crystals and fiber optic demagnifier. CCD systems are implemented in X-ray detection for its very high spatial resolution. State of the art CCD detector has active areas up to $0.4m^2$. An Example Q315 model CCD detector produced by Area Detector Systems Corporation has with active area of 315 mm diameter and 200,000 pixels [114].

2.9 Drift Detectors

2.9.1 Structure and Operational Principle

The operating principle of drift detectors was proposed by Gatti and Rehak in 1984 [115].

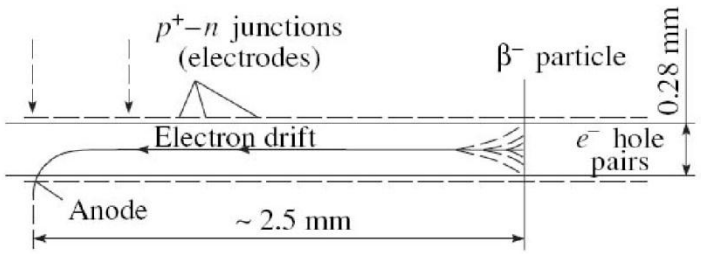

Figure 2.20 Working principle of drift detector.

Source: [88]

Figure 2.20 is an illustration of working principle of drift detector as proposed by Gatti and Rehak in 1984 paper. A Silicon Drift Detector (SDD) is built on a ultra-pure silicon wafer with planar technology. A small anode is formed on one side in the center of the detector. A concentric ring shaped cathode is formed on both sides. The potential of the whole detector is carefully controlled by strip electrodes on both side of the detector to from a depletion region extend from the small anode to entire detector. When ionization radiation creates electron hole pairs in the depletion region, holes are collected at the nearby cathode, and electrons will drift in the depletion region of the detector to anode.

By this special configuration, anodes can be small while maintaining a large volume of depletion region. Unlike PIN detectors, the anode area is not proportional to depletion area. Therefore SDD detector can achieve much smaller detector capacitance than PIN detectors, and thus provide better resolution, detector speed and lower noise.

Modern SDD detectors integrate first stage readout MOS amplifier inside the detector to further reduce input capacitance of the readout circuit. The center part in Figure 2.21 is the MOS transistor that is integrated into the sensor.

Drift detector provide high spatial resolution; the position of ionization can be determined by the drift time and can provide sub-millimeter spatial resolution [88].

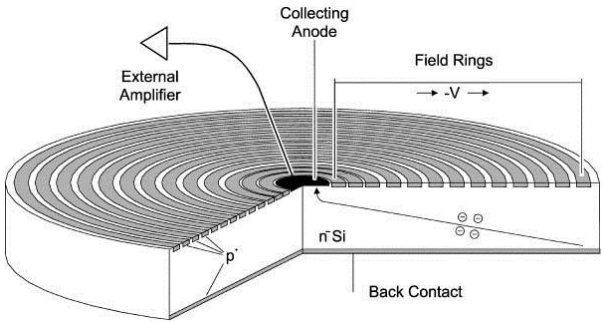

Figure 2.21 A ring drift detector.

Source: [116]

Figure 2.21 is an example of a ring shaped drift detector [117]. Detectors of this type offer integrated amplification for the anode and nearby electrode from a FET in the detector.

2.9.2 Performance

As an example state of the art SDD detector, Oxford Instrumentation offers the X-Max SDD detector system with up to 80 mm^2 active area. The SDD detector works with a count rate of 500 kcps with resolution better than 124 eV for Mn K X-ray (6.5 keV) [118]. Figure 2.22 is a photograph of the Oxford Instrumentation X-Max SDD detector system.

Figure 2.22 Oxford instrumentation X-Max silicon drift detector system.

Source: [118]

2.10 Strip Detector and Pixel Detector

With the application of planar technology, large detectors can be divided into strips or even pixels [119]. Strip detectors and pixel detectors are arrays of PIN detectors, each with its own read out circuit. An array of detectors can provide spatial resolution, together with parallel processing capability. These detectors can be as small as a single detector as shown in Figure 2.24, it can also be a huge detectors used in high energy particle experiment. In early 1980's, large size multi-layered onion-type silicon detectors were produced for experiments on high energy particle accelerators, especially colliders [88]. These large detectors are designed to provide spatial resolutions. Signal from the strips are read out by circuits placed on one or both side of the strip detector.

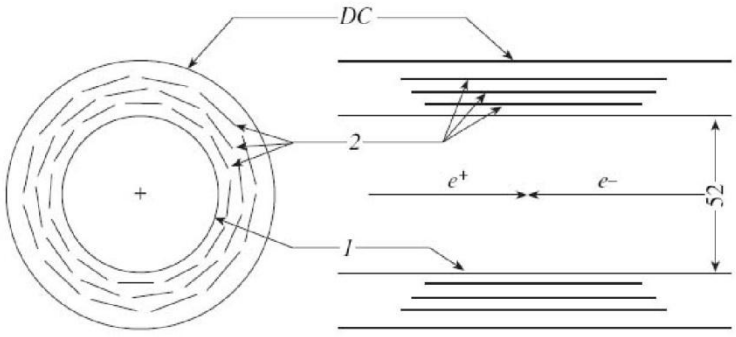

Figure 2.23 An example onion-type strip detector designed for collider applications.

Source: [88]

Figure 2.23 is an example of the 1980's onion like large scale silicon detector.

Figure 2.24 is a pixel detector connected with side read out circuit produced in Brookhaven National Laboratory (BNL). The large detector is divided into 32 pixels and connects to independent read out circuits. Detectors of this structure provide parallel processing power of 32 channels.

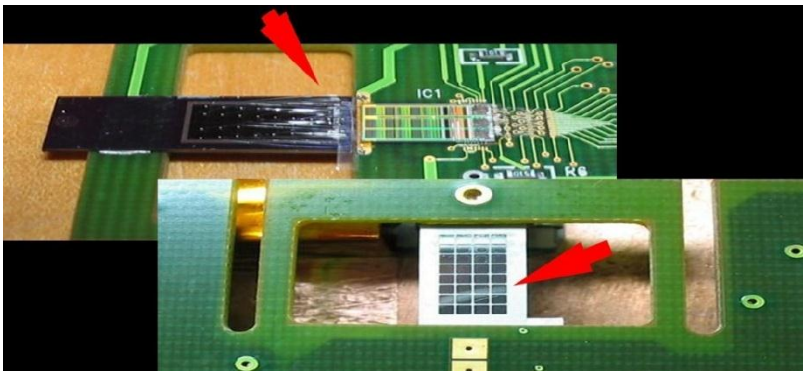

Figure 2.24 A pixel strip detector with side read out circuit.

Table 2.1 gives some example large strip detector projects for high energy particle experiments.

Table 2.1 Example Large Strip Detector Projects for High Energy Particle Experiments

Detector	Silicon area [m^2]	No. of strip readout channels (10^6)
CMS	210	9.6
ATLAS	61	6.3
CDF II	5.8-8.7	0.722-1.083
D0 2	4.7-8.3	0.793-0.952
ZEUS		0.207
LHCb VELO	0.32	0.205
AMS 2	6.5	0.196
Delphi	1.8	0.175
Babar	0.95	0.14
Phobos		0.137
Aleph	0.49	0.095
L3	0.23	0.086
Belle SVD		0.082

Source: [120]

2.11 The HERMES Based 384 Element Detector

Three types of detectors are being developed and utilized: a HERMES 384 element detector, a 96 element Maia detector and a 64 elements silicon drift detector for use in high count rate high energy resolution applications of X-ray holography. HERMES is the name of ASICs used in the NSLS energy resolving detector with multiple elements. The HERMES 384 element detector is composed of 384 independent detector elements and read out circuits. The HERMES readout ASIC contain frontend amplifier, shaper, fast ADC and digital processing components in each channel. The detector is cooled with a Peltier unit and provides ~200 eV energy resolution at low count rates. When energy resolution is not critical, each element can be operated at 1,000,000 cps count rate and together 384 channels can provide a very high dynamic range. In this mode the energy resolution approaches 400 eV. Figure 2.25 is a photograph of the HERMES 384 element detector.

Figure 2.25 A photograph of the HERMES 384 element detector.

Figure 2.26 compares spectra measured from each element in the detector before and after compensating photon energies with trim parameters in the detector. Since the 384 channels are independent to each other, trimming is necessary for aligning spectra in the 384 channels.

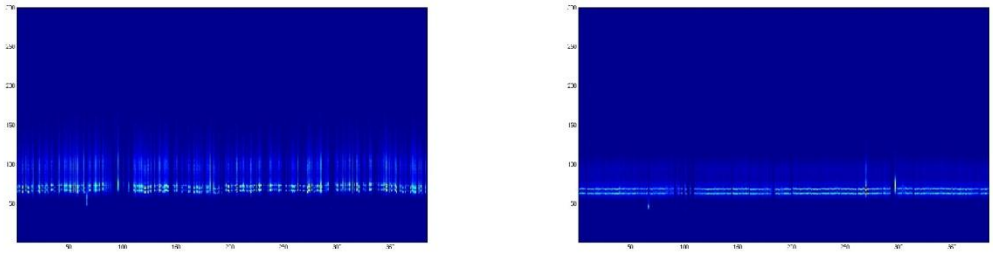

Figure 2.26 Spectra of Germanium K_α and K_β peaks plotted as a function of element number in detector measured before the peak energy is compensated with trim parameter (left) and measured after the peak energy is compensated with trim parameter (right).

When properly trimmed, the whole 384 channel can be used as a very fast detector with energy resolution. This allows XFH experiments to be performed without an analyzer crystal, and thus reduce the requirement of high beam intensity. This enables the possibility that XFH scans can be performed within hours rather than days with the detector.

2.12 The Maia Based Detector

Maia is a second generation multi-channel detector technology developed in NSLS. It has read out circuits made up from the HERMES ASIC and SCEPTER ASIC combination. Here HERMES ANSI is only used as preamp/shaper. SCEPTER is a analog processing ASIC designed for Peak Detector/Derandomizer (PDD).

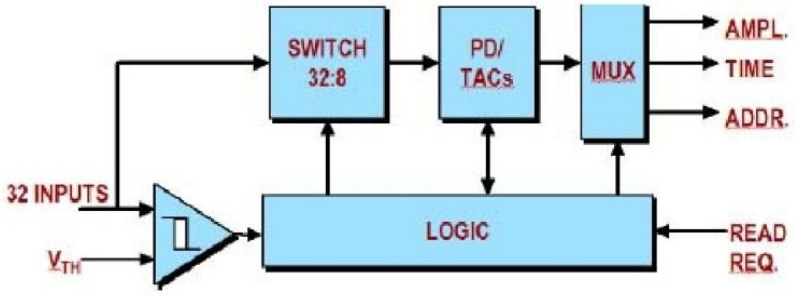

Figure 2.27 A block diagram for PDD ASIC.

Source: [121]

Figure 2.27 is a block diagram for the PDD ASIC [121]. The circuit contains a set of eight peak detectors and associated time-to-amplitude converters (PD/TACs) which are shared and routed to 32 input channels. A 32 to 8 routing logic array derandomize the incoming signal and finds an available PD/TACs for an incoming pulse. The multiple PD/TACs, together with the derandomizer, effective sparsify and buffer the data resulting in exceptionally low dead time.

The processing results is buffered in PD/TACs and read later, governed by the control logic. The upgrade to the Maia detector provides a method for distinguishing pileup events, by checking the ratio between peak amplitude and time over threshold, and thus provides better read out preference than HERMES.

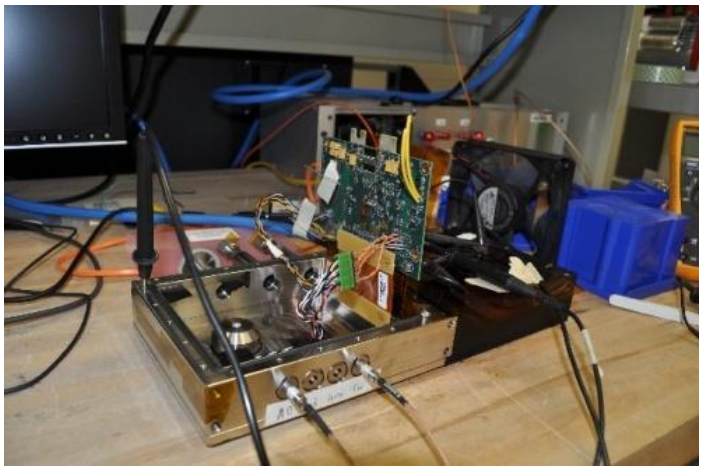

Figure 2.28 A photograph of the Maia detector under development.

Figure 2.28 is a photograph of the Maia detector under development. The detector has now undergone several tests but is not yet ready for XFH experiments. When the detector is ready, it is expected to have better stability and thus less noise in XFH experiment. New generations of detectors (384 element, Maia and drift detectors) are being developed under a collaboration involving NJIT and BNL.

CHAPTER 3

DEVELOPING AN EXPERIMENTAL SETUP FOR X-RAY FLUORESCENCE HOLOGRAPHY (XFH) MEASUREMENTS AT NSLS BEAMLINE X14A

3.1 Introduction

The development of Multi-element detectors with high energy resolution has made fast and low noise XFH measurement possible. A large amount of effort has been spent to setup and configure beamline X-14A so that low noise combined with fast scan speed for XFH is achieved. In this chapter, a detailed description of the setup of this National Synchrotron Light Source (NSLS) beamline at Brookhaven National Laboratory (BNL) is given.

3.2 Goniometer in Beamline X14A at NSLS

The NSLS X14A beamline uses a large bent crystal monochromator to intercept 10 mrad of X-ray beam and focuses it to a 1x3 mm^2 beam spot. The beamline provides photon flux of 10^{12} cps at its best condition. Sample and detector are mounted on a goniometer. Accurate alignment and scanning can be performed with the goniometer.

Figure 3.1 is a photograph of the goniometer at the NSLS beamline X14A. An avalanche photodiode (APD) detector and a crystal analyzer are attached to the goniometer. The X-ray beam from synchrotron is guided from behind the goniometer on the far left of the picture to the center of goniometer.

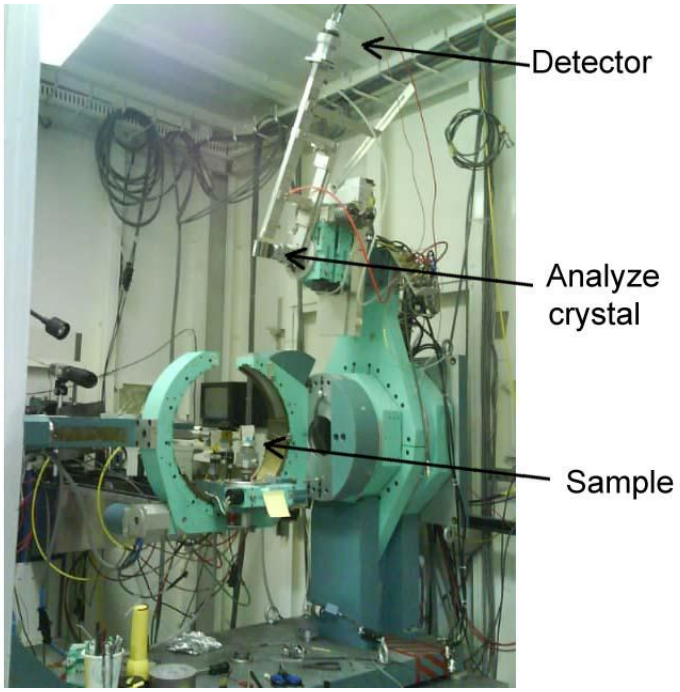

Figure 3.1 Photograph of goniometer in beamline X14A.

3.3 Modification of the Beamline Control System for the Piezoelectric Actuator for Improved Beamline Stabilization

It was noticed that the beamline system was not stable enough to keep the optics fully tuned during a full scan of X-ray holography. Drifting of the incoming beam position at the monochromator is observed during measurements. For a XFH measurement that takes hours to complete, focusing and tuning the optics during experiments is required to compensate for instability and drift of the beam position. Manual adjustment that tunes the monochromator is time consuming and impractical if a XFH measurement is continuously performed for many days. An automatic beamline tuning and control algorithm was devised to help perform XFH experiments under the best optical conditions.

Figure 3.2 Controller for piezoelectric actuator on monochromator at beamline X14A.

A piezoelectric actuator is attached to the first monocrhomator crystal in the X14A beamline. This actuator can tilt the crystal slightly if the incoming beam position has drifted. Beamline optics tune-up can be realized by manually adjusting the tilt of the first monocrhomator crystal. Figure 3.2 shows the controller of the piezoelectric actuator. The controller can be remotely controlled by the beamline computer.

A program that automatically tunes the beamline optics was developed. The script monitors the beam intensity and automatically compensates to fix the small drift in incoming beam position, using the piezoelectric actuator. This program reduces the beamline instability due to the position of incoming beam.

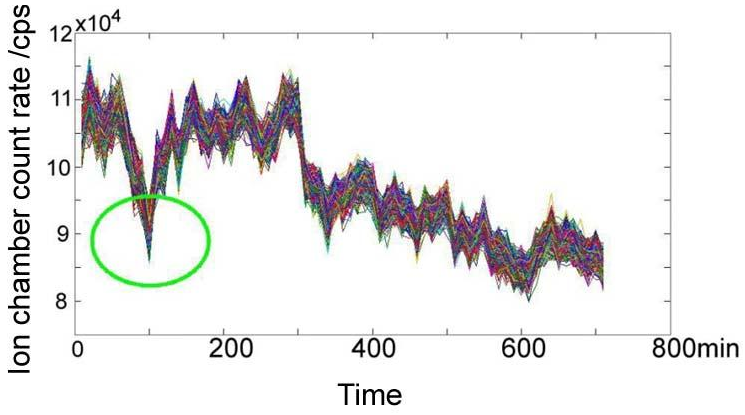

Figure 3.3 A plot of beam intensity during a holograph scan showing recovery of the loss of intensity by the feedback system. The x-axis time is in minutes. The y axis is the intensity in arbitrary units.

Figure 3.3 is a plot of beamline intensity during a holograph scan and the highlighted point is where the program has altered the piezoelectric actuator and compensation has taken effect. The piezoelectric actuator is configured as a pseudo-motor [122] in the X-14A beamline's software interface [122]. The detailed program for automatically tuning the beamline optics is described in Appendix A.

3.4 Fast Scanner Controlled by DC-motor and Position Encoder

Fast and high resolution XFH scans requires a fast scanner with smooth rotation speed. A DC motor is ideal to provide fast and smooth rotation speed and its position can be read out by an encoder. Figure 3.4 is a fast scanner with encoder developed for XFH experiments at beamline X14A. The scanner is capable of providing 0.2 ~ 1.0 rev/s rotation speeds.

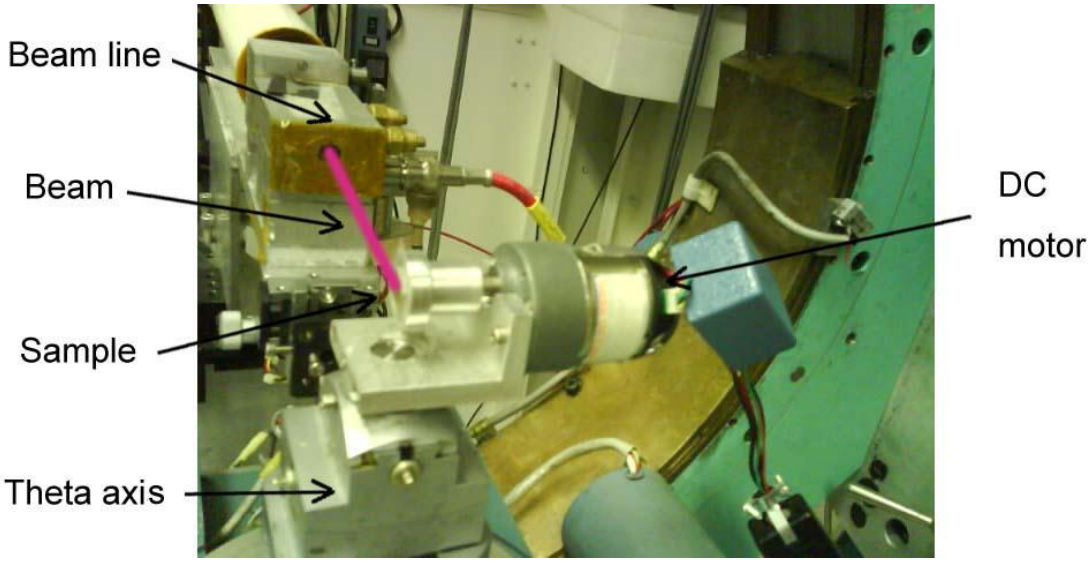

Figure 3.4 A photograph of the fast scanner.

The fast scanner system was designed and assembled at NSLS. A geared DC motor is attached to a E4P OEM optical kit encoder [123] (Figure 3.5). The encoder provides an encoded pulse that represents the angular position of the motor.

Figure 3.5 The E4P OEM encoder that provides an indication of the location of the DC motor.

Source: [123]

The gear-encoder combination provides 115700 electric pulses per revolution. Pulses from the encoder are fed into a custom developed counter circuit (Figure 3.6).

The counter circuit provides format translation from encoded pulse to digital output which can be easily read by the computer.

Figure 3.6 Custom developed counter circuit that monitors DC motor position.

The detailed program that reads the position of the DC motor from the counter circuit is described in Appendix B.

3.5 XFH Measurement with Simple APD Detector and Crystal Analyzer

3.5.1 Measurement on $Pb(Zr_{1/3}Nb_{2/3})O_3(95\%)$ -PbTi(5%) (PZN-PT) Samples

The XFH experimental setup using an APD detector and crystal analyzer shown in Figure 3.1, is widely employed in the traditional XFH measurement method [38, 39]. With this setup, XFH measurements on single crystal $Pb(Zr_{1/3}Nb_{2/3})O_3$(95%)-PbTi(5%) (PZN-PT) samples were performed. Sample together with the DC scanner are loaded in the center of the goniometer, APD detector and a graphite crystal analyzer are mounted on the θ and 2θ scan arm. The APD detector provides a maximum count rate of 1Mcps. Pb Lα line fluorescence at 10.5 keV is used for holography measurements.

The sample crystal is a solid solution of 95 percent $Pb(Zr_{1/3}Nb_{2/3})O_3$ (PZN) and 5 percent $PbTiO_3$ (PT). The solid solution sample has an average grain size of 5μm [124].

Figure 3.7 is a photograph of the crystal. The size of the crystal is about 10x10x1 mm^3.

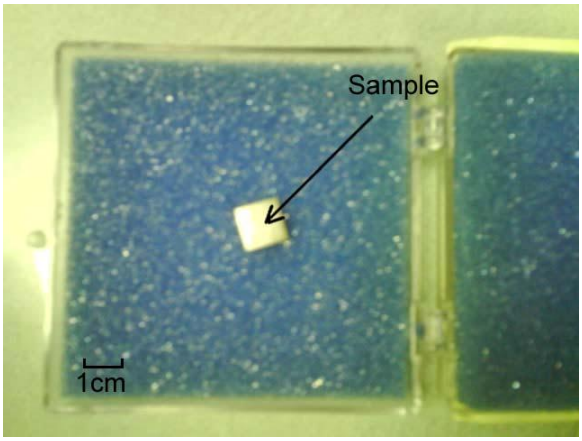

Figure 3.7 A photograph of the PZN-PT crystal.

The holograph is measured with a resolution of 1^o in azimuthal angle and 0.72^o in longitudinal angle. Scans in longitudinal direction are controlled by the DC motor. The scan speed is around 0.2 rev/s. 120 full longitudinal (phi) scans are averaged for each azimuthal angle. It takes about 10 minutes scan time to complete scan of 1^o in azimuthal angle and 10 hours to complete the entire holography scan. This setting gives 60,000 counts on each hologram data point.

A direct scheme XFH measurement is performed at a X-ray incident energy of 14.5 keV. Three indirect scheme measurements are performed at incident X-ray energies of 13.5 keV, 14.0 keV and 14.5 keV. Measurements are repeated several times at each energy to improve statistics.

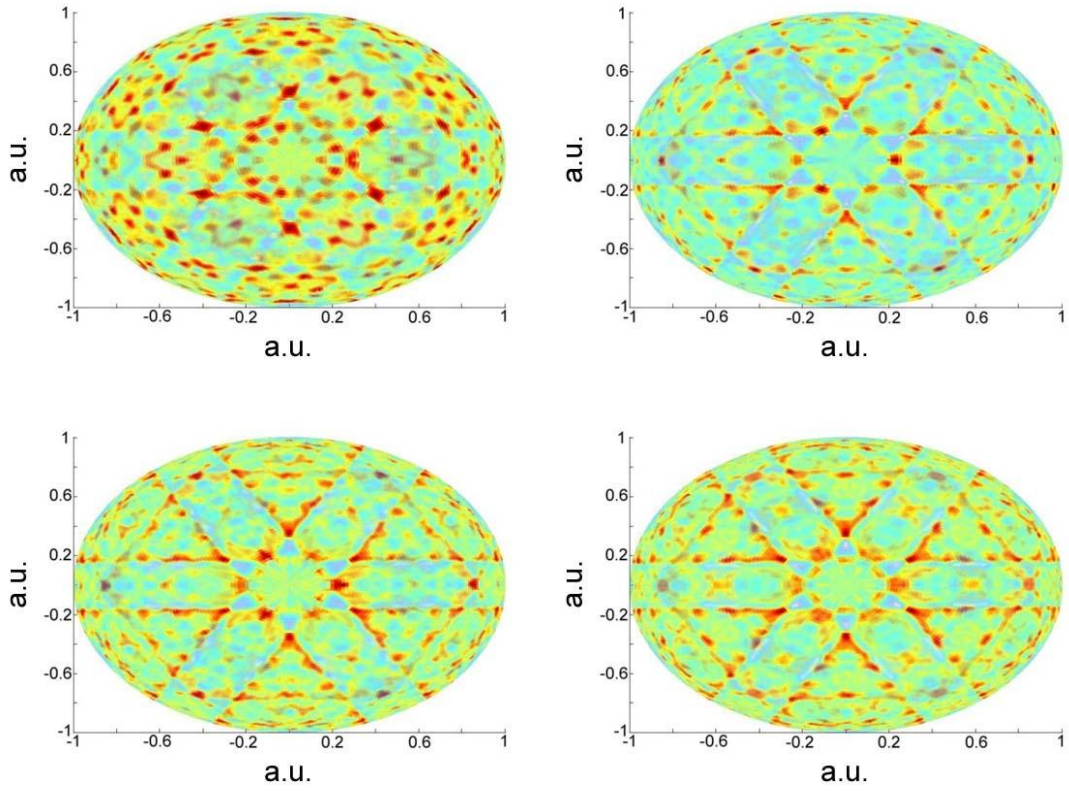

Figure 3.8 Averaged hologram data using symmetrical expansion technique [125] for direct scheme (top left) and indirect scheme at 13.5 keV (top right) 14.0 keV (bottom left) and 14.5 keV (bottom right) X-ray energy.

The raw data are averaged and expanded to 4π solid angle using sample crystalline symmetry. The technique [125] of expanding and averaging raw data requires manually aligning raw data from all measurements to the sample's axis of symmetry. Simple cubic symmetry is used for the PZN-PT sample. Figure 3.8 represents the averaged and expanded holograms from the measurement results. From top to bottom, they are holograms for direct scheme measurement and indirect scheme at 13.5 keV, 14.0 keV and 14.5 keV X-ray energy, respectively.

Data with quality in Figure 3.8 are good enough for the reconstruction via Barton's method [23] with isotropic resolution. The four measured holograms are

reconstructed at multiple energy XFH configuration. The results clearly show the image of each atom. Figure 3.9 shows the real space reconstruction with holograms from Figure 3.8.

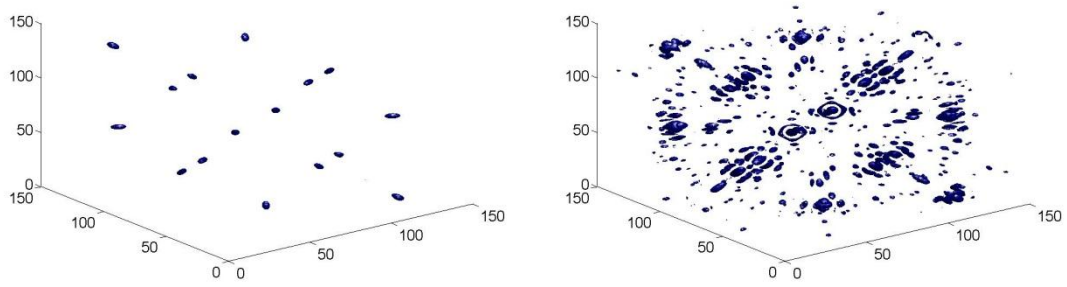

Figure 3.9 Real space reconstructions of PZN-PT holograms (units are in 0.1 Å). Signal is filtered to show only signals larger than 80% (left) of maximum signal intensity and 50% (right) of maximum signal intensity.

The left image in Figure 3.9 shows the plot of signals after noise suppression. So, only the peak signals are displayed. Although the lattice structure is clearly seen when noise is not displayed, actual noise level is more that 50% of maximum signal in the reconstructed image, as shown in the right side image in Figure 3.9.

3.5.2 Measurement on CuAu Sample

XFH measurements on a single crystal CuAu sample are performed together with the experiment on PZN-PT samples, using the same set up and same experimental conditions. A single energy inverse scheme holograph is measured at energy of 14.5 keV. The Cu K_α emission line at 8.0 keV is used in the XFH measurements.

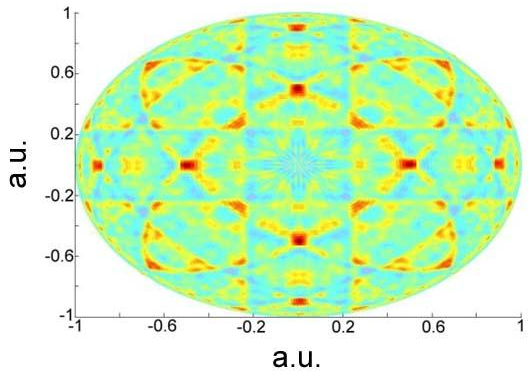

Figure 3.10 Averaged holographic data with symmetrical expansion for AuCu hologram.

Figure 3.10 shows the holographic data expanded and averaged using the symmetrical expansion technique. The hologram is reconstructed with Barton's method in single energy configuration. The reconstructed real space image is shown in Figure 3.11. The contribution due to noise is suppressed in the plot to reveal the structural image.

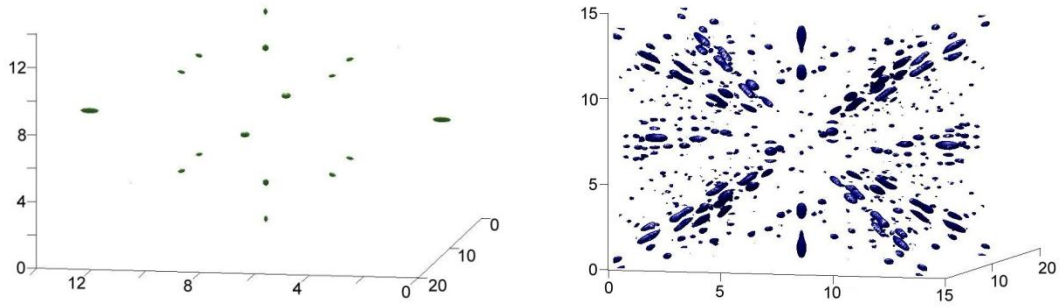

Figure 3.11 Reconstructed image for hologram measured for AuCu sample, units of axes are in Å. Signal is filtered to show only signals larger than 80% (left) of maximum signal intensity and 50% (right) of maximum signal intensity.

3.6 XFH measurement without Crystal Analyzer

Traditional XFH measurement requires a crystal analyzer for providing energy resolution. Use of a crystal analyzer is not desirable in XFH experiments because it increases the

distance between the fluorescent sample and the detector, thus in turn reducing the efficiency of the photon collection. XFH measurement setup using detectors with energy resolutions without crystal analyzer is thus a promising direction for XFH instrumentation development.

In order to verify the concept of XFH measurement without a crystal analyzer, XFH measurements with a commercially available single channel silicon drift detector (SSD) [126] were performed. This allowed the detector to be placed close to the sample without a crystal analyzer and offered a very large acceptance angle and thus fast counting rate. The challenge is how to distinguish fluorescence from elastic photons that enter into the detector. The setup for this measurement is shown in Figure 3.12. In order to suppress influence from elastic photons, the detector is placed parallel to the direction of polarization to minimize elastic scattering. The X14A beamline X-ray has a horizontal polarization since it is a synchrotron bending magnet beamline.

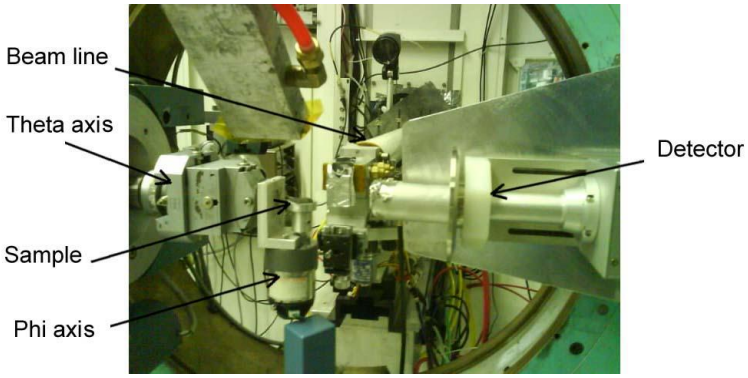

Figure 3.12 Set up of detector without crystal analyzer.

Electric pulses from the detector that represent detected photons are then processed by a pair of Single-Channel Analyzer (Tennelec Tc450 SCA). Fluorescent photons and elastic photons are counted in respective channels. Since the detector is

working near the saturation region at high count rate for XFH measurements, any elastic photons entering the detector will bring in extra dead time to the detector. Thus, for every bright spot (high count rate) in the elastic photon channel, there is a dark spot (low count rate) in the fluorescence channel, as is shown in Figure 3.13. This influence can be removed numerically by correlating the two channels. Dead time correction is performed on elastic channel count rate using count rate from inelastic channel. Using detectors with larger dynamic range will provide a big improvement in linearity at high count rate.

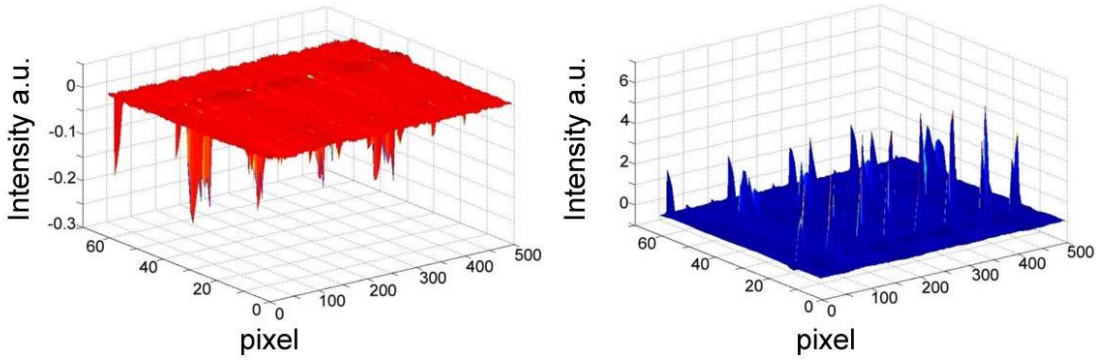

Figure 3.13 Signal from fluorescense channel (red) and elastic channel (blue).

A Ge doped Si single crystal Si-$Ge_{10\%}$ sample is used as the fluorescent sample for this XFH measurement. Fluorescence from germanium K_α line (9.8 keV) is used in XFH measurement. Figure 3.14 is the measured hologram after the influence of elastic photon has been removed Kossel lines can be seen clearly in the image.

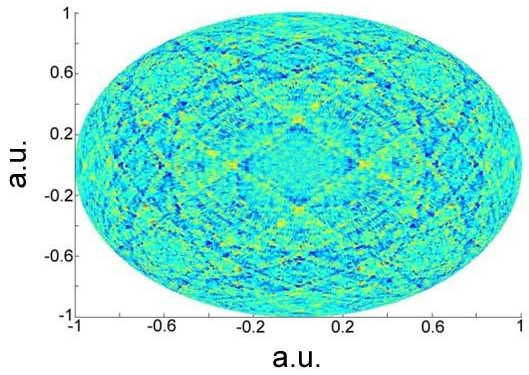

Figure 3.14 The measured hologram of Si-$Ge_{10\%}$ sample after the influence of elastic photons has been removed.

Noise in the resulting XFH hologram is relatively high partially due to statistical noise from low photon counts and partially due to incomplete removal of dead time caused by elastic scattering photons.

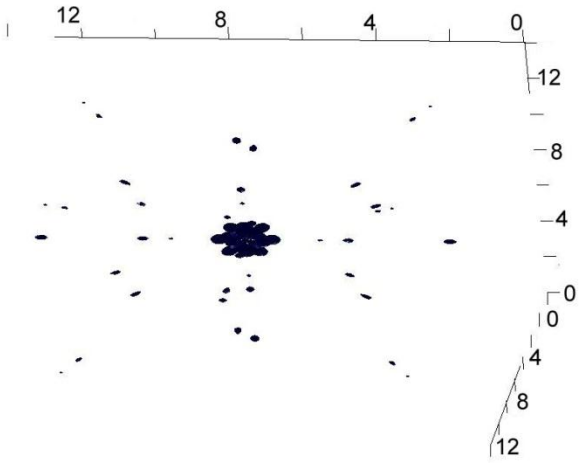

Figure 3.15 Reconstruction image representing electron density in the Si-$Ge_{10\%}$ sample, unit of axes are in Å.

Figure 3.15 is a 3D reconstruction image from the measured hologram of the Si-$Ge_{10\%}$ sample. The result shows a BCC structure rather than a diamond structure for the silicon lattice. It is worth mentioning that the symmetry applied to the data during symmetrical expansion is not the reason for this discrepancy. The difference between the

real electron density and the image is due to the nature of XFH measurement that all possible scattering signals are averaged. Thus, the diamond structure in silicon lattice is seen as a BCC structure in XFH measurements.

3.7 Design and Development of a Novel HERMES ASIC Based 384 Element Detector and its Cooling System

3.7.1 The 384 Element HERMES Detector Circuit

Novel detectors have been developed in this research based on National Synchrotron Light Source (NSLS) High Energy Resolution Multiple Element Silicon (HERMES) detector ASIC circuit [127]. The HERMES ASIC is a 32 channel signal processing unit that provides read out circuitry and energy resolution power for silicon detectors.

Figure 3.16 is a picture of the HERMES ASIC. This ASIC is composed of 32 identical signal processing channels. Each channel is segmented into 4 components, as shown in the photograph and shown in Figure 3.17.

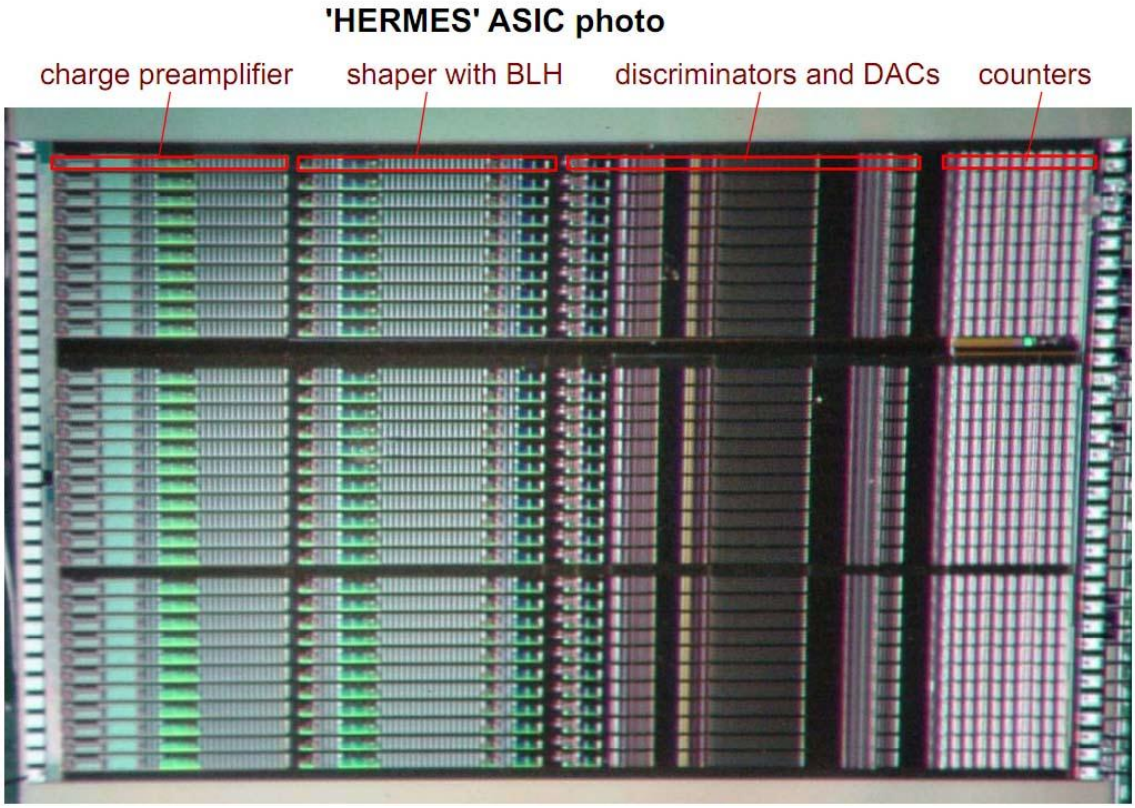

Figure 3.16 A photograph of HERMES ASIC channels.

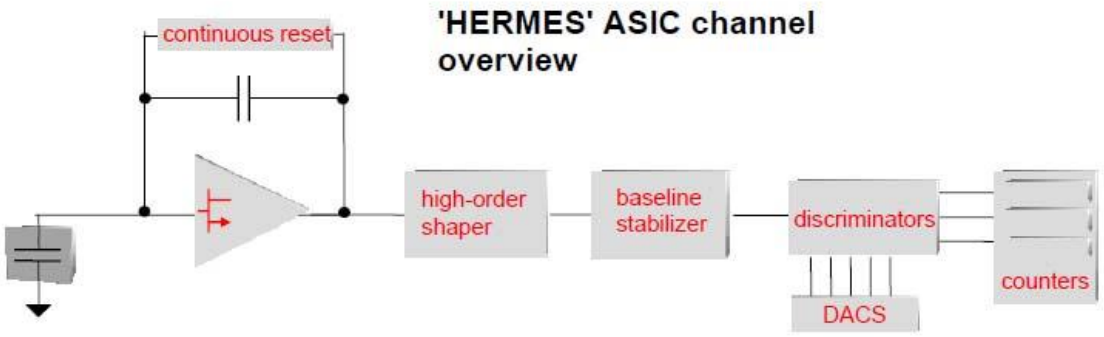

Figure 3.17 HERMES ASIC channel components overview.

Figure 3.17 is a block diagram that shows the components in the signal processing channel. The input stage amplifier is a charge sensitive p-MOSFET amplifier with continuous reset circuit [109]. Amplified signal is then passed into a high-order shaper

and a baseline stabilizer [110]. Signals at this stage can be read out with a Multi-Channel Analyzer (MCA) for spectral analysis as the setup in Section 3.6. Instead of supplying 32 independent MCAs for the 32 signal processing channels, 32 discriminators are built into the ASIC to provide energy discrimination. The discriminators are controlled by 6 bit DACs and digital logic and provide three energy analyzer channels within each signal processing channel. A 24 bit counter is provided to record counting rates in each energy analyzer channel in each detector signal processing channel.

Figure 3.18 and Figure 3.19 show schematic and printed circuit board (PCB) layout diagram for the HERMES based 384 element detector. The components in the schematic and PCB of the 384 element detector contain HERMES ASIC and several power supply units. Digital and analog data and control signals are directly connected from the HERMES ASIC to outside connectors on the 384 element detector PCB.

The digital and analog signals from the 384 element detector PCB can be collected and processed by general equipment such as a computer or oscilloscope.

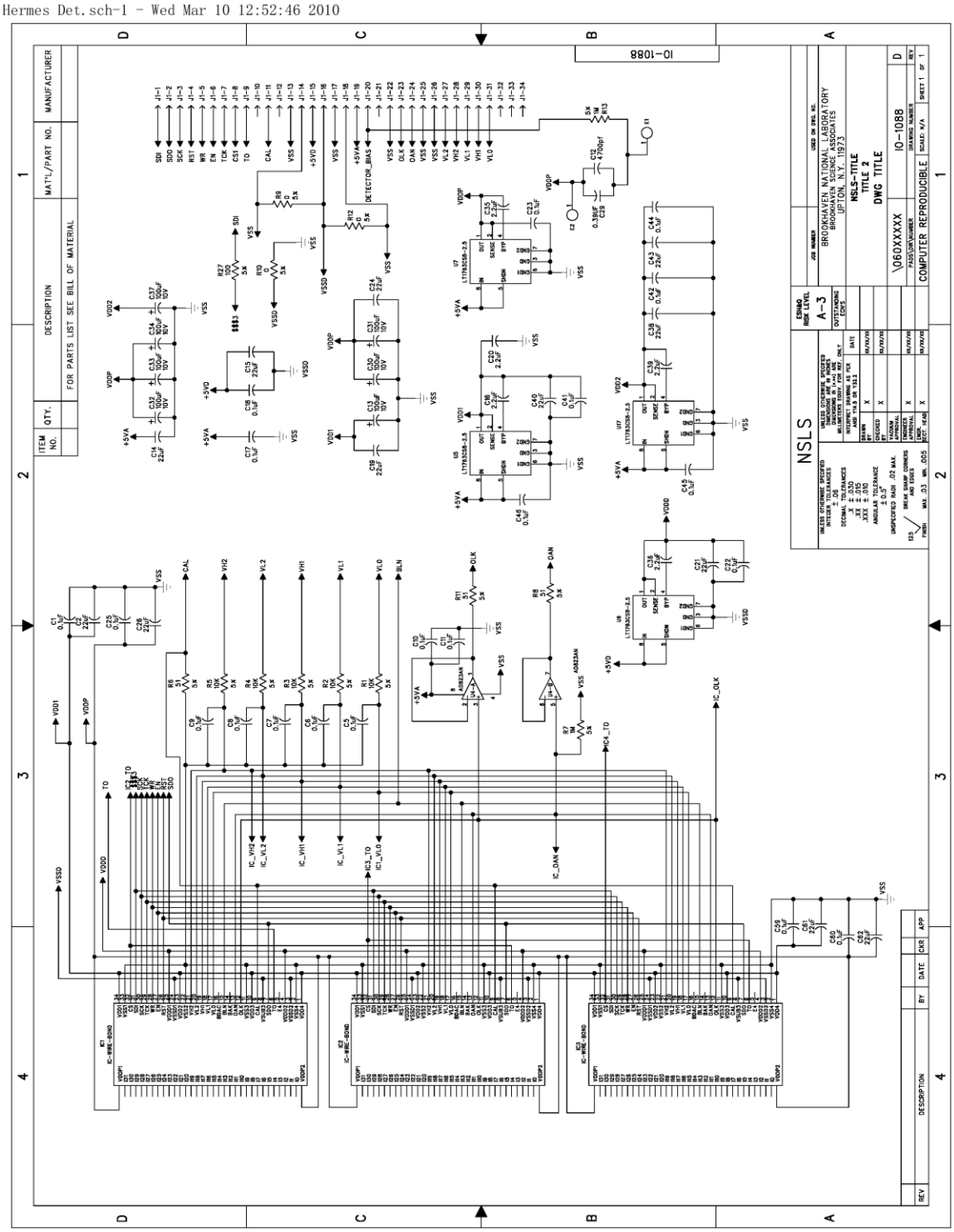

Figure 3.18 Schematic design of the HERMES based 384 element silicon detector.

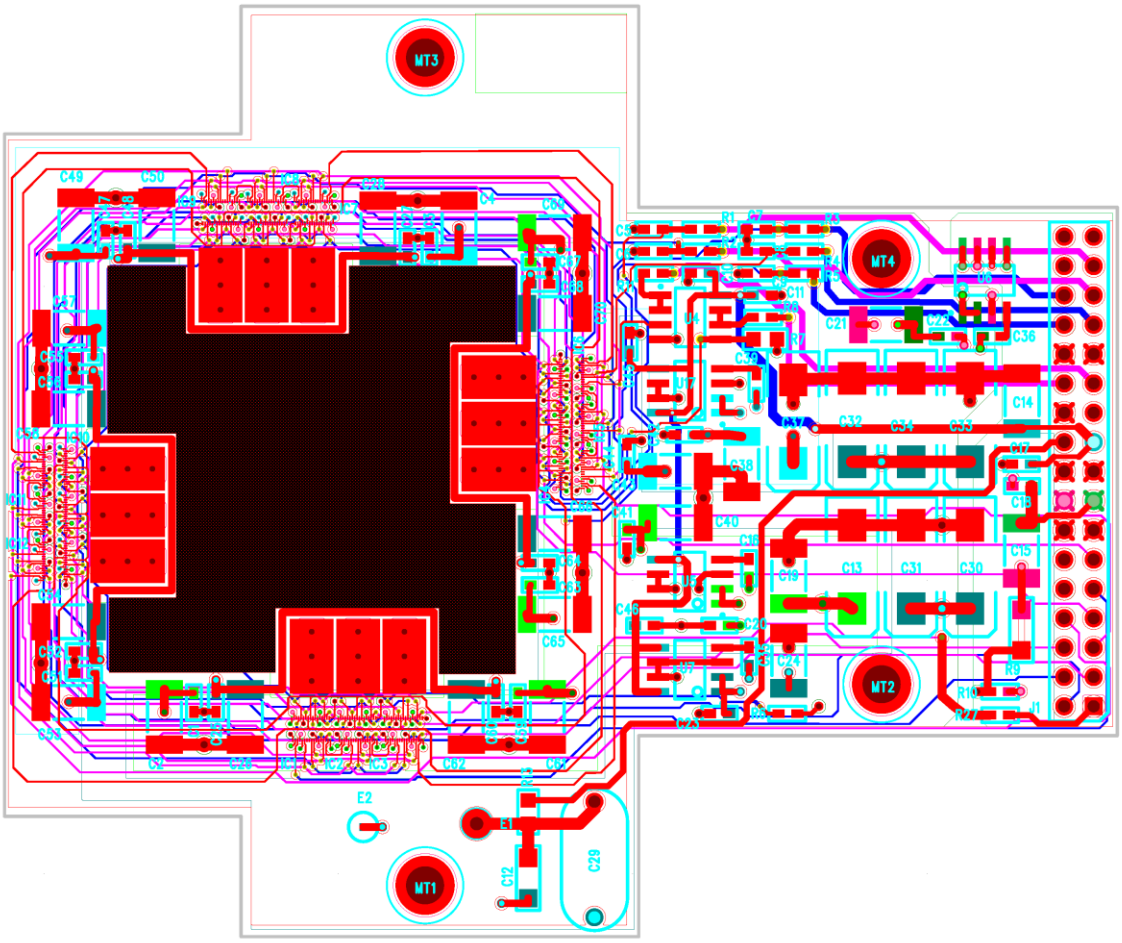

Figure 3.19 Printed Circuit Board layout of the HERMES based 384 element silicon detector.

3.7.2 Cooling System Developed for the HERMES 384 Element Detector

The HERMES based silicon detector requires a cooling system to work at ~-40^{o}C. A novel cooling system design is assembled and tested. The cooling system (Figure 3.20) employs an Aluminum Nitride (AlN) block as a heat sink and supporting device. Aluminum Nitride has no major X-ray fluorescence at hard X-ray energies and has thermal conductivity of 285 W/(m K) (70% of copper) and thermal expansion coefficient (4.5×10^{-6}/K) comparable to silicon (2.6×10^{-6}/K). Since copper (Cu) has much higher thermal expansion coefficient (17×10^{-6}/K) than AlN, and copper works at a temperature

different from the aluminum nitride block, stress could build up during operation due to thermal expansion and contraction. A flexible design at the components to accommodate changes in size caused by thermal expansion and contraction is used. The copper and aluminum nitride parts are connected by Peltier cooling units at the 4 corners of the AlN block, as shown in Figure 3.21. The aluminum nitride unit is displayed in yellow and the copper part is displayed in gray. The blue color in Figure 3.20 represents the passage of cooling water.

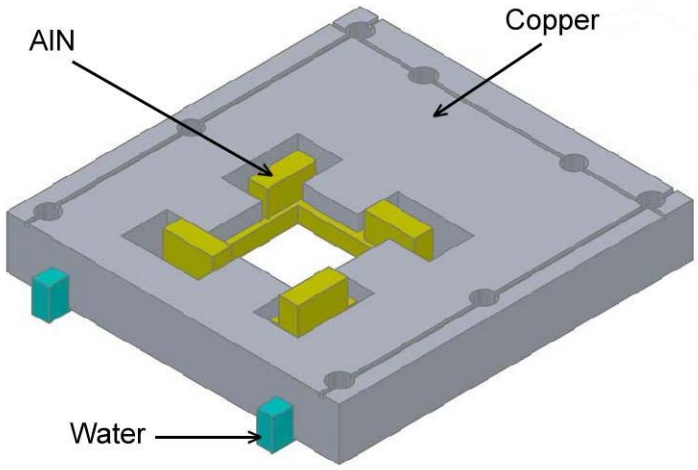

Figure 3.20 Design concept of Cu-AlN cooling system.

Figure 3.21 is a bottom view photograph of the cooling system. The water cooled copper frame is used as a 5^{o}C heat sink. Four custom ordered 2-stage Peltier cooling devices with 1x1 cm^{2} working area are used to cool the AlN block to -50^{o}C and provide mechanical connection from the copper frame to the aluminum nitride block. The connection is made by thermal conductive resin. A small rotational motion can reduce stress while thermal expansion causes stress between copper and aluminum nitride block.

A silicon wafer is used to simulate the detector sensor. A thermistor is glued on the aluminum nitride block to monitor temperature.

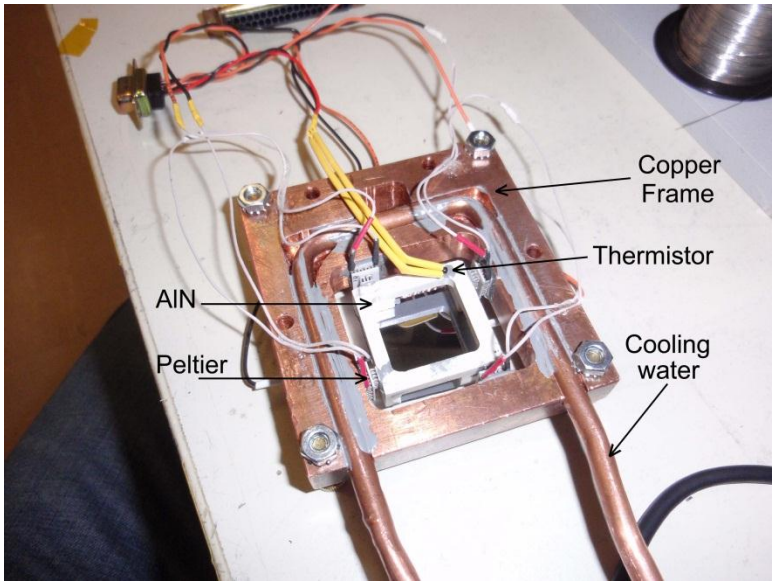

Figure 3.21 Bottom view photograph of the cooling system.

Figure 3.22 is a top view of the cooling system; a resistor is glued on the silicon wafer to simulate actual heat load on the detector system.

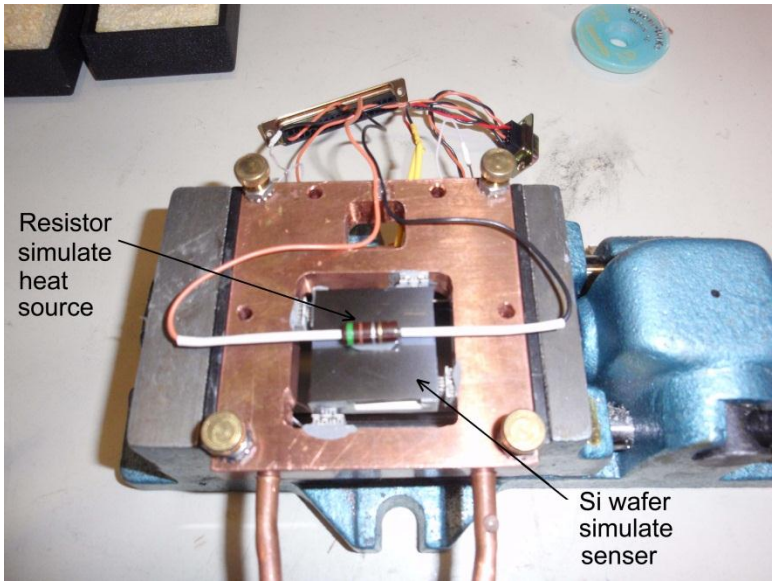

Figure 3.22 Top view photograph of the cooling system.

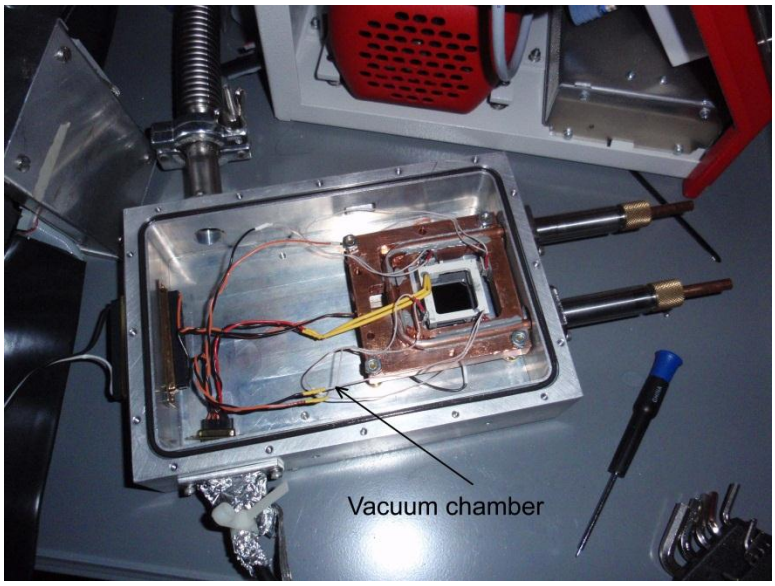

Figure 3.23 Photograph of the vacuum tight box for the HERMES 384 element detector.

The cooling system is tested in a detector vacuum box at a vacuum condition of 10^{-6} mbar. Figure 3.23 is a photograph of the vacuum chamber for the HERMES 384 element detector in the actual testing setup.

Testing of the power of the cooling system and its stability over repeated heat cycles is of our interest. The cooling system was put through 1150 heat cycles during 14 days of continuous operation. No power was supplied to the heat load resistor on the silicon wafer during the stability test. The power supplies for the Peltier coolers were turned on and off every 10 minutes and temperature was monitored.

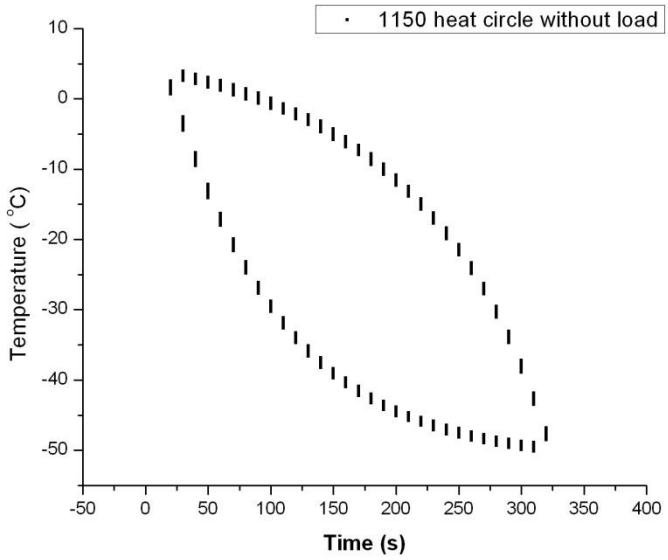

Figure 3.24 Temperature versus time in heat cycles.

Figure 3.24 shows temperature variation as a function of time during the 1150 heat cycles. Figure 3.25 shows maximum and minimum temperature in heat cycles. It is assumed that any failure caused by fatigue or any other defect should cause reduction in the cooling power. Since Figure 3.25 shows no reduction in the cooling power, it is concluded that the test system is stable, showing no mechanical fatigue for 1150 heat cycles.

Figure 3.26 is a plot of temperature versus load heat power curve measured after stability test. The cooling system keeps the temperature at -46^{o}C at a load of 500 mW. The actual heat load in the detector is estimated to be around 400 mW.

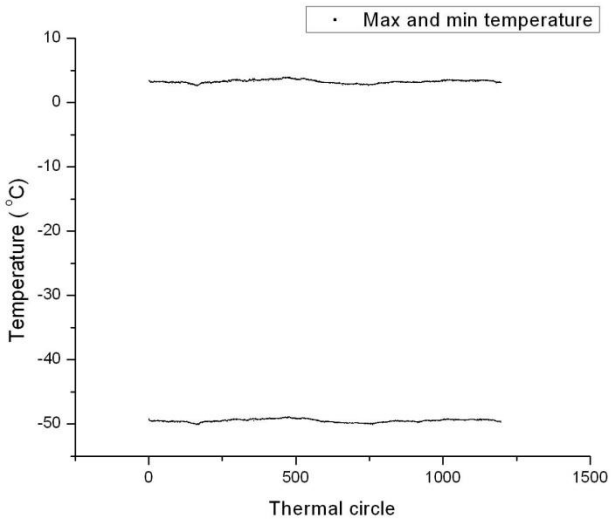

Figure 3.25 Maximum and minimum temperature in heat cycles.

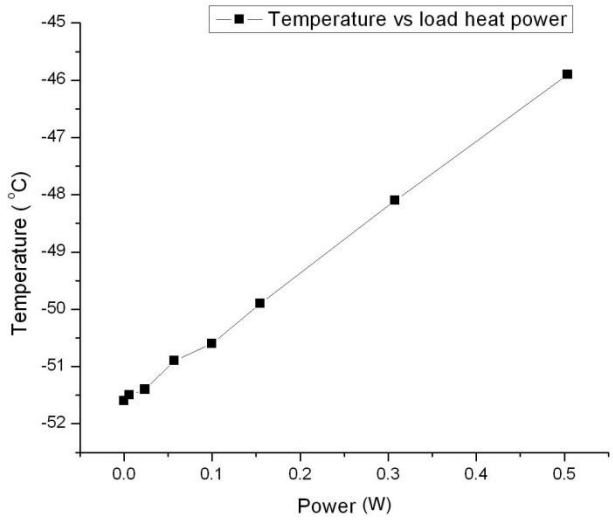

Figure 3.26 Temperature versus heat load.

Figures 3.27 and 3.28 are dimensions and design of the AlN and Cu parts of the cooling system.

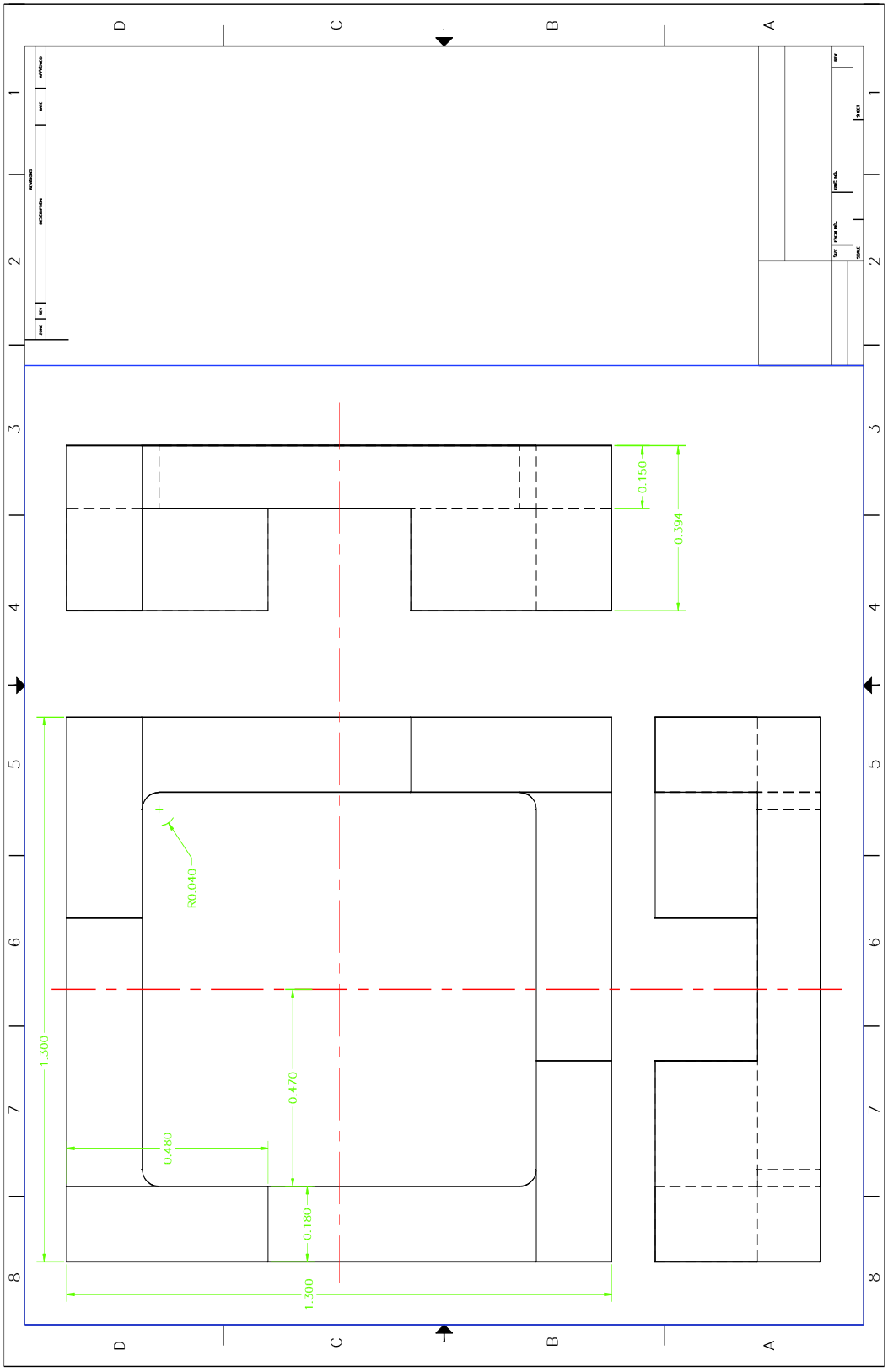

Figure 3.27 Dimensions (in inch) of the aluminum nitride frame in cooling system.

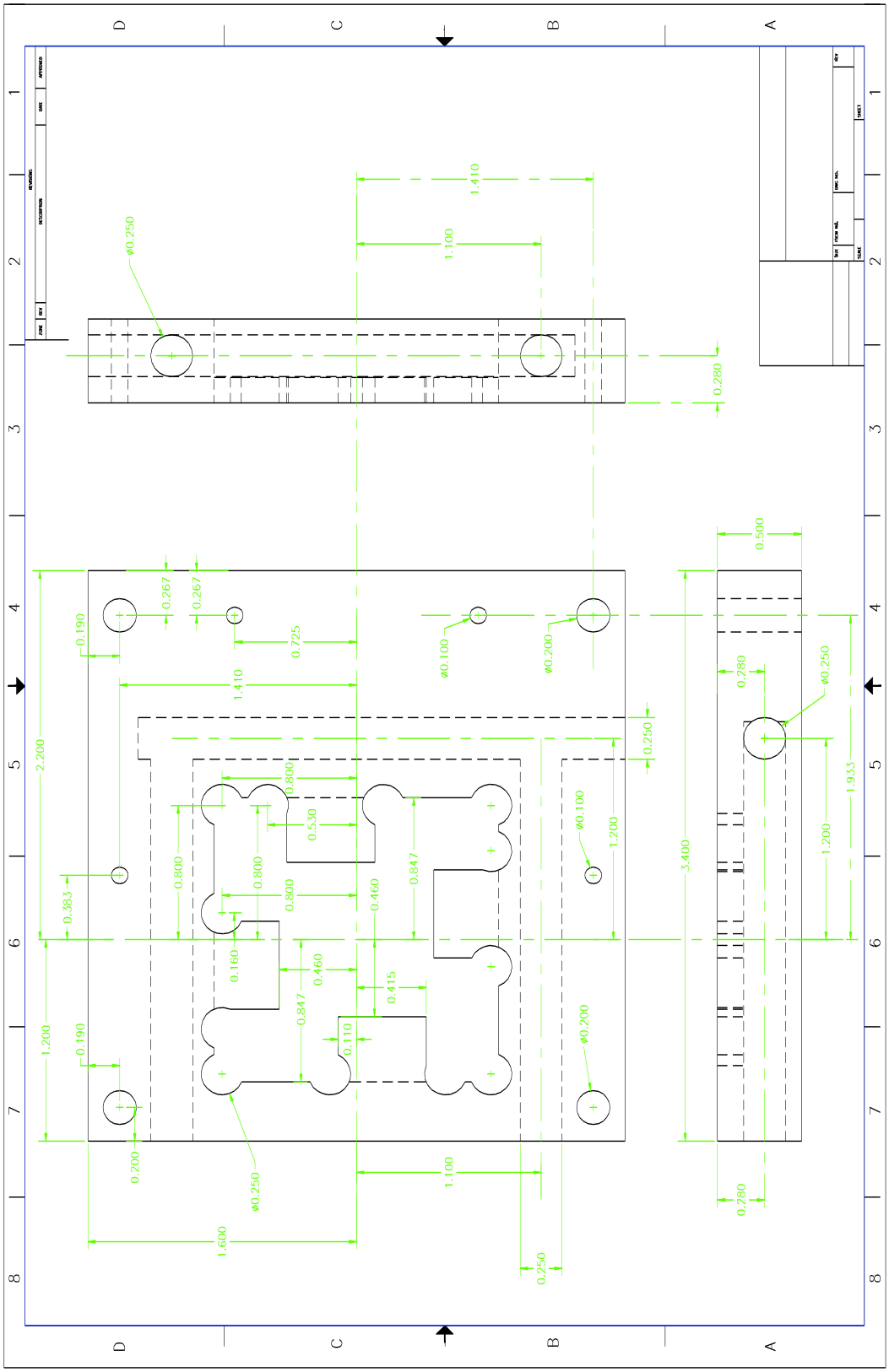

Figure 3.28 Dimensions (in inch) of the copper part in cooling system.

3.8 Observing X-ray Fluorescence with Multi-element Detector with Energy Resolution

A 384 element X-ray detector is developed based on BNL designed HERMES (High Energy Resolution Multi-Element Silicon) ASIC [128]. The detector is configured into a square shape with an active area of 0.85 inch^2. 384 PIN diode elements are arranged in this area. The detector provides energy resolution up to 200 eV for low count rates but resolution decreases as count rate increases [127]. 384 independent channels of read out ASIC are connected directly to the diodes by wire bonding to provide spatial resolution. Figure 3.29 is a photograph of the detector.

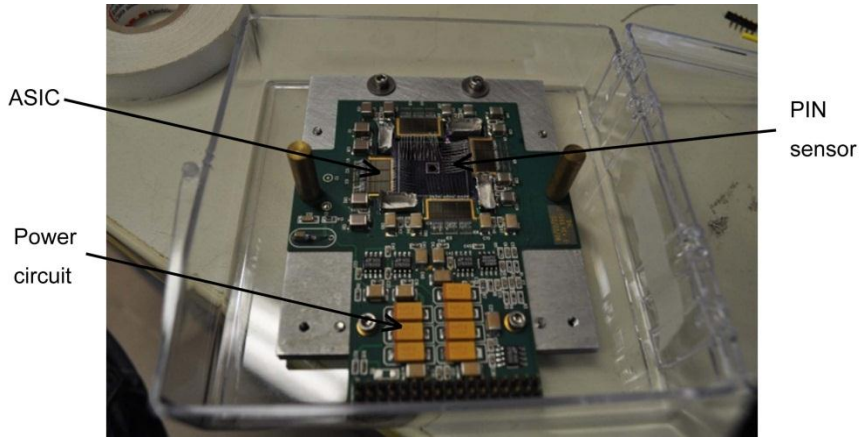

Figure 3.29 The HERMES based multi-element silicon detector.

The new detector was installed at NSLS X14A beamline. Figure 3.30 is a photograph of the XFH setup. The detector is placed at a distance of 1.3 inch from the sample. This setup allows 3.7% of the total fluorescence radiation to be detected.

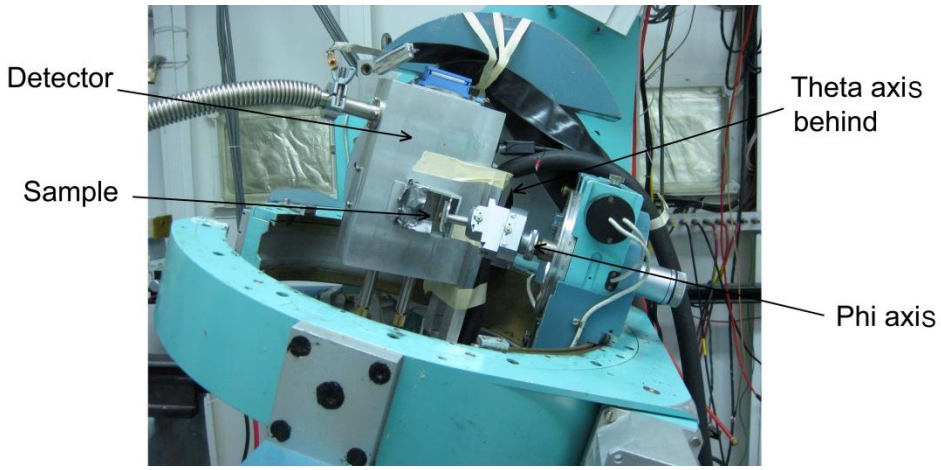

Figure 3.30 XFH setup in beamline X14A at NSLS.

The above setup is configured for inverse XFH experiment only. Sample and detector will scan an azimuthal angle (theta) together, and sample will scan independently on a longitudinal angle. The signal from the 384 element detector will give a holograph pattern which is a mixture of inverse scheme holograph and direct scheme signal in the longitudinal direction. Inverse scheme holograph can be extracted using standard methods [125].

The acquired signal can be considered to be 384 individual holographs or a single holograph if the total counts are inregraded.

3.8.1 Noise Level

Fluorescence data are taken in 384 channels simultaneously and added up directly to give a total count number from the detector. A static stability test using the Si-$Ge_{10\%}$ sample was conducted at 14.5 keV. The stability test measures fluorescence without moving the orientation of the sample or detector.

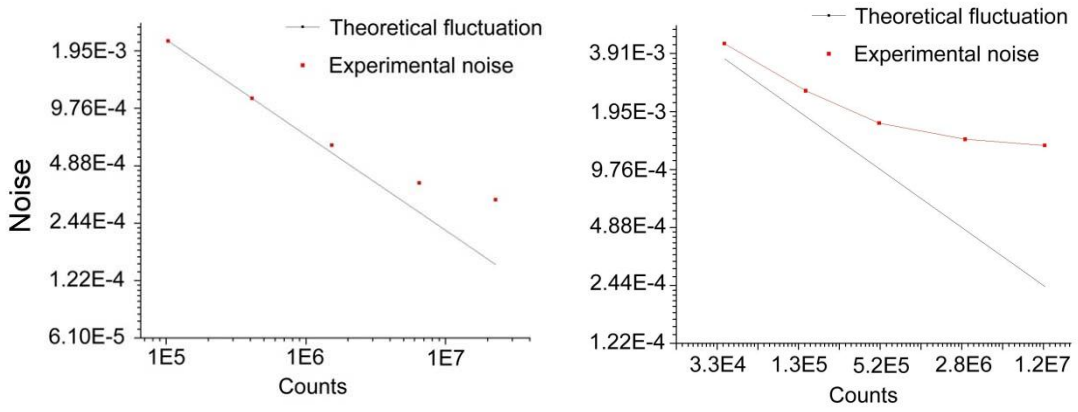

Figure 3.31 Noise level and stability measurement on Si-$Ge_{10\%}$ sample for count rate of 100,000 cps per channel (left) and 35,000 cps per channel (right).

Figure 3.31 gives the relationship between noise level and accumulated photon counts. The minimum noise value in the stability test is $3x10^{-4}$ relative to the signal intensity. This noise value is sufficiently low to give a clean XFH measurement for samples containing heavy elements and thus signals stronger than $1x10^{-3}$. The noise is attributed to electrical interference, synchronization and noises other than statistical noise.

Figure 3.32 is the spectrum of Si-$Ge_{10\%}$ measured by a MCA analyzer connected to the analog output signal from the HERMES detector. Ge K_α (9.8 keV) and K_β (10.9 keV) lines are visible in the spectrum.

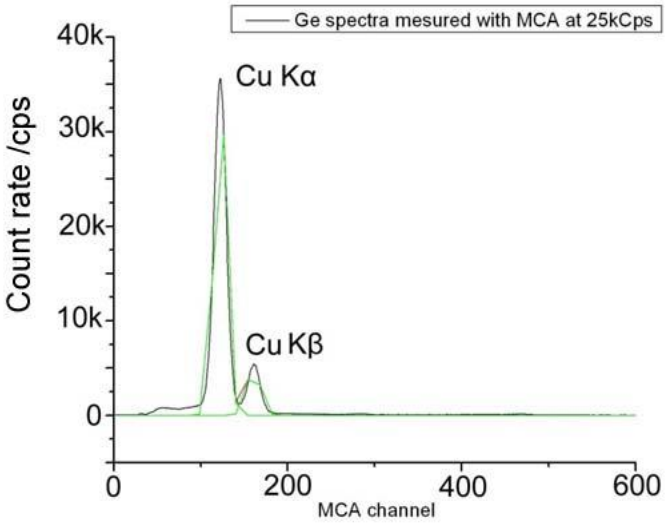

Figure 3.32 Fluorescence in Si-$Ge_{10\%}$ sample.

3.8.2 Measurement of Holograph on $Pb(Zr_{1/3}Nb_{2/3})O_3$(95%) -PbTi(5%) Sample

A single crystal $Pb(Zr_{1/3}Nb_{2/3})O_3$(95%) –$PbTiO_3$(5%) (PZN-PT) sample is studied with the above XFH setup. Pb is selected as the fluorescent element in the sample.

Figure 3.33 gives spectra of sample fluorescence detected with the multi-element detector. The two major peaks are Pb L_α line at 10.5 keV and Pb L_β line at 12.6 keV. Only signal from these two peaks are used in the holograph measurement. The elastic X-ray energy is at 16.2 keV and is strong only in individual pixels whose orientation satisfies Bragg's condition. The resolution at 50,000 Cps and 100,000 Cps is about 500 eV. The detector suffers resolution degradation when the count rate is large.

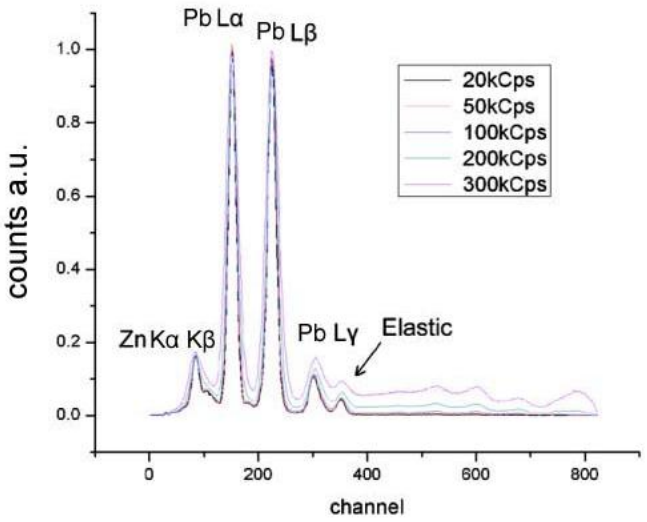

Figure 3.33 Fluorescent spectra of PZN-PT sample measured by HERMES based 384 element detector with MCA analyzer.

3.8.3 XFH Measurement Results

The 384 element detector is used is a configuration similar to a single element detector described in section 3.6. Photons from both fluorescence X-ray and elastic scattering would be picked up by the detector. The total photon count is thus a summation of the XFH holograph and the elastic scattering (Figure 3.34).

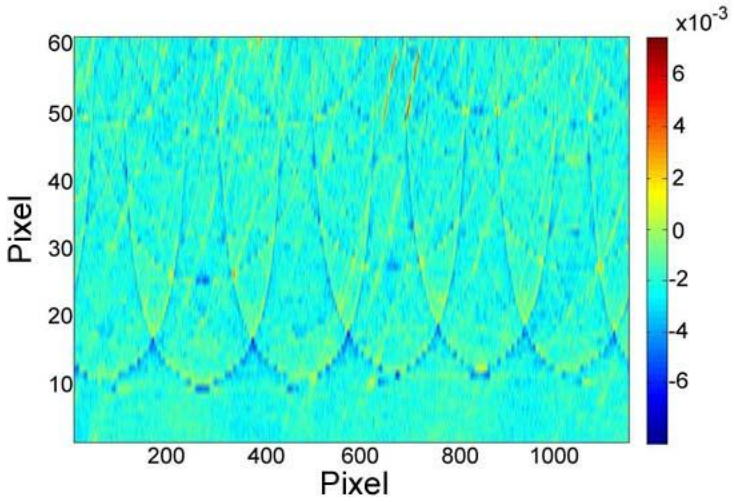

Figure 3.34 Total count signal of PZN-PT sample XFH measurements for the whole spectrum, containing both fluorescence signals and elastic signals.

Elastic scattering signals have to be separated from the hologram signal. One can use the same method as shown in Section 3.6. Using the energy resolution in HERMES detector, one can extract fluorescence photons from the whole photon spectrum and count signals for fluorescence X-rays.

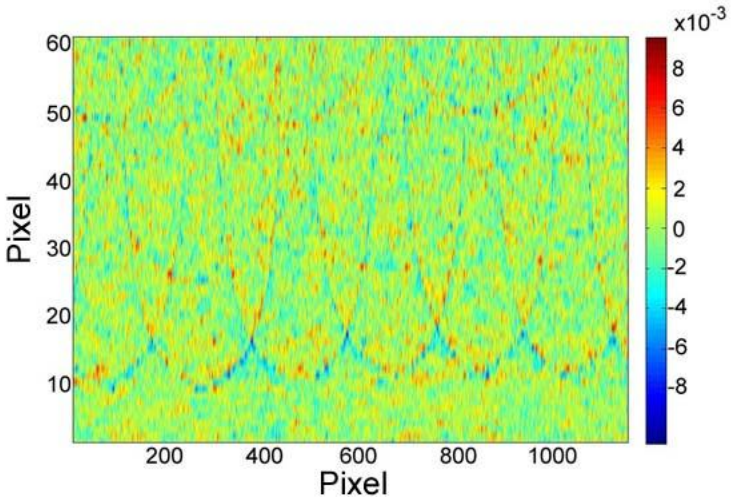

Figure 3.35 PZN-PT sample holograph processed from sum of two energy windows of HERMES based 384 channel detectors. The two energy windows are set to Pb L_α line (10.5 keV) and Pb L_β line (12.6 keV).

Figure 3.35 is a measured holograph using energy resolution to remove elastic scattering. The result has a spike like noise pattern with peak noise level at 10^{-2}. The high noise is due to poor energy resolution in the detector. This noise has made the result worse than results from a single energy detector.

Strong elastic scattering of single crystal sample happens only at diffraction angle close to Bragg's condition. For the large active area of the HERMES 384 element detector, at each orientation of XFH scan, only a few detector elements suffer influence of elastic scattering while the majority of elements are not influenced. This can be used to provide a method to remove elastic scattering signals even without using energy resolution in multi-element detectors.

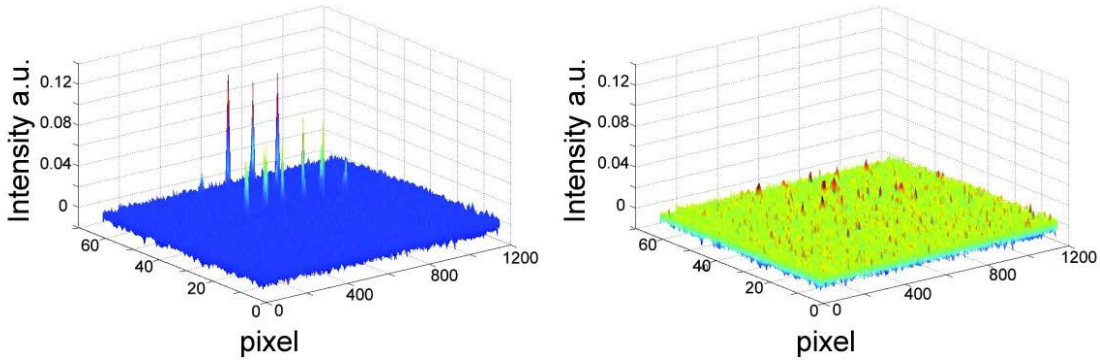

Figure 3.36 XFH total signals of all photon energy with elastic scattering signal shown as spikes (left) and after the spike shaped elastic signals are identified and removed (right).

In Figure 3.36, XFH measurement signal from a single element of the multi-element detector is displayed. Elastic signal in the Figure 3.36 are spike shaped and can be easily identified. The elastic photon influenced region for each element can be removed by putting a weight factor of 0 when averaging signals over all detector elements. Because different detector elements have different orientations that affect the elastic scattering count rate, the total average over 384 elements will eliminate elastic photon signals. Thus fluorescence photon signals can be extracted without using energy resolution in the HERMES detector.

Figure 3.37 is the extracted hologram from PZN-PT sample without using energy resolution. Elastic photons are removed from the signal. The measurement gives a holograph with noise level of 10^{-3}, which corresponds to data of the best quality that have been achieved. Noise in the picture does not show any obvious pattern.

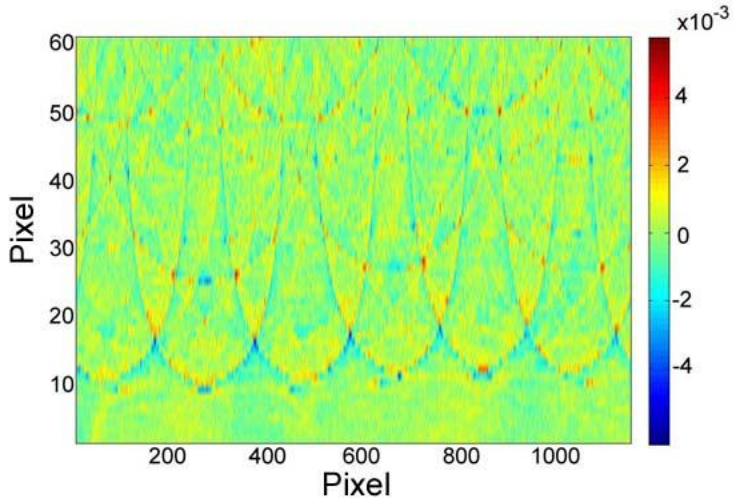

Figure 3.37 Hologram of PZN-PT sample processed from weighted average of 384 element detector signals with elastic photons removed.

The hologram in Figure 3.37 is reconstructed with Barton's algorithm. The resulting real space structural image for PZN-PT sample is shown in Figure 3.38. Noises is suppressed in the display of the image on the left.

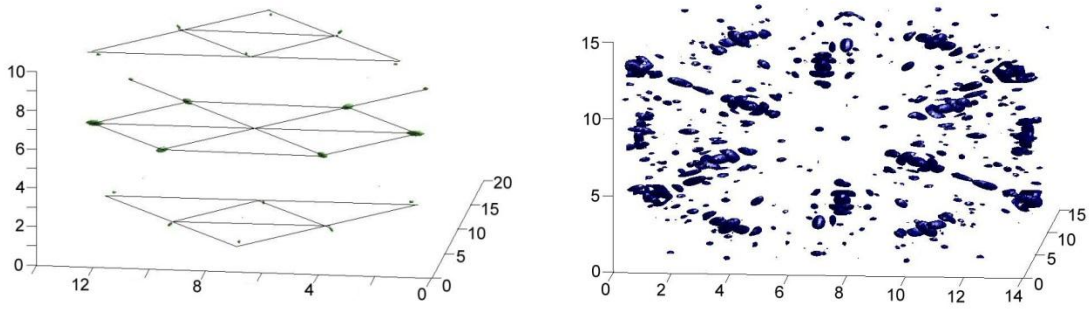

Figure 3.38 Real space image reconstructed from single energy PZN-PT hologram, unit of axes are in Å. Noise is supressed to show only signals larger than 80% (left) of maximum signal intensity and 50% (right) of maximum signal intensity.

3.9 Conclusions

In this study, fast and low noise XFH measurements are setup in beamline X14A at NSLS. A beamline stability issue is solved with automatic algorithm that tunes optics in

the monochromator to the best condition. A custom developed DC motor with encoder is used to provide continuous scan capability which is not available on the step motor based goniometer.

Multi-element PIN diodes dedicated to the XFH experiment has been built. The detectors show reasonable energy resolution and have a very large dynamic range. XFH measurements on $Pb(Zn_{1/3}Nb_{2/3})O_3(95\%)$ -$PbTiO_3(5\%)$ sample were performed to verify the feasibility of XFH experiment with multi-element detector. The mixed direct scheme holograph signals, as well as elastic bright peak were successfully separated from the holographic signal in acquired data. The holograph has acceptable quality. A reconstruction of the holograph is consistent with sample structure.

The resulting holograph has noise higher than statistics but sufficient for holograph measurement and reconstruction. The extra noise is due to detector noise, beamline fluctuation, difficulty in removing mixed elastic scattering signals and dead time correction.

The noise level of holograph can be readily improved as the system is further developed. The detector needs to be improved to reduce noise level and enhance the energy resolution.

The XFH method with multi-element PIN diodes is a promising technology and will be developed further in the future.

CHAPTER 4

DIRECT EXTRACTION OF QUANTITATIVE STRUCTURAL INFORMATION FROM X-RAY FLUORESCENCE HOLOGRAMS USING SPHERICAL HARMONIC ANALYSIS

4.1 Introduction

X-ray Fluorescence Holography (XFH) is a promising technique for model-independent structure determination from single crystals. Unlike standard X-ray diffraction (XRD) methods that measure only the magnitude of the structure factors and require significant priori knowledge of the crystal structure for generating a solution, XFH provides both the amplitude and phase of the structure factor. However, even though the first experimental XFH measurement was realized fifteen years ago [38, 39], and data collection procedures have greatly improved with the advent of high flux third generation synchrotron sources, there still are no effective methods for retrieving quantitative structural information from X-ray holograms.

Since X-ray scattering methods, such as XFH and XRD, are sensitive mainly to electrons, the complete structural information of a crystal obtained with these methods can be represented by a 3-dimensional density distribution of electron charge, or its Fourier transformation in the reciprocal space, viz., the complex structure factors.

Previous work widely used Barton's method [23], an atomic image reconstruction algorithm based on the Helmholtz-Kirchhoff integral theorem, for analyzing XFH data. The 3D image calculated with Barton's method is the wave field amplitude around the fluorescence emitting atoms formed by a fictitious converging spherical wave through the recorded hologram. This image assumes maxima at atomic positions, but is distorted because of interference between the scattered waves. The interference artifacts can be

suppressed by summing multiple energy XFH data [39]. However, the resulting image differs significantly from the true charge density of a material. Typically, it is extremely difficult, if not impossible, to solve unknown structures or to do any quantitative structural analysis with XFH data using Barton's method.

Much effort has been invested in developing methods to extract the electron density directly from an XFH measurement. Chukhovskii et al. [52] proposed a Fourier transform type algorithm to derive the distribution of electron charge density from XFH data. Their results using a single wavelength hologram are similar to, but have better spatial resolution than those obtained with Barton's method. Seemingly, the algorithm can restore the true electron charge density from data taken with a suitably large energy range; however, this is impractical with current experimental approaches. Marchesini et al. [129] proposed an iterative image deconvolution method to construct the electron charge density from XFH data. They demonstrated the method by approximating the atoms in the crystal as point charges. However, there is no proof that their iterative procedure will converge to the true electron charge density. Matsushita el al. [68, 69] developed a 'scattering pattern matrix' method to derive a 3D atomic distribution function defined in real space from the 2D hologram taken in k space with the iterative-scaling algorithm of maximum-entropy. By using the non-negative constraint, and imposing translational symmetry of the atomic distribution function, they successfully reconstructed atomic images from measured XFH holograms without significant artifacts. However, this atomic distribution function is not related to the electron charge density and cannot be used to solve unknown structures without pre-assigning atomic species on individual atomic sites. Chukhovskii et al. [130, 131] defined a scattering function

connecting the XFH hologram function to the structure factors. Using standard least square methods, they retrieved a set of structure factors from a XFH hologram simulated with the same set of structure factors. This formalism needs to be tested with more realistic model holograms based on real space atomic configurations. As indicated later, each XFH hologram can be expressed by a complete set of structure factors with a finite number limited by the energy of the scattered waves. The complete set of structure factors is needed to avoid truncation errors in the XFH structure analysis.

In this chapter, a formalism connecting the structure factors to the spherical harmonic components of XFH holograms via a set of linear equations is present. The electron density is then obtained by Fourier expansion, using the structure factors resolved by directly solving the linear equations. The advantage of using a spherical harmonic expansion lies in the fact that each spherical harmonic component represents a weighted integration of the hologram on the surface of a sphere in k-space, analogous to the integrated intensity of the Bragg peaks in X-ray diffraction. As Warren [132] noted, intensity as a function of the diffraction angle, usually is not an observable quantity; rather the integrated intensity is more useful since it can be both calculated and measured. In XFH, each spherical harmonic component of the hologram is a well-defined quantity, expressible as a linear expansion of structure factors with a well behaved scattering matrix. Using the spherical harmonic method allows us to retrieve the structure factors from holograms modeled with real space atomic configurations, and with these structure factors, the electron charge density can be reconstructed with high fidelity.

4.2 Theoretical Considerations

The X-ray fluorescence hologram for a polarized probing wave can be expressed as [56, 133]:

$$\chi(\vec{k}) = \iiint \frac{\rho(\vec{r})\left(r_e \mathrm{Exp}(ikr - i\vec{k}\cdot\vec{r})\right)}{r}[A(r) + B(r)(\boldsymbol{\epsilon}\cdot\hat{r})^2]\,d\vec{r} + C.C. \qquad (4.1)$$

where, $\chi(\vec{k})$ represents holograph χ in k-space, $\rho(\vec{r})$ is electron density distribution in real space, r_e is the classical electron radius, $[A(r) + B(r)(\epsilon\cdot\hat{r})^2]$ is a generalized expression for the scattering factor between the polarized photon and electron, $\vec{r}$ represents the position of the scattering electron relative to the fluorescent center at $\vec{r} = 0$, $\boldsymbol{\epsilon}$ is the unit vector for direction of the electric field, and $\hat{r}$ is the direction of $\vec{r}$. Considering near field effect (the deviations from plane wave behavior of the probing waves), $A(r) = \frac{ik}{r} - \frac{1}{r^2} + k^2$ and $B(r) = -\frac{3ik}{r} + \frac{3}{r^2} + k^2$[56, 133]. Most complex crystal structures encompass multiple fluorescent atomic sites with unique atomic surroundings in a unit cell. The experimentally measured hologram $\chi(\vec{k})$ from these structures then is a superposition of fluorescence patterns from different fluorescent atomic sites, and $\rho(\vec{r})$ in Equation 4.1 will be the averaged electron charge distribution with respect to all unique fluorescent atomic sites of the same chemical species. Hence, the term "electron density" refers to its averaged value when multiple fluorescent atomic sites are involved.

The hologram $\chi(\vec{k})$ is usually represented as $\chi(\theta_k, \varphi_k)$ for a fixed wave number k, where (θ_k, φ_k) is the direction of $\vec{k}$, as represented in a spherical coordinate system of measurement.

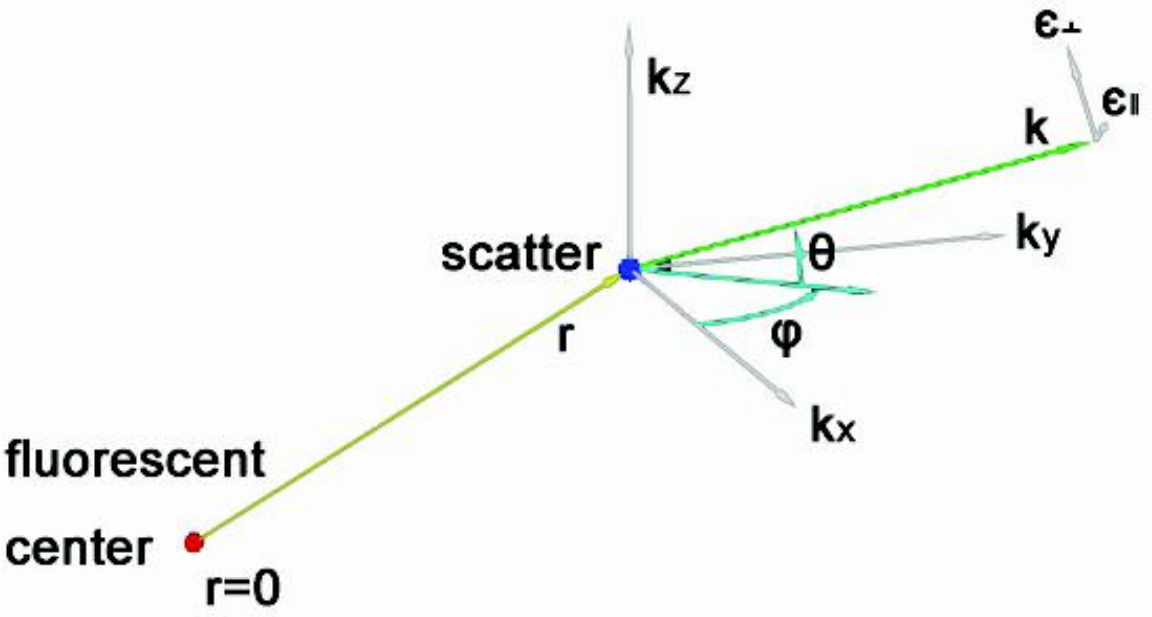

Figure 4.1 Definition of vectors and angles in spherical analysis.

Figure 4.1 illustrates the definition of vectors and angles in spherical analysis. In a transverse wave like X-ray, the polarization vector $\boldsymbol{\epsilon}$ is always in a plane perpendicular to the wave vector **k**. In direct scheme XFH, the unpolarized fluorescence wave is the probing wave and $\boldsymbol{\epsilon}$ in (4.1) is averaged in the plane. Equation 4.1 can be simplified as:

$$\chi(\vec{k}) = \iiint \rho(\vec{r}) \frac{r_e \mathrm{Exp}(ikr - i\vec{k}\cdot\vec{r})}{r} \left[A(r) + \frac{B(r)}{2}\left(1 - (\hat{k}\cdot\hat{r})^2\right)\right] d\vec{r} + \mathrm{C.C.} \qquad (4.2)$$

For the indirect scheme XFH, the probing wave is the polarized, elastically scattered X-ray wave. The indirect XFH can be depolarized by summing the holograms measured with two perpendicular polarization directions, $\boldsymbol{\epsilon}_\perp$ and $\boldsymbol{\epsilon}_\parallel$. With $(\boldsymbol{\epsilon}_\perp \cdot \hat{r})^2 + (\boldsymbol{\epsilon}_\parallel \cdot \hat{r})^2 + (\hat{k}\cdot\hat{r})^2 = 1$, the depolarized indirect XFH also can be represented by Equation 4.2. The following discussions apply to both direct XFH and depolarized indirect XFH, as described by Equation 4.2.

To extract the electron density from XFH, the hologram was expanded with spherical harmonics, and a relation between the spherical harmonic coefficients and the electron density function was derived.

Using the expansion for plane waves in terms of spherical wave:

$$\exp\left(-i\vec{k}\cdot\vec{r}\right) = \sum_{l=0}^{\infty}(-i)^{l}(2l+1)j_{l}(kr)P_{l}\left(\hat{k}\cdot\hat{r}\right) \tag{4.3}$$

where, j_l is the spherical Bessel function, and P_l, the Legendre function, the hologram χ can then be expanded to give:

$$\chi = r_e \sum_{l=0}^{\infty}\iiint \rho(\vec{r})\frac{e^{ikr}}{r}S_l(kr)P_l(\hat{k}\cdot\hat{r})d\vec{r} + C.C. \tag{4.4}$$

Here, $S_l(kr)$ is a spherical representation of the scattering factor between electrons and photons. Considering near field effects, $S_l(kr)$ is written as:

$$\begin{aligned} S_l(kr) = {} & (-i)^l(2l+1)j_l(kr)\left(\frac{-ik}{r}+\frac{1}{r^2}+k^2\right) \\ & + (-i)^l\frac{l(l-1)}{2l-1}j_{l-2}(kr)\left(\frac{-3ik}{r}+\frac{3}{r^2}-k^2\right) \\ & - (-i)^l\left[\frac{(l+1)^2}{2l+3}+\frac{l^2}{2l-1}\right]j_l(kr)\left(\frac{-3ik}{r}+\frac{3}{r^2}-k^2\right) \\ & + (-i)^l\frac{(l+1)(l+2)}{2l+3}j_{l+2}(kr)\left(\frac{-3ik}{r}+\frac{3}{r^2}-k^2\right) \end{aligned} \tag{4.5}$$

Also considering $P_l\left(\hat{k}\cdot\hat{r}\right) = \frac{4\pi}{2l+1}\sum_{m=-l}^{l}Y_{lm}(\theta_k,\varphi_k)Y_{lm}^{*}(\theta_r,\varphi_r)$, the spherical harmonic expansion of hologram is given by:

$$\chi = \sum_{l=0}^{\infty}\sum_{m=-l}^{l}Y_{lm}(\theta_k,\varphi_k)a_{lm} + C.C. \tag{4.6}$$

where, a_{lm} is calculated as:

$$a_{lm} = \frac{4\pi r_e}{2l+1} \iiint \rho(\vec{r}) \frac{e^{ikr}}{r} S_l(kr) Y_{lm}^*(\theta_r, \varphi_r)\, d\vec{r} \qquad (4.7)$$

The integral in Equation 4.7 extends over the entire volume of a single crystal. Electron density $\rho(\vec{r})$ in a crystal with finite size can be represented by a periodical electron density in infinite 3D space multiplied with an envelope size distribution function $\mu(r)$. By using the translation symmetry of the crystal, the electron density can be written as $\rho(\vec{r}) = \sum \rho(\vec{h}) \mathrm{Exp}(i\vec{h} \cdot \vec{r})\, \mu(r)$, where, $\rho(\vec{h})$ is related to the atomic structure factor $F(\vec{h})$ by $\rho(\vec{h}) = F(\vec{h})/V$ (V = unit cell volume), A simple form of $\mu(r)$ is a unit step function: $\mu = \eta(r - r_0)$, where r_0 is the average crystal size.

Then, Equation 4.7 can be rewritten as

$$a_{lm} = \frac{4\pi r_e}{2l+1} \sum_h \left[\iiint \mathrm{Exp}(i\vec{h} \cdot \vec{r}) \frac{e^{ikr}}{r} S_l(kr) Y_{lm}^*(\theta_r, \varphi_r) \mu(r) d\vec{r} \right] \rho(\vec{h}) \qquad (4.8)$$

Again, replacing the expression for the plane wave with the spherical wave expansion in (4.8):

$$\exp(-i\vec{h} \cdot \vec{r}) = \sum_{l=0}^{\infty} (-i)^l (2l+1) j_l(hr) P_l(\hat{h} \cdot \hat{r}) \qquad (4.9)$$

and considering $P_l(\hat{h} \cdot \hat{r}) = \frac{4\pi}{2l+1} \sum_{m=-l}^{l} Y_{lm}(\theta_r, \varphi_r) Y_{lm}^*(\theta_h, \varphi_h)$, Equation 4.8 can be rewritten as:

$$a_{lm} = \frac{(4\pi)^2 r_e}{2l+1} (i)^l \sum_{h,l,m} \left[\iiint \frac{e^{ikr}}{r} S_l(kr) j_l(hr) Y_{lm}^*(\theta_r, \varphi_r) Y_{lm}(\theta_r, \varphi_r) Y_{lm}^*(\theta_h, \varphi_h) \mu(r) d\vec{r} \right] \rho(\vec{h}) \qquad (4.10)$$

The integration in Equation 4.10 can be simplified using the orthogonal property of spherical harmonics on the surface of a sphere $\oiint Y_{lm}^{*}(\theta_r,\varphi_r)Y_{l'\ m'}\ (\theta_r,\varphi_r)d\Omega = \delta(l-l')\delta(m-m')$, so one have:

$$a_{lm} = \frac{(4\pi)^2 r_e}{2l+1}(i)^l \sum_h \left[Y_{lm}^{*}(\theta_h,\varphi_h)\int j_l(hr)e^{ikr}\mu(r)S_l(kr)rdr\right]\rho(\vec{h}) \qquad (4.11)$$

Now, consider the complex conjugate of (4.6), and add it to the expression of hologram as a real function:

$$\begin{aligned}\chi &= \sum_{l=0}^{\infty}\sum_{m=-l}^{l} Y_{lm}(\theta_k,\varphi_k)(a_{lm} + (-1)^m {a_{l-m}}^{*}) \\ &= \sum_{l=0}^{\infty}\sum_{m=-l}^{l} Y_{lm}(\theta_k,\varphi_k)c_{lm}\end{aligned} \qquad (4.12)$$

The $c_{lm}'s$ are the coefficients of spherical harmonics that can be calculated directly from the experimental hologram data. Since the hologram χ is a real function, there are only l+1 independent spherical harmonic coefficient for each l. The $c_{lm}'s$ provide a series of linear equations related to the structure factors:

$$\begin{aligned}c_{lm} = &\sum_h \left[\frac{8\pi^2 i^l r_e}{2l+1} Y_{lm}^{*}(\theta_h,\varphi_h)\int j_l(hr)e^{ikr}S_l(kr)\mu(r)rdr\right]\rho(\vec{h}) \\ &+ \sum_h \left[\frac{8\pi^2 i^l r_e}{2l+1} Y_{lm}^{*}(\theta_h,\varphi_h)\int j_l(hr)e^{-ikr}{S_l}^{*}(kr)\mu(r)rdr\right]\rho(\overrightarrow{-h})^{*}\end{aligned} \qquad (4.13)$$

Neglecting the anomalous scattering factors by assuming $\rho(\vec{h}) = \rho(\overrightarrow{-h})^{*}$ (or equivalently, assuming a real electron density function in Equation 4.7, the spherical harmonic expansion coefficient of the hologram can be given as:

$$c_{lm} = \sum_h \left[\frac{16\pi^2 i^l r_e}{2l+1} Y_{lm}^{*}(\theta_h,\varphi_h)\int j_l(hr)\mathrm{Re}\left(e^{ikr}S_l(kr)\right)\mu(r)rdr\right]\rho(\vec{h}) \qquad (4.14)$$

The structure factors $\rho(\vec{h})$ can be extracted from the coefficients of the spherical harmonics by solving linear Equations 4.13 or 4.14. To calculate the matrix elements, one need to know the values of h, θ_h , and φ_h. These are constants related to the lattice parameters, and can be obtained with routine X-ray diffraction measurements or Kossel line measurements on single crystals [134]. The crystal size is estimated from the line broadening of the X-ray diffraction to construct the size distribution function $\mu(r)$.

The integral function in Equation 4.14:

$$SJ_l(h,k) = \int j_l(hr)\mathrm{Re}\left(e^{ikr}S_l(kr)\right)\mu(r)rdr \qquad (4.15)$$

is a structure-independent function of h, with given wave vector k and the size distribution function $\mu(r)$. For odd l's and large even l's, $SJ_l(h,k)$ abruptly approaches zero at h = 2k. This is the consequence of the diffraction limit imposed by the equation: $\hat{k}\cdot\hat{h} = h/2k$.

Figure 4.2 shows an example of the numerical calculation of $SJ_l(h,k)$ for $l \in (0,50)$. Integration is performed with $\mu = \eta(r - 200\ \text{Å})$. For low even l's, the function extends beyond $h = 2k$, but quickly decays to negligible values. This is attributed to the tails of the Kossel lines with h-values nearest to 2k from above.

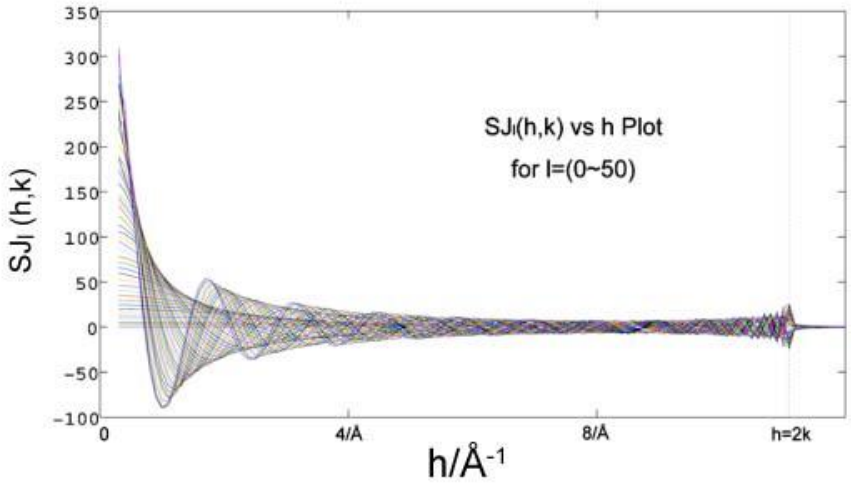

Figure 4.2 Matrix calculation as a function of h for k = 5.55 $Å^{-1}$.

Even though the diffraction limit reduces the number of structure factors that can be derived from the XFH data, it helps in defining a finite set of unknowns to be solved in the linear Equations 4.13- 4.14. All structure factors with h < 2k must be included to resolve the $\rho(\vec{h})$'s with high accuracy, while it is safe to ignore the structure factors with h > 2k using selected spherical harmonics.

The fine structure of the experimental XFH data depend on crystal size, the angular resolution of the X-ray beam, and other factors that cause the loss of high frequency signals in the hologram. For a structure to be reliably solved from the hologram, signals more susceptible to experimental condition must be separated from those strongly determined by the structure factors. The method of spherical harmonic expansion separates hologram signals according to their spatial frequency, thus allowing unreliable high frequency signals to be discarded. In practice, low and mid frequency signals are weakly influenced by the crystal size and the angular resolution of the X-ray beam.

4.3 Spherical Harmonic Analysis on Simulated Holograms from a Tetragonal CuAu Structure

Holograms from a tetragonal CuAu structure (Space group P4/mmm, a=2.800 Å, c= 3.670 Å) [135] is simulated with various crystal sizes and approximations using the following equation:

$$\chi\left(\vec{k}\right)=\sum_{i} A_{sf}(\vec{k},\vec{\mathrm{r}_{\mathrm{i}}})\frac{r_e Exp\left(ik\mathrm{r}_{\mathrm{i}}-i\vec{k}\cdot\vec{\mathrm{r}_{\mathrm{i}}}\right)}{\mathrm{r}_{\mathrm{i}}}\mu(\mathrm{r}_{\mathrm{i}})+C.C. \tag{4.16}$$

where, $A_{sf}(\vec{k},\vec{\mathrm{r}})$ is the generalized atomic scattering factor for XFH [51] which simulates effects including spherical wave scattering and polarization as well as the distribution of electron density in scattering atoms. The sum is over atoms in a sufficient large crystal lattice, where $\mu(\mathrm{r})$ is not negligible.

The holograms are simulated with a resolution of 0.25^{o} by 0.25^{o}, making 1440 points in φ direction and 721 points in θ direction. This resolution is selected to guarantee a reliable spherical harmonic expansion of the holograph up to $\mathrm{l}=99$, since it roughly gives 14 points of mesh grid in each oscillation period of $Y_{lm}(\theta_k,\varphi_k)$ with $l=99$. Using lower resolution in the holograph could cause increased noise during the spherical expansion.

The copper atom is taken as the fluorescent center in the inverse scheme XFH holograph simulation. Holograms are simulated with X-ray energy at 10.95 keV. This energy gives 1356 independent structure factors that satisfy the $h<2k$ condition, where $k=5.55\ \text{Å}^{-1}$ ($k=E*0.507keV^{-1}\ \text{Å}^{-1}$). There are a total of 1356 complex $\rho\left(\vec{h}\right)$ values to be solved from the spherical harmonic analysis. For this simple structure, there is only one fluorescence atom (Cu) in each unit cell; so the electron density derived from the XFH is the true electron density.

4740 c_{lm} spherical harmonic coefficients for $l \in (21,99)$ and $m \in (0,l)$ are extracted from the simulated holograph using the codes adapted from SPHEREPACK 3 [136]. Using Equation 4.14, the 1356 structure factor $\rho(\vec{h})$ are solved from the 4740 c_{lm} using MATLAB matrix division. For the overdetermined matrix equation, the solution is given by MATLAB in a least square sense with the QR iteration algorithm [137, 138]. This method decomposes a rectangular matrix into a product of an orthogonal matrix and an upper triangular matrix. An iteration algorithm based on the decomposed matrix is used to minimize the difference between the two sides of the matrix equation.

The matrix is chosen to be overdetermined to improve stability and accuracy when solving the matrix. Stability of the matrix equation can be measured by the condition number. For matrix equation $\boldsymbol{x} = A^{-1}\boldsymbol{b}$ **,** the condition number is defined as the maximum ratio of the change in solution to the change in input condition[139]:

$$\kappa(A) = \lim_{\epsilon \to 0} \left[\sup_{\|\delta \boldsymbol{b}\| \leq \epsilon} \frac{\|\boldsymbol{x}(\boldsymbol{b} + \delta \boldsymbol{b}) - \boldsymbol{x}(\boldsymbol{b})\| / \|\boldsymbol{x}(\boldsymbol{b})\|}{\|\delta \boldsymbol{b}\| / \|\boldsymbol{b}\|} \right] \tag{4.17}$$

where $\|.\|$ represents the norm of a vector. The condition number represents the upper limit of the matrix solution's sensitivity to error from the input matrix conditions. However, the maximum instability is only present at certain critical point of input condition $\boldsymbol{b}$=$\boldsymbol{b_c}$. In a practical matrix with 4740x678 elements, the chance of encountering the maximum instability is small. The error in matrix solution is expected to be much lower than the maximum error predicted by the condition number.

MATLAB also provides a 'cond' function for condition number calculation on overdetermined matrix equations. Condition number for rectangular matrix is calculated as $\kappa(A) = \|A\| \cdot \|A^{+}\|$, where A^{+} represents Moore-Penrose pseudo-inverse of the matrix A [138]. The condition number for the 4740x678 element matrix of CuAu model is 15.6.

This indicates an upper boundary of instability where the error in solution of the structure factors is 15.6 times larger than the error in measured spherical harmonic coefficients from the hologram.

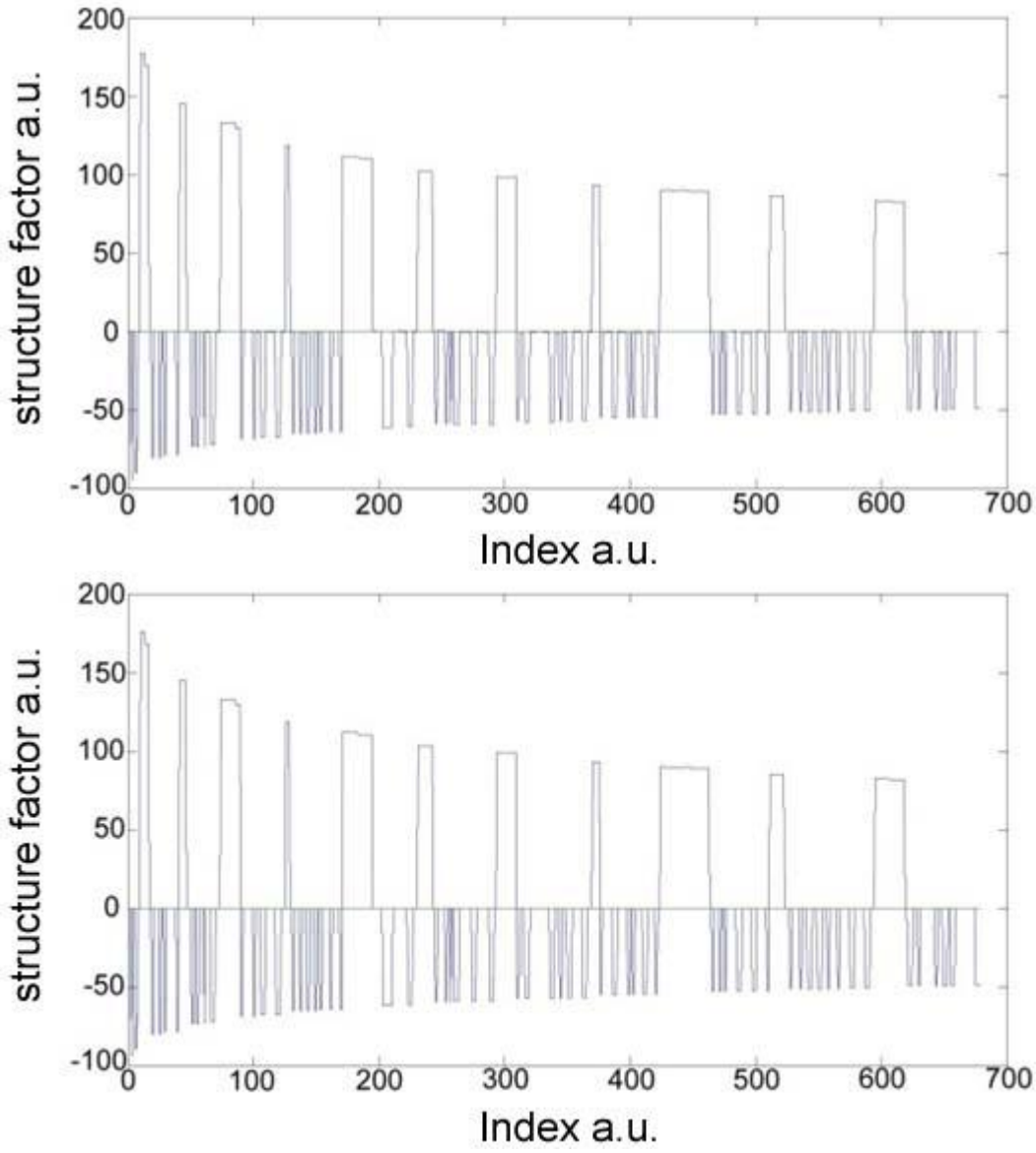

Figure 4.3 Solution structure factor (upper panel) of tetragonal CuAu single energy hologram with theoretical value (lower panel). Only half of the 1356 structure factors are displayed due to crystal symmetry.

The Matrix equation 4.14 does have some limitation. Low frequency $c_{lm}'s$ for $l < 21$ and high frequency $c_{lm}'s$ for $l > 99$ can cause inaccuracies. At $l < 21$, integration in Equation 4.12 converges relatively slower to zero when $h > 2k$. This in turn makes the matrix Equation 4.14 inaccurate. At $l > 99$, accurate spherical harmonic decomposition is limited by the hologram's resolution.

The above Figure 4.3 is $\rho(\vec{h})$ solved from the matrix equation, as compared with the theoretical value of $\rho(\vec{h})$ model. The holograph is simulated with cluster profile of $\mu = \exp(-(r/100\ \text{Å})^2)$. The matrix is calculated with the same profile. In Equation 4.15, a finite integration over r between 0.01 Å~190 Å is used to approximate the infinite integration. The RMS difference between this result and the theoretical value is 3.0% of the average $\rho(\vec{h})$.

Table 4.1 summarizes the solution achieved from the above spherical harmonic analysis condition as compared to theoretical values. A step function $\mu = \eta(r - r_0)$ is used to describe the cluster size in holograph simulation and matrix calculation. Four different cluster size of r_0 are simulated.

Table 4.1 Spherical Harmonic Analysis Results for Simulation with Different Cluster Size

(hkl)	*(100)*	*(001)*	*(110)*	*(111)*	*(135)*	*(352)*	*error*
Theoretical	(0,0)	(-93.9,0)	(-89.1,0)	(176.0,0)	(90.0,0)	(-52.1,0)	--
$r_0 = 19$ Å	(7.6,0)	(-86.1,0)	(-92.5,0)	(176.2,0)	(88.3,0)	(-53.4,0)	6.0%
$r_0 = 58$ Å	(0.2,0)	(-94.7,0)	(-89.9,0)	(177.1,0)	(92.9,0)	(-53.3,0)	3.2%
$r_0 = 190$ Å	(0.0,0)	(-95.0,0)	(-89.7,0)	(178.3,0)	(90.5,0)	(-54.2,0)	3.0%
$r_0 = 580$ Å	(-0.4,0)	(-94.2,0)	(-89.2,0)	(177.4,0)	(83.9,0)	(-49.9,0)	5.8%

The theoretical structure factor is calculated from the atomic scattering factor by $\rho(\vec{h}) = \sum A_{sf}(\vec{h}, \vec{r})e^{i\vec{h}\cdot\vec{r}}$ where summation is over the atoms in the unit cell.

4.3.1 Simulation of Large Cluster with 580 Å Radius

The result of the solved structure factors in Table 4.1, for a 580 Å sample cluster radius, is simulated in a way different from the other cluster size. The simulation on other cluster size is conducted using a hologram resolution of 1440x721. This resolution is sufficient when the signal is spatially smooth and the mesh grid of the holograph can accurately represent all details in hologram signal.

For the simulation of the 580 Å sample size, resonant Kossel line became very sharp. In this case, the 1440x721 holograph resolution cannot accurately represent all the signals in the holograph. A holograph simulation with 4320x2161 resolution was used to accurately simulate the hologram of 580 Å cluster size. To be consistent with resolution in other simulations, the simulated 4320x2161 resolution holograph is then averaged to become a 1440x721 resolution holograph. Each neighboring nine pixels in the high resolution holograph is averaged to become a single pixel in the lower resolution holograph. This averaging method simulates a real XFH experiment because the detector has a finite acceptance angle which averages all hologram signals in the solid angle into a single pixel.

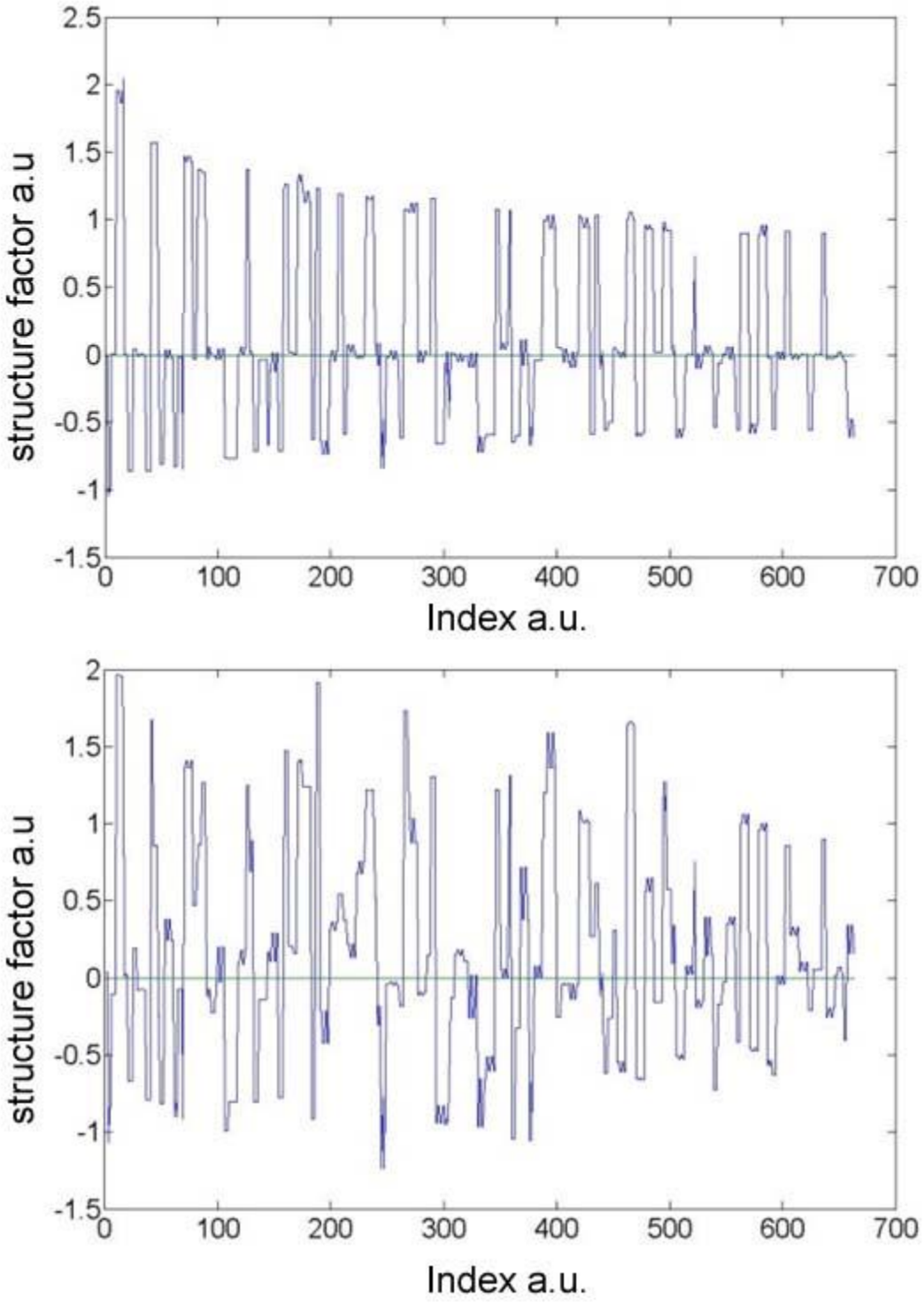

Figure 4.4 Solved structure factor from averaged hologram (upper panel) and not averaged low resolution hologram (lower panel).

If the averaging process is not used, the directly simulated low resolution holograph will contain too much noise and the structure factor would contain significant errors. Figure 4.4 is the result of structure factor solved from the simulated holograph with averaged hologram and not averaged low resolution holograph.

4.3.2 Effect of Inaccurate Cluster Size Profile $\mu(r)$

A cluster size profile factor μ(r) has to be estimated when calculating matrix elements in Equation 4.13-14. The factor μ(r) represents the statistical distribution of sample cluster sizes in the measured sample. In practice, inaccurately estimated μ(r) might be used to solve structure factor in spherical harmonic analysis. As shown in this Table 4.2, inaccuracy in estimated μ(r) has only a weak influence on reconstruction results. In this simulation, different cluster size profile functions μ(r) were used in the simulation of CuAu hologram and calculation of matrix elements in Equation 4.14. Anomalous scattering is neglected.

Table 4.2 Effect of Inaccurate Estimation of Cluster Profile μ(**h**) on the Solutions of Matrix (part 1)

(hkl)	*(100)*	*(001)*	*(110)*	*(111)*	*(135)*	*(352)*	*error*
Theoretical	(0,0)	(-93.9,0)	(-89.1,0)	(176.0,0)	(90.0,0)	(-52.1,0)	--
$c_{\mu 1}/M_{\mu 1}$	(-0.4,0)	(-94.7,0)	(-90.6,0)	(177.6,0)	(92.7,0)	(-54.0,0)	2.1%
$c_{\mu 2}/M_{\mu 2}$	(0.1,0)	(-94.9,0)	(-90.0,0)	(178.0,0)	(88.1,0)	(-52.4,0)	2.0%
$c_{\mu 3}/M_{\mu 3}$	(-0.2,0)	(-94.8,0)	(-90.5,0)	(177.4,0)	(92.5,0)	(-53.0,0)	2.4%
$c_{\mu 2}/M_{\mu 1}$	(-0.4,0)	(-94.7,0)	(-90.7,0)	(177.5,0)	(91.8,0)	(-52.4,0)	2.2%
$c_{\mu 1}/M_{\mu 2}$	(-0.7,0)	(-94.9,0)	(-89.9,0)	(178.2,0)	(89.6,0)	(-54.1,0)	2.4%
$c_{\mu 1}/M_{\mu 3}$	(-1.0,0)	(-95.1,0)	(-89.8,0)	(177.8,0)	(93.6,0)	(-55.5,0)	5.0%
$c_{\mu 3}/M_{\mu 1}$	(0.3,0)	(-94.2,0)	(-91.1,0)	(177.0,0)	(91.4,0)	(-51.6,0)	5.1%

For a simulation of relatively small inaccuracy in cluster profile, cluster size profiles $\mu1 = \eta(r - 150\ \text{Å})$, $\mu2 = \text{erfc}(r/20 - 7.5)$ and $\mu3 = \eta(r - 100\ \text{Å})$ were used. Three holograms and matrices are simulated from these cluster size profiles. The matrix solution results are compared in Table 4.2. Errors induced by the difference in these cluster size profiles are less than 5.1%.

Larger inaccuracy is also simulated using $\mu1 = \text{erfc}(r/20 - 7.5)$ for hologram simulation, and a significantly different unit step function $\mu2 = \eta(r - 190\ \text{Å})$ to calculate matrix elements. The matrix solution results are compared in Table 4.3. $c_{lm}/M(\mu1)$ represents a hologram solved with accurate cluster size profile in matrix calculation. $c_{lm}/M(\mu2)$ represents hologram solved with inaccurate cluster size profile in matrix calculation.

Table 4.3 Effect of Inaccurate Estimation of Cluster Profile μ on the Solutions of Matrix (part 2)

(hkl)	*(100)*	*(001)*	*(110)*	*(111)*	*(135)*	*(352)*
Theoretical	(0,0)	(-93.9,0)	(-89.1,0)	(176.0,0)	(90.0,0)	(-52.1,0)
$c_{lm}/M(\mu1)$	(-0.2,0)	(-94.2,0)	(-89.9,0)	(177.5,0)	(89.4,0)	(-52.3,0)
$c_{lm}/M(\mu2)$	(-0.5,0)	(-85.3,0)	(-83.1,0)	(167.1,0)	(89.4,0)	(-49.5,0)
$Error(\mu1)$	--	0.3%	0.9%	0.9%	0.7%	0.4%
$Error(\mu2)$	--	9.5%	6.7%	5.0%	0.7%	3.1%

From Table 4.3, a very inaccurate estimation of μ results in some error in the solved structure factor; however, the matrix Equation 4.11 is stable.

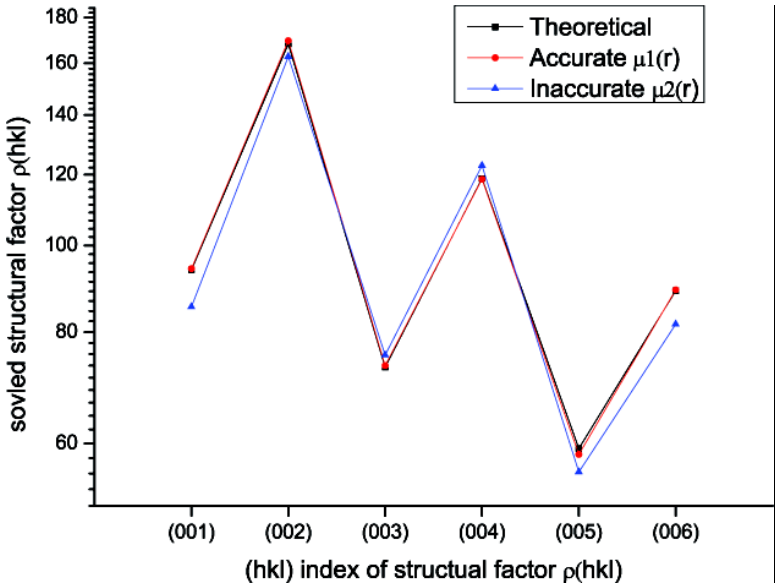

Figure 4.5 Solved structure factor of tetragonal CuAu single energy holograph.

The additional data in Table 4.3 are plotted as a function of the (hkl) index of the structure factor, as shown in the above Figure 4.5. Accurate estimation of $\mu(r)$ in Equation 4.14 gives solution $c_{lm}/M(\mu 1)$, which is undistinguishable from theoretical value in Figure 4.5. Inaccurate estimation results in reasonable level of error.

Figure 4.6 is a plot of the reconstructed real space electron density (along the 011 direction in unit cell) from solved structure factors. The results from $c_{lm}/M(\mu 1)$ and $c_{lm}/M(\mu 2)$ are overlapped. No shift in atom position is observed. The resulting peak intensity for Au atom from $c_{lm}/M(\mu 2)$ has 1.7% error. The error in results from $c_{lm}/M(\mu 1)$ is less than 0.1%.

Although $c_{lm}/M(\mu 2)$ gives as much as 9.5% error in structure factors for the (001) index, real space electron density $\rho(\vec{r})$ is calculated from all structure factors within condition of $h < 2k$. In this case of simulation, for 1356 structure factors, all contribute

to reconstruction of $\rho(\vec{r})$. Error in individual $\rho(\vec{h})$ are statistically averaged and results in good electron density $\rho(\vec{r})$ even using poor estimations of $\mu(r)$.

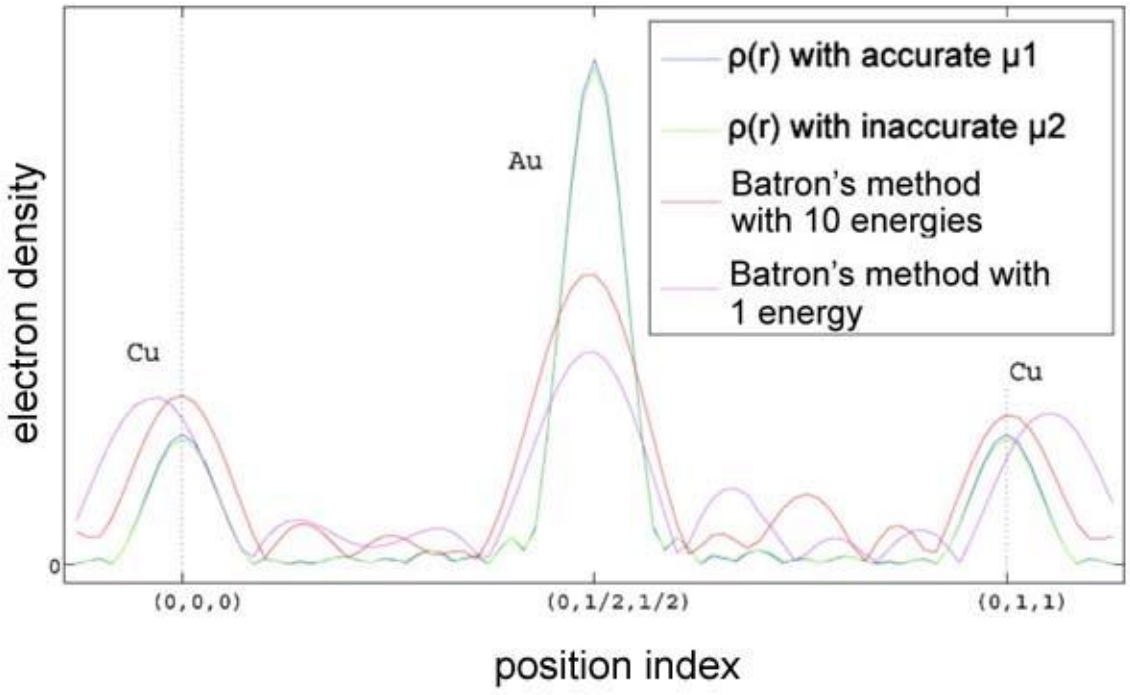

Figure 4.6 Real space electron density (in arbitrary unit) of CuAu simulated model on (011) unit cell direction.

Reconstruction results from Barton's method are also simulated and compared in Figure 4.6. MXFH simulation were performed on ten X-ray energies equally space between 10.97 keV and 11.83 keV and reconstructed using standard MXFH (multiple energy) algorithm [39]. Single energy XFH simulation is reconstructed with standard single energy XFH algorithm [38] at 10.97 keV. Note the significant shifts in the atomic positions obtained by use of the Barton 2D Fourier Transform approach makes use of XFH as a qualitative tool difficult.

Specifically, the cluster size profile, $\mu(r)$, has only a small influence on reconstructed real space electron density. The reconstructed image suffers from much

lower background ripple as compared to Barton's method. The shift in Cu peak position is measured to be zero compared to 2.8% in the lattice constant peak position shift in the reconstruction from single energy Barton's method.

4.3.3 Effect of Near Field Spherical Wave Front Scattering

Since X-ray holograph is a scattering process between spherical waves and electrons, the effect of the near field spherical wave front will make the scattering behave slightly different from scattering described with plane wave equations [51, 133]. This difference is a second order effect and can be observed in simulations. The $\frac{k}{r}$ term and $\frac{1}{r^2}$ term in $A(r)$ and $B(r)$ in Equation 4.5 are used to simulate this near field effect. When this effect is neglected, it causes a discernable error when reconstructing small clusters. In the following result, holograms are simulated assuming spherical cluster of 19 Å radius, i.e., $\mu = \eta(r - 19\,\text{Å})$, and with near field effect considered. Anomalous scattering is neglected.

M_{Near}^{hkl} is the matrix in Equation 4.14 calculated with consideration of near field effects. M_{Far}^{hkl} is the matrix calculated neglecting near field effects. Results in Table 4.4 show theoretical structure factor values for selected (hkl) indices; solutions that neglect near field effects in matrix calculation as in c_{lm}/M_{Far}^{hkl}, and solutions that do not neglect near field effects as in c_{lm}/M_{Near}^{hkl}. The method takes full consideration of near field effects and theoretically gives smaller errors when compared to theoretical values. However, the influence is small. When simulating larger clusters as shown in Table 4.4, the effect of the near field correction is negligible.

Table 4.4 Effect of Near Field Spherical Wave Front on Matrix Solving

(hkl)	*(100)*	*(001)*	*(110)*	*(111)*	*(135)*	*(352)*
Theoretical	(0,0)	(-93.9,0)	(-89.1,0)	(176.0,0)	(90.0,0)	(-52.1,0)
$c_{lm}/\mathrm{M}_{\mathrm{Far}}^{\mathrm{hkl}}$	(7.9,0)	(-86.3,0)	(-95.6,0)	(171.4,0)	(81.0,0)	(-60.0,0)
$c_{lm}/\mathrm{M}_{\mathrm{Near}}^{\mathrm{hkl}}$	(6.6,0)	(-87.5,0)	(-95.3,0)	(172.4,0)	(81.0,0)	(-59.3,0)
$\mathrm{Error}_{Far}^{Near}$	--	8.1%	7.3%	2.6%	10.0%	15.2%
$\mathrm{Error}_{Near}^{Near}$	--	6.8%	7.0%	2.0%	10.0%	13.8%

4.3.4 Considering Anomalous Scattering

A real atom has a complex atomic scattering factor when the X-ray energy is close to an absorption edge of the scattering element. Electron density could show an imaginary part in this condition. Holograms simulated with consideration of anomalous scattering need to be solved with Equation 4.13 rather than Equation 4.14. In the following result, complex atomic scattering factors are used in hologram simulation to study the effect of anomalous scattering. An error function $\mu(\mathrm{r}) = \mathrm{erfc}(\mathrm{r}/50 - 3)$ cluster size profile is assumed in holograph simulation and used to calculate the matrix elements. Solution of $\rho(\vec{\mathrm{h}})$ from Equation 4.13 is compared with solution from Equation 4.14 in Table 4.5.

Table 4.5 Solved Structure factor with Consideration of Anomalous Scattering

(hkl)	*(100)*	*(001)*	*(110)*	*(111)*	*(135)*	*(352)*
Theor(4.13)	(0,0)	(-79.1,3.3)	(-74.3,-3.3)	(158.7,14.5)	(72.6,14.5)	(-37.3,-3.3)
$c_{lm}/\mathrm{M}(4.13)$	(0.1,0.0)	(-79.5,-2.8)	(-75.1,-3.0)	(159.5,14.2)	(72.6,14.7)	(-37.5,-3.3)
Theor(4.14)	(0,0)	(-93.9,0)	(-89.1,0)	(176.0,0)	(90.0,0)	(-52.1,0)
$c_{lm}/\mathrm{M}(4.14)$	(0.0,0)	(-97.2,0)	(-88.4,0)	(179.2,0)	(99.5,0)	(-53.0,0)
Error(4.13)	--	0.8%	1.1%	0.5%	0.3%	0.5%
Error(4.14)	--	3.5%	0.8%	1.8%	10.5%	1.7%

In Table 4.5, the ‘Theor(4.13)’ parameter is theoretical structure factor considering anomalous scattering effect and calculated from complex atomic scattering factors. $Theoretical_{14}$ is theoretical structure factor neglecting anomalous scattering effect and calculated from real atomic scattering factors. Although the holograms are simulated from complex atomic scattering factors, the result is close to the ‘Theor(4.14)’ parameter where matrix is solved with a simplifying assumption that neglects anomalous scattering.

4.4 Spherical Harmonic Analysis on Simulated $HoMnO_3$ Hologram

To demonstrate the structure-resolving power of the spherical harmonic analysis method on XFH data, the method is applied to a hexagonal $HoMnO_3$ structure (space group P63cm, a = 6.1413 Å, c = 11.4122 Å) [135]. $HoMnO_3$ is an important multi-ferroic structure [140]. This system is chosen as an example because this non-centrosymmetric system has a complex structure factor and the presence of the heavy holmium atoms in the unit cell. It is difficult to accurately determine the oxygen positions using regular XRD methods. Calculating the spontaneous polarization of the system based on its structure requires accurate determination of the positions of the oxygen in the unit cell. The manganese in the structure is the fluorescence emitter with 8 keV X-rays used as the probing wave.

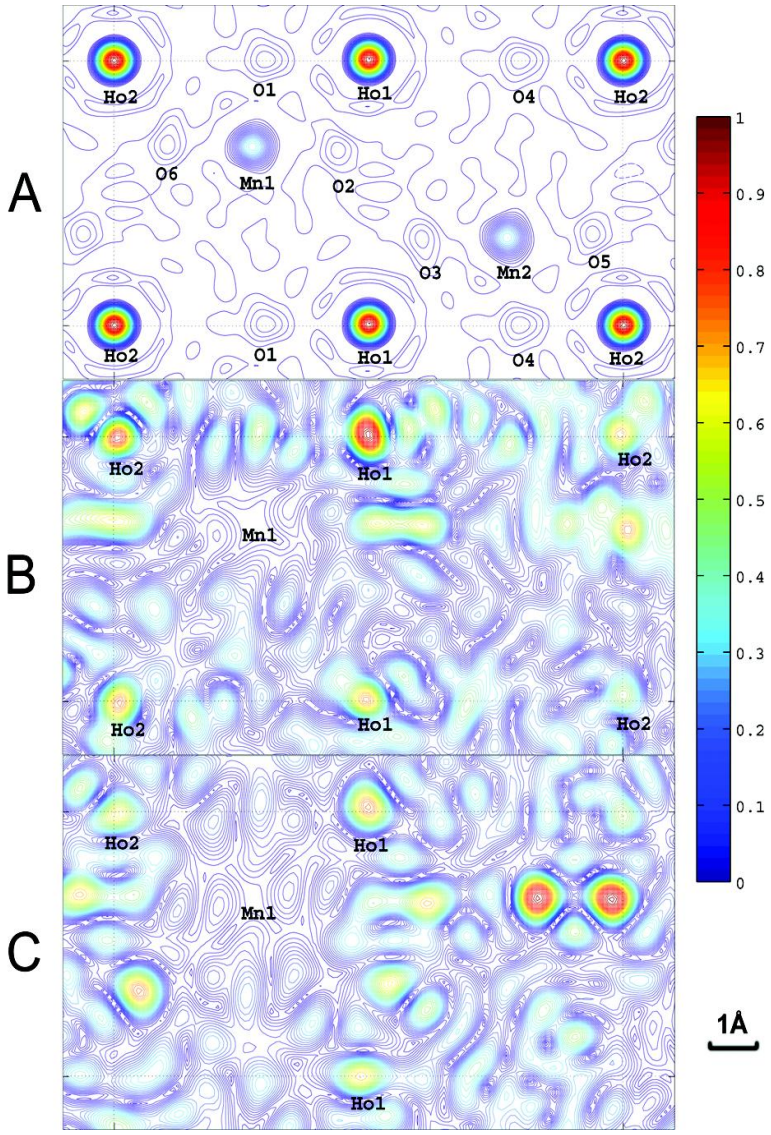

Figure 4.7 (A) Reconstructed electron density in (100) plane from the solved structure factors of $HoMnO_3$, (B) structure image from Barton's method with five energies, (C) from Barton's method with one energy.

The hologram is simulated with the same algorithm for the CuAu holograph. Only one of the six Mn atoms is assigned in the HoMnO3 unit cell as the fluorescence emitter in the simulation so that one could compare the reconstructed electron density map directly to that of the model structure. With an X-ray energy of 8.0 keV, there are 3334 structure factors satisfying $h < 2k$. The hologram was simulated with 0.5°

resolution in both θ_k and φ_k, resulting in 361x720 data points. FORTRAN codes adapted from SPHEREPACK 3.0 were employed to calculate the coefficients c_{lm} of spherical harmonic expansion from these data points. A complementary error function $\mu = \mathrm{erfc}\left[(r - 150\ \text{Å})/50\ \text{Å}\right]$ was used to define the crystalline size in the hologram simulation and in the matrix calculation. The c_{lm}'s with $l \in (21,99)$ and $m \in (0, l)$ were used to construct 4740 complex linear Equations (4.14). The matrix division function of MATLAB was used to solve this over-determined linear system. The condition number of the matrix is 434.5. This indicates the matrix is sufficiently good for both simulation and experiment. This condition number can be further improved by selecting more spherical harmonic coefficients to make the matrix equation further overdetermined.

The 3344 structure factors had a standard deviation of approximately 1.8% with respect to the model values. An electron density map in the (100) plane of HoMnO3 with these structure factors (Figure 4.7A) is then constructed. In Figure 4.7B and 4.7C, real space images obtained using the Barton transform is also depicted, from the five holograms acquired with equally spaced energies from 8.0 keV to 9.6 keV (Figure 4.7B), and a single energy hologram at 8.0 keV (Figure 4.7C), on the same contrast scale. Comparing them clearly reveals that the new method greatly improved the structure-resolving capability of the XFH method. It also demonstrates that the essential structural information is already contained in a single energy hologram. The electron density map displays precise atomic positions and proper intensity ratios between the Ho, Mn, and O atoms, thus providing adequate information to resolve the structure without an a priori knowledge of the atomic constituents of the unit cell. Importantly, the position and shape of oxygen atoms are shown clearly, despite the presence of the heavy holmium atoms in

the unit cell. Hence, XFH, undoubtedly, is an effective tool to probe systems with high variations in electron density. Further, the spherical harmonic analysis on XFH data affords us a novel method to study the non-spherical distribution of density without resorting to model building or phase refinement.

The distance between image atoms can be measured by peak to peak distance in Figure 4.7. Table 4.6 compares the listed distance for atoms in reconstructed image to theoretical value. Note that the measured distance is the distance between the maximum at the electron density positions of the atom images. It is not the center of the image atoms.

Table 4.6 Comparison of the Bound Distance in Solved Structure to Theoretical Values

Bound Δr	*Ho1/Ho2*	*Mn1/Ho1*	*Mn2/O3*	*O1/O6*
Theoretical	5.7061 Å	3.5959 Å	1.8838 Å	3.9614 Å
Simulation	5.7061 Å	3.5498 Å	2.0482 Å	4.1505 Å
Error	0.0000 Å	0.0461 Å	0.1644 Å	0.1889 Å

The strongest peaks for Ho atoms give accurate results. The atomic distances between weaker atoms suffer larger error due to the fact that weaker peaks are influenced by background noise and ripples form stronger peaks. For better accuracy in measuring distance between atomic positions, three dimensional non-linear fitting with a well-designed fitting model that correctly represent shape, ripple and tail of atomic peaks can be developed to fit the center position of each atomic image.

The result indicates that spherical harmonic analysis is capable of extracting quantitive structural information with good accuracy.

The ambiguity caused by the multiple fluorescence centers is an intrinsic limit of the XFH method and can be resolved by making use of space group symmetry and bond

length constraints. Spherical harmonic analysis, as well as Barton's method, requires a hologram data set in full 4π solid angle. Currently, most XFH measurements are taken from a flat surface of large single crystals, and hence, it is difficult to directly measure the hologram in a full 4π solid angle in this geometry. Therefore, the point group symmetry of the crystal is employed to extend the data set to its full range. With advancements in synchrotron radiation technologies, XFH can be measured from small crystals in the transmission mode using a highly focused beam. XFH in transmission mode will make it possible to directly measure the full range hologram, to measure the holograms in two polarization geometries with same diffractometer setup (to depolarize the direct XFH data), and to extend the application of XFH to other fields of crystallography, such as structural biology.

4.5 Reconstruction of Experimental PZN-PT Hologram

A single energy indirect scheme PZN-PT XFH hologram was measured at NSLS at beamline X14A (Figure 3.8D). The energy of the incident X-ray beam is 14.5 keV.

The hologram is measured between 0^o and 70^o theta angles and expanded to 4π solid angle with symmetry. Cubic symmetry is assumed in the expansion.

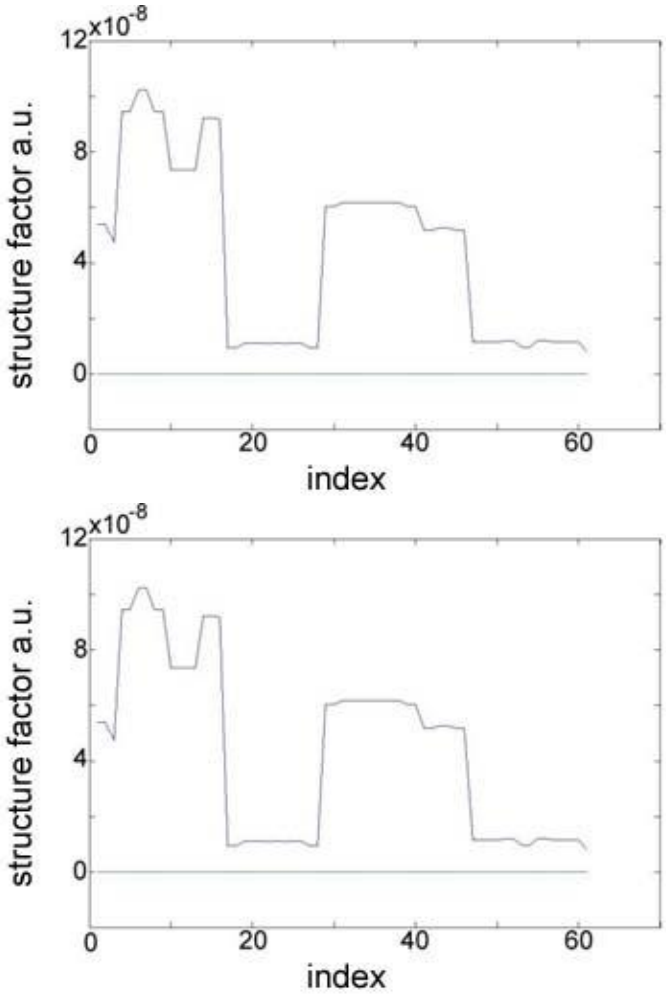

Figure 4.8 Solved ρ(h) (upper panel) for experimental holograph as compared to theoretical ρ(h) (lower panel).

Even with the low quality and resolution of the experimental hologram, spherical harmonic expansion of the holograph can be accurately performed to the maximum resolution at l = 40. This resolution is not sufficient to solve all structure factors in Equation 4.14. In order to get stable solution, all structure factors with $h > 3.77$ are assumed negligible. This assumption is not accurate but is necessary to acquire stable solution from Equation 4.14. $\rho(\vec{h})$ is solved for all $h < 3.77$ structure factors; this gives

63 structure factors solved as shown in Figure 4.8. The result is noisy. Only rough features in $\rho(\vec{h})$ can be distinguished.

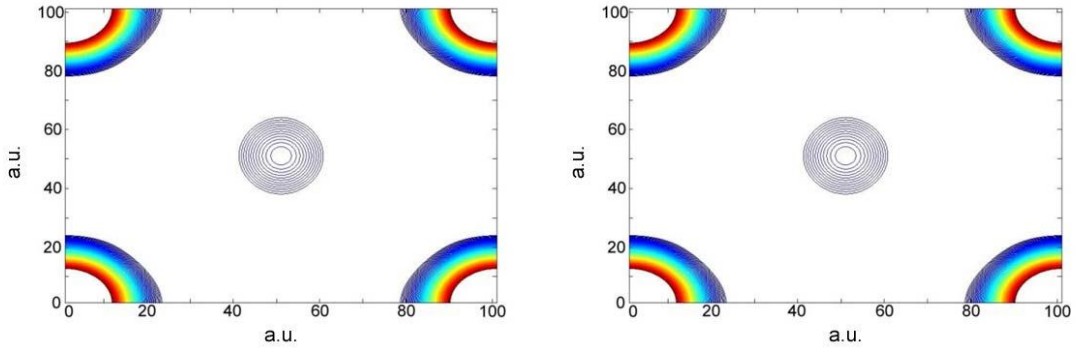

Figure 4.9 Reconstructed electron density on (100) (left) and (110) (right) plane of PZN-PT unit cell from solved ρ(h) picture.

Figure 4.9 is the reconstructed electron density $\rho(\vec{r})$ from the solved structure factor $\rho(\vec{h})$ in Figure 4.8.

The atom at corners are Pb and the atom at center for (110) plane is 2/3 Zr mixed with 1/3 Nb. The atoms at center of (100) plane and at center edges of (110) plane are oxygen. The intensity of the oxygen atom is stronger than estimated. This could be due to errors that are caused by truncating the matrix Equation 4.14 by assuming all structure factor with $h > 3.77$ are negligible.

4.6 Conclusions

The new reconstruction algorithm based on spherical harmonic analysis provides an efficient method that is readily automated to directly extract structure information from single energy X-ray fluorescence holograms. This new method makes XFH a quantitative method that is highly applicable to materials characterization.

CHAPTER 5

OTHER TECHNIQUES AND CONSIDERATIONS

5.1 Introduction

X-Ray Holography is a promising technique which yields the three dimensional structure of materials. With the advent of high flux sources and fast X-ray detectors, this method is under serious consideration as a mainstream measurement technique [68, 78-80]. The method is still in rapid development and has not achieved a routine utility. One of the major problems in the traditional reconstruction technique (Barton's method) is the difficulty to achieve high signal to noise ratio, especially for atoms far away from the central atom. A relatively comprehensive analysis on the source and nature of the errors in X-ray holograms and reconstructed images is thus worth the effort.

5.2 Study of Forward Scattering Suppression

The normalized hologram function, as defined in Barton's paper [23], can be written as [51]:

$$\chi(\boldsymbol{k}) = r_e \sum_i \frac{A_{sf}(\boldsymbol{k}, \boldsymbol{r_i})}{r_i} Exp(ikr_i - i\boldsymbol{k} \cdot \boldsymbol{r_i}) + C.C. \qquad (5.1)$$

where, r_e is the classical electron radius and $\boldsymbol{r_i}$ is the center of the i^{th} scattering atom and c.c. represent complex conjugation, $A_{sf}(\boldsymbol{k}, \boldsymbol{r_i})$ is a generalized atomic scattering factor for the i^{th} scattering atom.

The reconstructed image of a single energy hologram, which is the Fourier transformation of the normalized hologram function, has the form:

$$U(\boldsymbol{r}) = \iint_S \chi(\boldsymbol{k})\, Exp(i\boldsymbol{k}\cdot\boldsymbol{r}) d\Omega_k \tag{5.2}$$

Where, $U(\boldsymbol{r})$ is the reconstructed real space image, and the integration is over 4π solid angle.

5.2.1 Effect of Atomic Scattering Factor

Plugging the normalized holograph function $\chi(k)$ into the reconstruct image Equation 5.2, one has:

$$\begin{aligned} U(\boldsymbol{r}) &= \iint_S \chi(\boldsymbol{k})\, Exp(i\boldsymbol{k}\cdot\boldsymbol{r})\Omega_k \\ &= r_e \sum_i \left\{ \frac{e^{-ikr_i}}{r_i} \int_0^{2\pi} \int_{-\pi/2}^{\pi/2} A_{sf}(\boldsymbol{k}, \boldsymbol{r_i})\, e^{i\boldsymbol{k}\cdot(\boldsymbol{r}+\boldsymbol{r_i})} \cos(\theta) d\theta d\varphi \right\} \\ & r_e \sum_i \left\{ \frac{e^{ikr_i}}{r_i} \int_0^{2\pi} \int_{-\pi/2}^{\pi/2} A_{sf}(\boldsymbol{k}, \boldsymbol{r_i})\, e^{i\boldsymbol{k}\cdot(\boldsymbol{r}-\boldsymbol{r_i})} \cos(\theta) d\theta d\varphi \right\} \end{aligned} \tag{5.3}$$

Since the integration is over the full 4π solid angle, one can choose (θ, φ) so that $\theta = \pi/2$ is oriented at the direction of $(\mathbf{r} - \mathbf{r_i})$ for the first term in Equation 5.3 and in the direction of $(\mathbf{r} + \mathbf{r_i})$ for the second term in Equation 5.3. Hence the first and second terms are treated separately and use different coordinate systems. Figure 5.1 is a graph for the coordinate systems used here.

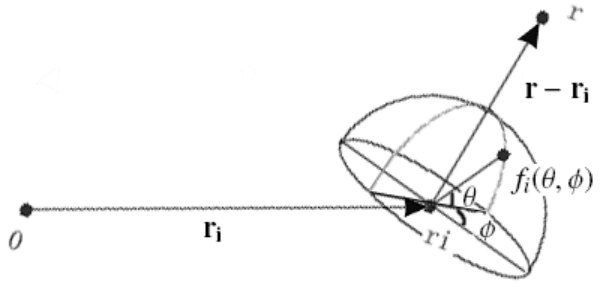

Figure 5.1 Coordinates used in the discussion.

Using coordinates shown as Figure 5.1, Equation 5.3 can be rewritten as:

$$U(\boldsymbol{r}) = r_e \sum_i \left\{ \frac{e^{-ikr_i}}{r_i} \int_{-\pi/2}^{\pi/2} \left[\int_0^{2\pi} A_{sf}(\boldsymbol{k}, \boldsymbol{r_i})\, d\varphi \right] e^{i\boldsymbol{k}\cdot(\boldsymbol{r}+\boldsymbol{r_i})} dsin\theta \right\} \\ r_e \sum_i \left\{ \frac{e^{ikr_i}}{r_i} \int_{-\pi/2}^{\pi/2} \left[\int_0^{2\pi} A_{sf}(\boldsymbol{k}, \boldsymbol{r_i})\, d\varphi \right] e^{i\boldsymbol{k}\cdot(\boldsymbol{r}-\boldsymbol{r_i})} dsin\theta \right\} \tag{5.4}$$

One can define the integration of atomic scattering factor over φ as IASF and the Fourier transform of IASF as $\mathcal{F}$IASF:

$$IASF(\theta) = \left[\int_0^{2\pi} A_{sf}(\boldsymbol{k}, \boldsymbol{r_i})\, d\varphi \right] \tag{5.5}$$

$$\begin{aligned} \mathcal{F}IASF(k|\boldsymbol{r} - \boldsymbol{r_i}|) &= \int_{-\pi/2}^{\pi/2} \left[\int_0^{2\pi} A_{sf}(\boldsymbol{k}, \boldsymbol{r_i})\, d\varphi \right] e^{i\boldsymbol{k}\cdot(\boldsymbol{r}-\boldsymbol{r_i})} dsin\theta \\ &= \int_{-\pi/2}^{\pi/2} IASF(\theta) e^{ik(r-r_i)sin\theta} dsin\theta \end{aligned} \tag{5.6}$$

Thus, the reconstructed image in Equation 5.2 can is given by:

$$U(r) = r_e \sum_i \left[\frac{e^{ikr_i}}{r_i} \mathcal{F}IASF(k|\boldsymbol{r} - \boldsymbol{r_i}|) + \frac{e^{-ikr_i}}{r_i} \mathcal{F}IASF(k|\boldsymbol{r} + \boldsymbol{r_i}|) \right] \tag{5.7}$$

Equation 5.7 indicates that the image of a single atom scatter in the reconstructed image is proportional to the $\mathcal{F}IASF$ function, which in turn is solely determined by Fourier transformation between $\theta \in (-\pi/2, \pi/2)$ of the atomic scattering factor. The more high frequency component exists in the atomic scattering factor, the more ripples in the reconstructed real space image.

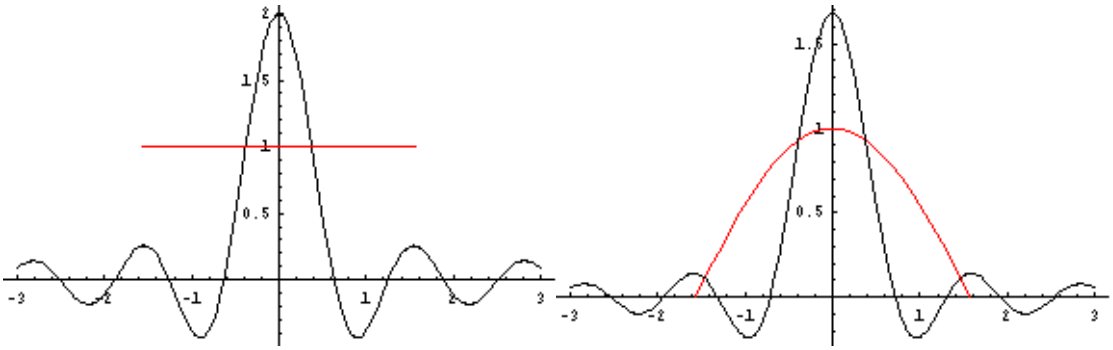

Figure 5.2 Atomic scattering factor A_{sf} versus scattering angle θ plot (red) and $\mathcal{F}IASF$ function versus $k|\boldsymbol{r}-\boldsymbol{r_i}|$ plot (black) for example atomic scattering factors $f_i(\theta,\varphi)$ where $f_i(\theta,\varphi)=1$ (left) and $f_i(\theta,\varphi)=\cos(\theta)$ (right).

Figure 5.2 is an example of the reconstructed image for atomic scattering factor for $f_i(\theta,\varphi)=1$ and $f_i(\theta,\varphi)=cos(\theta)$. Since integration is limited to $\theta\in(-\pi/2,\pi/2)$, the abrupt cut off of the $f_i(\theta,\varphi)=1$ atomic scattering factor gives more high frequency component, and thus has more ripples in the reconstructed image.

5.2.2 Suppressing Forward Scattering

Atomic scattering factor of real atoms could have strong high frequency components (anisotropic scattering component) for high energy X-rays, as shown in Figure 5.3. This is also referred as forward scattering [33]. The Fourier transform of a strongly anisotropic forward scattering atomic scattering factor causes large ripples in the reconstructed real space image.

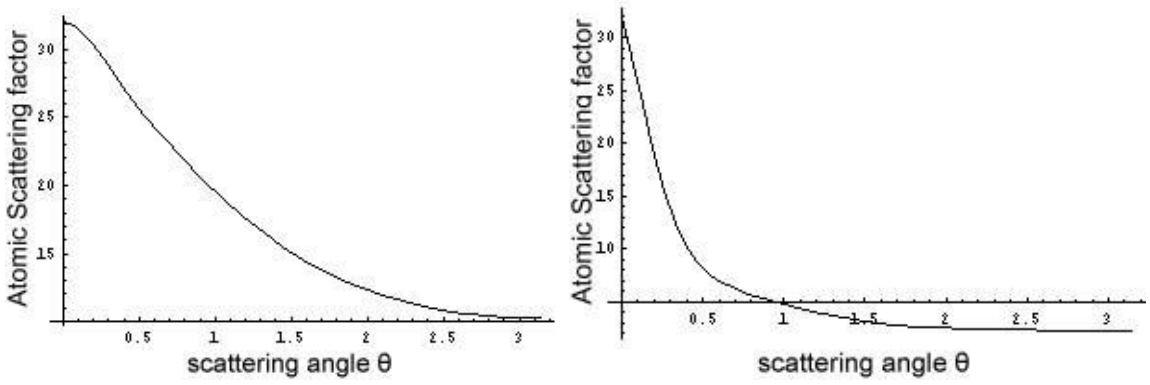

Figure 5.3 Atomic scattering factor f_i versus scattering angle θ plot for Fe atom for 5 keV energy (left) and 25 keV (right) X-ray energy.

The effect of anisotropic scattering caused ripple noise can be alleviated by multiplying the holograph by a profile function of $\alpha(\theta)$ to reduce ripple in the reconstructed real space image. The reconstruction equation is shown in Equation 5.8.

$$U(\boldsymbol{r}) = r_e \sum_i \left\{ \frac{e^{-ikr_i}}{r_i} \int_{-\pi/2}^{\pi/2} \left[\int_0^{2\pi} A_{sf}(\boldsymbol{k}, \boldsymbol{r_i})\, d\varphi \right] e^{i\boldsymbol{k}\cdot(\boldsymbol{r}+\boldsymbol{r_i})} \alpha(\theta) dsin\theta \right\} \\ r_e \sum_i \left\{ \frac{e^{ikr_i}}{r_i} \int_{-\pi/2}^{\pi/2} \left[\int_0^{2\pi} A_{sf}(\boldsymbol{k}, \boldsymbol{r_i})\, d\varphi \right] e^{i\boldsymbol{k}\cdot(\boldsymbol{r}-\boldsymbol{r_i})} \alpha(\theta) dsin\theta \right\} \tag{5.8}$$

The $\alpha(\theta)$ factor in Equation 5.8 can be chosen to reduce the weight of sharp forward scattering in Figure 5.3 and thus reduce ripples in the reconstructed image.

A 5x5x5 atom Fe lattice is used to simulate a XFH hologram at 25 keV X-ray energy with Equation 5.1. The hologram a reconstructed with both Equation 5.2 and Equation 5.8 with $\alpha(\theta) = cos^2\theta$. Results are shown in Figure 5.4.

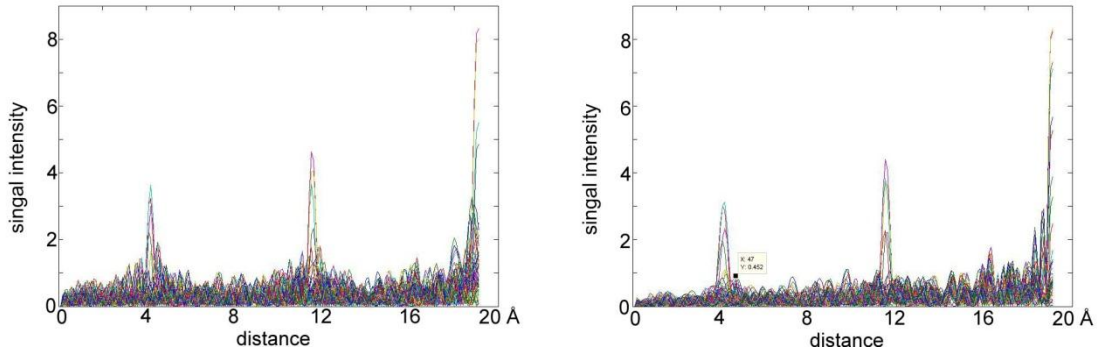

Figure 5.4 Reconstructed real space image for 5x5x5 unit cell Fe lattice without forward scattering suppression (left) and with $\alpha(\theta) = cos^2\theta$ as forward scattering suppression factor (right).

Results in Figure 5.4 show a reduction in ripple noise in the result of reconstruction using forward scattering suppression.

5.2.3 Conclusions

Using forward scattering suppression in XFH holograph reconstruction can reduce the amount of ripple noise. The extent to which noise is reduced depends on a careful choice of the suppression function $\alpha(\theta)$. Since the ripple noise will add to atomic image peaks in the reconstructed image, accurate extraction of atomic positions from the reconstruction image is difficult. With reduced ripple noise in background of reconstructed image, the position of atomic image peak can be extracted with better accuracy.

5.3 Statistical Considerations of Signal Intensity in XFH Measurements

The signal intensity of a XFH hologram can be estimated by numerical simulations. However, numerical simulation of large sample clusters is very time consuming. A simulation of 580 Å sample size would take 40 days on the NJIT Kong cluster using 19

CPU cores. In order to estimate the holograph signal intensity for large sample size before a real experiment is conducted, the method for estimating holographic signal intensity was studied.

The holograph in Equation 5.1 can be rewritten as:

$$\chi(\boldsymbol{k}) = \int \frac{r_e}{r_0} cos(ikr_0 - i\boldsymbol{k}\cdot\boldsymbol{r_0})\rho(\boldsymbol{r_0})L(\boldsymbol{k},\boldsymbol{r_0})\mu(r_0)d\boldsymbol{r_0} \tag{5.9}$$

where, $L(\boldsymbol{k},\boldsymbol{r_0})$ is the Lorenz factor that represents the effect of polarization in the scattering. $\mu(r_0)$ is a profile factor that represents sample cluster size, shape and attenuation effect when X-ray travels inside the sample material. $\rho(\boldsymbol{r_0})$ is the electron density function of the sample.

Since the hologram $\chi(\boldsymbol{k})$ is extracted from the isotropic fluorescence background, the average signal intensity $\chi(\boldsymbol{k})$ of hologram is zero. Thus, the root mean square (RMS) intensity of the holograph is given by:

$$RMS[\chi(\boldsymbol{k})] = \sqrt{\frac{\oiint[\chi(\boldsymbol{k})-0]^2 d\sigma}{4\pi k^2}}$$
$$= \sqrt{\frac{1}{4\pi k^2}}\bar{\rho}\sqrt{\oiint\left(\int \frac{r_e}{r_0}\mu(r_0)dr_0 \oiint cos(ikr_0 - i\boldsymbol{k}\cdot\boldsymbol{r_0})\frac{\rho(\boldsymbol{r_0})}{\bar{\rho}}L(\boldsymbol{k},\boldsymbol{r_0})d\hat{\boldsymbol{r}}_{\boldsymbol{0}}\right)^2 d\Omega_k} \tag{5.10}$$

where, $\bar{\rho}$ is averaged electron density of $\rho(\boldsymbol{r_0})$. Angular integration in Equation 5.9 is separated from radical integration in Equation 5.10.

One can define the integrand as variable rand as:

$$rand = cos(ikr_0 - i\boldsymbol{k}\cdot\boldsymbol{r_0})\frac{\rho(\boldsymbol{r_0})}{\bar{\rho}}L(\boldsymbol{k},\boldsymbol{r_0}) \tag{5.11}$$

Rand is a complex function that depends on many variables but its value only changes in a limited range. Here assumption is made that the rand variable can be treated as a random function. The assumption is verified numerically.

For random function rand one has:

$$\left(\oiint rand\, d\hat{\boldsymbol{r}}_{\boldsymbol{0}}\right)^2 = \left(\oiint rand^2\, d\hat{\boldsymbol{r}}_{\boldsymbol{0}}\right) \tag{5.12}$$

In order to verify the validity of the assumption, $(\oiint rand\, d\hat{\boldsymbol{r}}_{\boldsymbol{0}})^2$ and $(\oiint rand^2\, d\hat{\boldsymbol{r}}_{\boldsymbol{0}})$ values were calculated on CuAu model on 32 different r_0 values. The integration is performed on a 6 Å thick spherical layer of atoms in the model simulation. The numerical result is shown in Figure 5.5.

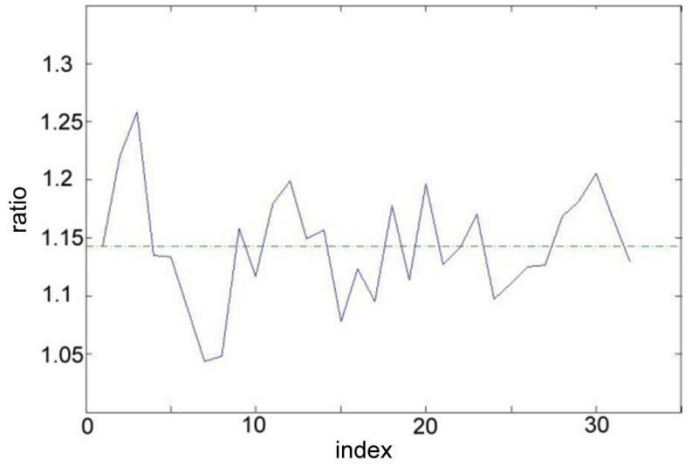

Figure 5.5 The plot of $(\oiint rand\, d\hat{\boldsymbol{r}}_{\boldsymbol{0}})^2 / \oiint rand^2\, d\hat{\boldsymbol{r}}_{\boldsymbol{0}}$.

The result in Figure 5.5 has an averaged ratio ~1.14 and fluctuates between 1.05 and 1.25. Although the value is not exactly 1, the approximation is good enough for an estimation of signal intensity; the error of estimation should be around 14%.

With the assumption that $cos(ikr_0 - i\boldsymbol{k}\cdot\boldsymbol{r}_{\boldsymbol{0}})\frac{\rho(\boldsymbol{r}_{\boldsymbol{0}})}{\bar{\rho}}L(\boldsymbol{k},\boldsymbol{r}_{\boldsymbol{0}})$ can be treated as a random number, the RMS value of the holograph is easily formulated as:

$$RMS[\chi(\boldsymbol{k})] = RMS(rand)r_e\sqrt{\frac{1}{4\pi k^2}}\int dr_0\frac{\bar{\rho}}{r_0}\mu(r_0)(4\pi k r_0) \tag{5.13}$$

The $RMS(rand)r_e\sqrt{\frac{1}{4\pi k^2}}$ factor is a constant value. The RMS value of a holograph only depends on the average electron density and cluster size profile. An estimation of holograph signal intensity can be performed with integration in Equation 5.13.

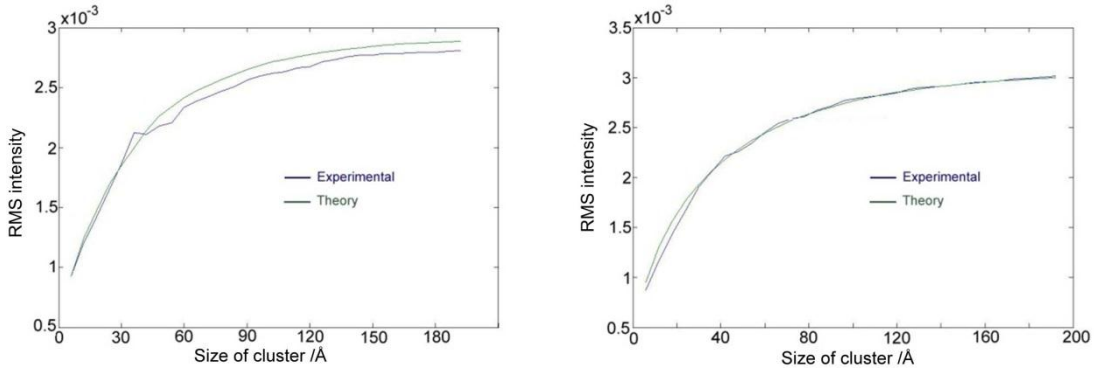

Figure 5.6 Plot of experimental RMS signal intensity of holograph for $\mu(r_0) = 1$ (left) and $\mu(r_0) = \exp(-0.0085r_0)$ (right) with theoretical estimation given by Equation 5.13. A $RMS(rand)$ value is fitted from experimental results and used in the estimation of the signal intensity.

The CuAu holograms were simulated based on two different profile functions $\mu(r_0) = 1$ and $\mu(r_0) = \exp(-0.0085r_0)$ and various sample cluster sizes from a radius of 6 Å to a radius of 192 Å. A universal RMS(rand) number is fitted from the simulation results and used to calculate the estimated signal intensity for all situations. Figure 5.6 are the results that compare numerical simulation results of RMS signal intensity with estimation given by Equation 5.13.

The results indicate that the assumption of random number treatment on signal intensity estimation is valid and is useful to give estimation on XFH holograph signal intensity level based on sample electron density and cluster profile.

5.4 Extracting Kossel Line Signals from a Noisy Holograph with Non-linear Fitting Method

Experimentally measured holograms are often too noisy to be directly reconstructed. It is possible to separate signals in holograms from noise based on the fact that noise in holograph is not inter-correlated while signals in a hologram have certain symmetry. A non-linear fitting method was developed to extract Kossel line signals from a noisy holograph.

5.4.1 Kossel Line of Holograph Signals

The holograph in Equation 5.1 can be rewritten as an integration of electron density:

$$\chi(\boldsymbol{k}) = \int \frac{r_e}{r_0} Exp(ikr_0 - i\boldsymbol{k}\cdot\boldsymbol{r_0})\rho(\boldsymbol{r_0})L(\boldsymbol{k},\boldsymbol{r_0})\mu(r_0)d\boldsymbol{r_0} \qquad (5.14)$$

where, $L(\boldsymbol{k},\boldsymbol{r_0})$ represents the Lorenz factor of an electron at r_0 point, i.e, the polarization factor for X-ray scattering on electron. $\mu(r_0)$ is the cluster profile factor and it represents attenuation of X-ray traveling in sample material:

$$\mu(r_0) = \exp(-\mu r_0) \qquad (5.15)$$

Electron density $\rho(r_0)$ can be expressed in terms of structure factors:

$$\rho(\boldsymbol{r_0}) = \sum_{\boldsymbol{h}} \rho(\boldsymbol{h}) Exp(i\boldsymbol{h}\cdot\boldsymbol{r_0}) \qquad (5.16)$$

If one consider direct scheme un-polarized (or depolarized) Lorenz factor and neglect near field effects, $L(\boldsymbol{k}, \boldsymbol{r_0})$ would be given by (as shown in Chapter 4) $1 - (\boldsymbol{k} \cdot \boldsymbol{r_0})^{\boldsymbol{2}}$ **.** Thus:

$$\begin{aligned} \chi(\boldsymbol{k}) &= \sum_k \int \frac{r_e}{r_0} [1 - (\boldsymbol{k} \cdot \boldsymbol{r_0})^{\boldsymbol{2}}] e^{ikr_0 - \mu r_0} e^{i\boldsymbol{h}\cdot\boldsymbol{r_0} - i\boldsymbol{k}\cdot\boldsymbol{r_0}} d\boldsymbol{r_0} \\ &= r_e \sum_k \chi(\boldsymbol{k}, \boldsymbol{h}) \rho(\boldsymbol{h}) \end{aligned} \tag{5.17}$$

where, $\chi(\boldsymbol{k}, \boldsymbol{h}) = \int \frac{1}{r_0} [1 - (\boldsymbol{k} \cdot \boldsymbol{r_0})^{\boldsymbol{2}}] e^{ikr_0 - \mu r_0} e^{i\boldsymbol{h}\cdot\boldsymbol{r_0} - i\boldsymbol{k}\cdot\boldsymbol{r_0}} d\boldsymbol{r_0}$ is the resonant Kossel line of the $\boldsymbol{h}^{\text{th}}$ structure factor index. The integration can be easily carried out and gives the following results:

$$\begin{aligned} \chi(\boldsymbol{k}, \boldsymbol{h}) &= \int \frac{1}{r_0} [1 - (\boldsymbol{k} \cdot \boldsymbol{r_0})^{\boldsymbol{2}}] e^{ikr_0 - \mu r_0} e^{i\boldsymbol{h}\cdot\boldsymbol{r_0} - i\boldsymbol{k}\cdot\boldsymbol{r_0}} d\boldsymbol{r_0} \\ &= \frac{3 - \left(\hat{\boldsymbol{k}} \cdot (\widehat{\boldsymbol{h} + \boldsymbol{k}})\right)^2}{2} \frac{-4\pi}{(h + i\mu)^2 - |\boldsymbol{h} + \boldsymbol{k}|^{\boldsymbol{2}}} + \left[3\left(\hat{\boldsymbol{k}} \cdot (\widehat{\boldsymbol{h} + \boldsymbol{k}})\right)^2 - 1\right] * \\ &\quad \left[\frac{-2\pi}{|\boldsymbol{h} + \boldsymbol{k}|^{\boldsymbol{2}}} + \frac{-2\pi(k + i\mu)^2 / |\boldsymbol{h} + \boldsymbol{k}|^{\boldsymbol{2}}}{(h + i\mu)^2 - |\boldsymbol{h} + \boldsymbol{k}|^{\boldsymbol{2}}} + \frac{-2\pi(k + i\mu)}{|\boldsymbol{h} + \boldsymbol{k}|^{\boldsymbol{3}}} log \frac{(k + i\mu) + |\boldsymbol{h} + \boldsymbol{k}|}{(k + i\mu) - |\boldsymbol{h} + \boldsymbol{k}|}\right] \end{aligned} \tag{5.18}$$

5.4.2 Extracting Kossel Lines $\chi(\boldsymbol{k}, \boldsymbol{h})$ from Noisy Hologram

Equations 5.15 and 5.16 give us a method to calculate Kossel line signals from a few parameters including $\rho(\boldsymbol{h}), \boldsymbol{h}$ and μ. If one assumes that the signals in the hologram are composed of a finite number of Kossel lines, one has a non-linear equation:

$$\chi(\boldsymbol{k}) = \chi(\boldsymbol{h_1} \cdots \boldsymbol{h_n}, \rho(\boldsymbol{h_1}) \cdots \rho(\boldsymbol{h_n}), \mu_1 \cdots \mu_n) \tag{5.19}$$

For any given hologram $\chi(\boldsymbol{k})$, it is possible to perform the non-linear fitting method of Equation 5.18 to solve for parameters $\rho(\boldsymbol{h}), \boldsymbol{h}$ and μ.

The CuAu hologram at $k = 14.5keV$ is measured with polarized X-rays on NSLS beamline X14A and the non-linear fitting is performed with a steepest descent algorithm [141, 142]. Figure 5.7 is the nonlinear fitting result plotted together with the original holograph. The fitted result hologram is built from fitting parameters in Equation 5.19.

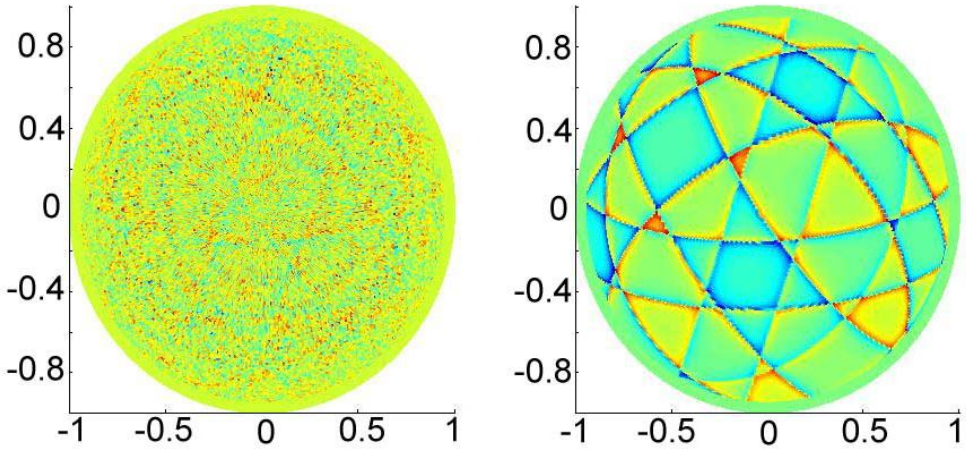

Figure 5.7 Nonlinear fitting results (right) plotted together with original holograph (left).

Table 5.1 summarizes the non-linear fitting results of the CuAu holograph. The CuAu holograph contain more than 700 Kossel line but only seven Kossel lines are considered in the non-linear fitting. The number of Kossel lines is limited by complexity and stability of the non-linear fitting algorithm. The result suffers from errors partially due to the limited number of Kossel line parameters and partially due to the fact that polarization is not properly suppressed. However, meaningful results were successfully extracted from the noisy original holograph as clearer Kossel lines are displayed in Figure 5.7.

Table 5.1 Non-linear Fitting Results of the CuAu Hologram

(hkl)	$\rho(h)$	$\|h\|$	μ
(100)	1.067046E-05	3.357004	-3.754705E-01
(010)	9.931009E-06	3.421202	-3.811271E-01
(001)	9.132409E-06	3.593153	-6.981951E-01
(111)	6.925094E-06	2.594162	-1.992746E-01
(-111)	1.018289E-05	2.681190	-3.657472E-01
(1-11)	5.723137E-06	2.598517	-2.132494E-01
(11-1)	6.666318E-06	2.733280	-4.327589E-01

5.4.3 Conclusions

For a holograph with a limited number of Kossel lines and measured from un-polarized or de-polarized X-rays, it is possible to extract Kossel line signals from a noisy hologram with a non-linear fitting method.

5.5 Numerical Simulation of Multiple Energy XFH in Barton's Algorithm

As already stated in Chapter 1, the multiple energy XFH (MXFH) Barton's reconstruction algorithm is given by:

$$U(r) = \sum_{k} \exp(ikr) \iint_{s} \chi(\boldsymbol{k}) exp(\mathrm{i}\boldsymbol{k} \cdot \mathbf{r}) d\Omega_k \tag{5.20}$$

The reconstructed image U(r) for any real space region will be affected from signals from other real space regions and will cause noise. Roughly speaking, using more energies in MFXH reconstructions results in lower noise in the reconstructed image. In order to quantitatively estimate the number of multi-energy holographs required to give reasonably low noise real space reconstructions, a study on a CuAu sample was conducted.

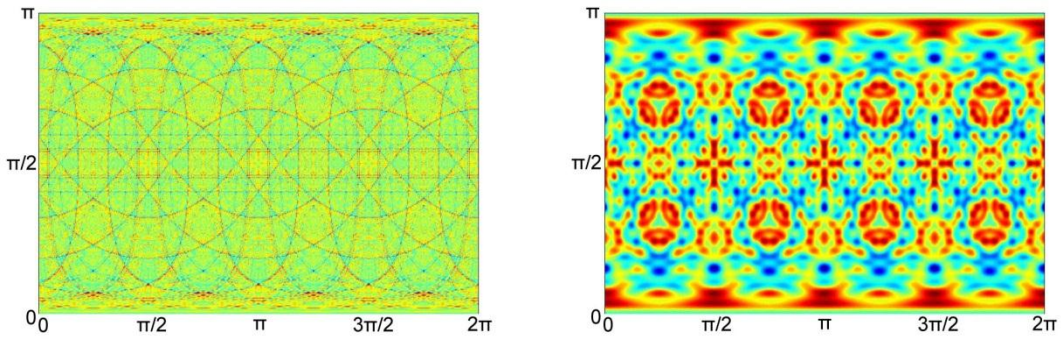

Figure 5.8 Sample simulated holograph for k = 10.8 keV from a 31x31x31 unit cell model (left) and 5x5x5 unit cell model (right).

64 holograms (Figure 5.8) from equally separated X-ray energies between 11 keV and 17 keV for a 31x31x31 unit cell model are calculated. As a reference, 64 holographs of corresponding X-ray energy for 5x5x5 unit cell model are simulated. The absorption coefficient for X-rays traveling in the CuAu sample in the simulation is given in Figure 5.9 [41].

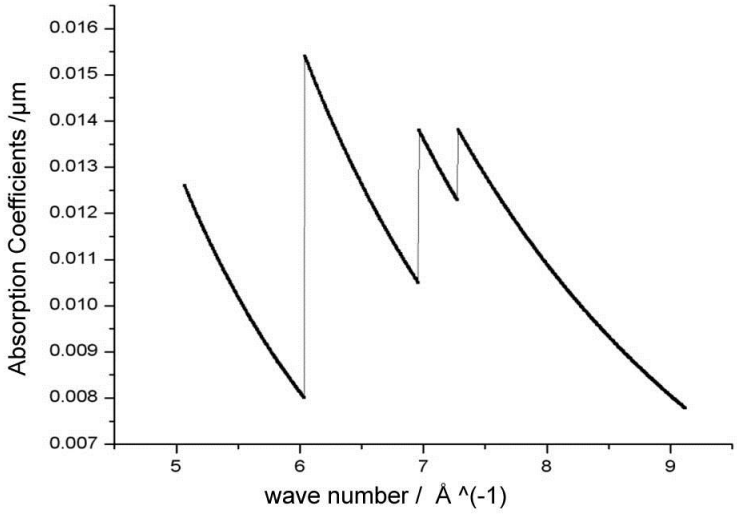

Figure 5.9 Absorption coefficients μm as a function of wave number $k/\text{Å}^{-1}$ using CuAu in holograph simulation.

The simulated holograph is then reconstructed to show the real space image on the 5x5x5 unit cell region. Reconstruction of holographs simulated from the 5x5x5 model are used as the 'ideal real space image' for that there is no noise due to longer distance atoms. Reconstruction results from holographs simulated with the 31x31x31 model real experiments and difference between the reconstructed image and the 'ideal real space image' are considered as noise.

Figure 5.10 is reconstructed real space image for holograph simulated at wave number k equal to 4.5 / $Å^{-1}$, 5.0 / $Å^{-1}$ and 5.5 / $Å^{-1}$. The results for larger cluster size show significantly different image from the ideal image for small cluster. The difference is noise due to ripple signals from atoms is not located in the reconstructed real space region.

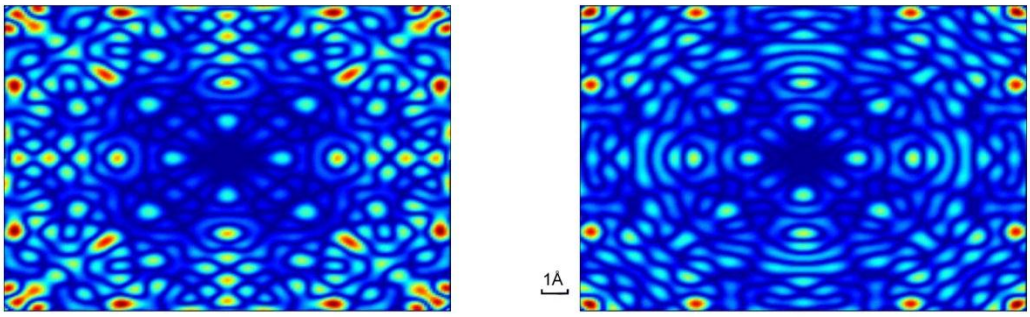

Figure 5.10 Three energy reconstructed real space image for 31x31x31 unit cell model (left) and for 5x5x5 unit cell model (right) as 'ideal image'.

The relationship between noise levels and number of energies used in reconstruction is shown in Figure 5.10. The noise level is calculated by the ratio of RMS intensity of noise to RMS intensity of 'ideal image'.

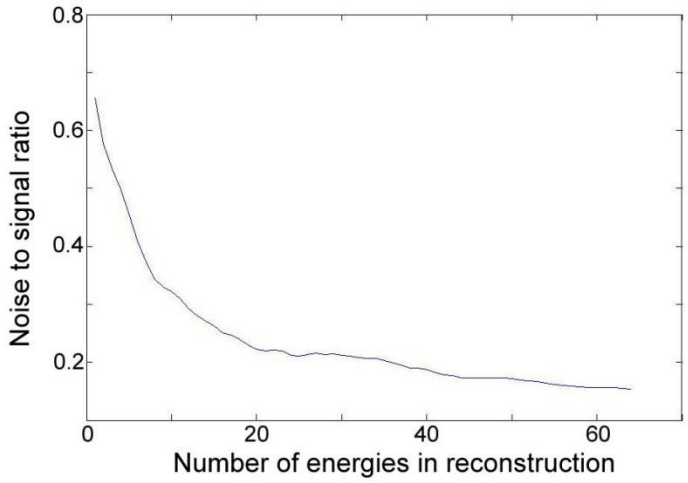

Figure 5.11 Relationship between noise level and number of distinct energy holographs included in MXFH reconstruction.

Results in Figure 5.11 show a fast decrease in noise level for the first ten energies used in MXFH reconstruction. The effect of noise reduction is reduced when extra energies are added into the MXFH reconstruction. This suggests that MXFH measurement should try to include at least ten energies, which gives a noise level of 30%.

5.6 Study of the Scattering Pattern Matrix (SPM) Method

5.6.1 Introduction

The scattering Pattern Matrix (SPM) method is an algorithm used to generate a real space electron density function that has an X-ray Holograph pattern that is the best fit to a measured holograph.

The operation that calculates the hologram function $\chi(\boldsymbol{k})$ from the real space electron density function is numerically a matrix operation given by:

$$\chi(\boldsymbol{k}) = T_{\boldsymbol{r_0}}^{\boldsymbol{k}} \cdot \rho(\boldsymbol{r_0}) \tag{5.21}$$

where, $\chi(\boldsymbol{k})$ is the hologram, $\rho(\boldsymbol{r_0})$ is electron density in real space and $T_{\boldsymbol{r_0}}^{\boldsymbol{k}}$ is the transformation matrix. The elements in the transformation matrix are given by:

$$T_{\boldsymbol{r_0}}^{\boldsymbol{k}} = Re\left[\frac{r_e}{r_0} Exp(ikr_0 - i\boldsymbol{k}\cdot\boldsymbol{r_0}) Lorenz(\boldsymbol{k}, \boldsymbol{r_0})\right] \tag{5.22}$$

To solve large matrix equations like Equation 5.22, a least square fitting solution can be attained by the steepest descent method [141].

The steepest descent method is an iteration beginning from a trial real space electron density function ρ_0, and iterates the following equations to approach the real solution:

$$\begin{aligned} e &= \left|\chi - T_{\boldsymbol{r_0}}^{\boldsymbol{k}} \cdot \rho_n\right| + \gamma|\,\rho_n| \\ \rho_{n+1} &= \rho_n - 1/2\alpha_n(\partial e/\partial\,\rho_n) \end{aligned} \tag{5.23}$$

where, e is the residual error, γ and α_n are interaction parameters which control convergence of the iteration. The final converged result of iteration gives the electron density which is the approximate solution of the input hologram.

5.6.2 Simulation Results on Single Atomic Model

In order to study the resolution power of the SPM method, nine holograms with deferent X-ray energies between 10 keV and 18 keV are simulated for a simple model of a delta-function electron density placed 4 Å from a fluorescent center.

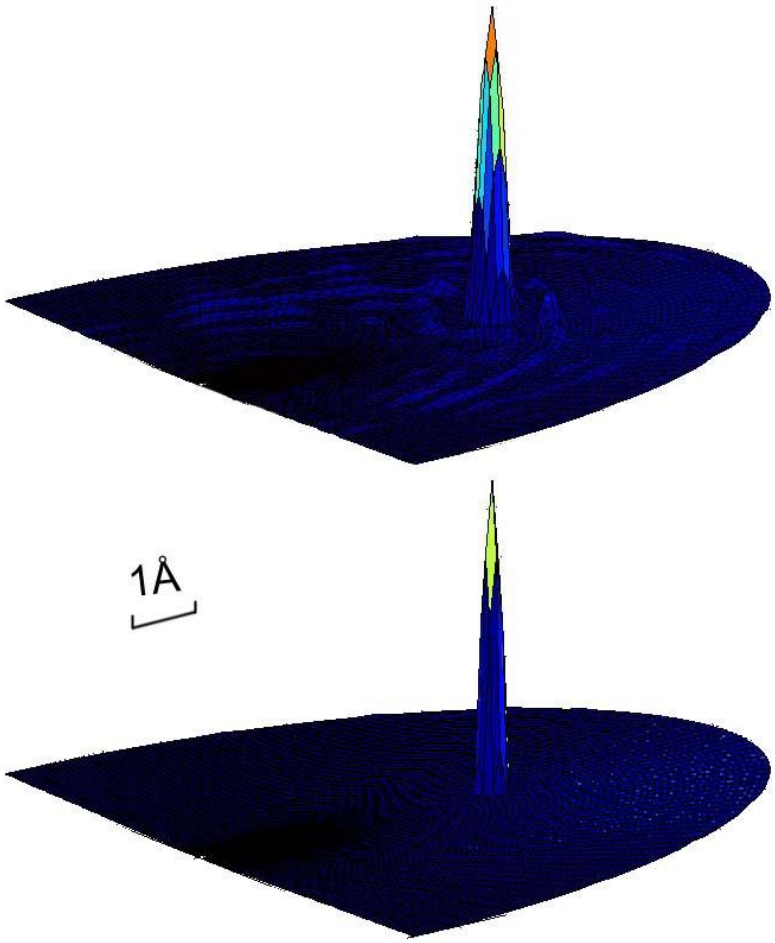

Figure 5.12 Reconstructed image of the holograph with least square fitting method without non-negative constraint (upper) and with non-negative constraint (lower).

Non-negative constraint is studied in the process of integration. Figure 5.11 is a comparison of the reconstructed image of the holograph with the SPM method without non-negative constraint and with non-negative constraint. The non-negative constraint forces $\rho(\boldsymbol{r_0})$ is considered to be non-negative during iteration.

Ripples in the upper image of Figure 5.12 result from the fact that simulated holograms have limited information in k-space in a way similar to a numerical aperture in microscopes. The result in the lower image of Figure 5.12 shows that, with the help the help of non-negative constraints, the least square fitting algorithm is able to suppress the

partially negative ripples in the reconstructed image and results in resolution that is better than the limit of the numerical aperture.

In Figure 5.13, holograms of nine deferent energies between 10 keV and 18 keV are simulated on a model with single iron atom placed 4 Å from fluorescent center.

The atomic scattering factor contains information on the electron density distribution inside the iron atom. The hologram was simulated with the atomic scattering factor of the iron atom. It is seen that, for this ideal situation, least square fitting method is capable of discerning the distribution of the electron density inside the iron atom. The solution for the delta-function atomic model gives resolution that is better than the size of the iron atom. Electron distribution inside the image of iron atom can be distinguished from the simulation.

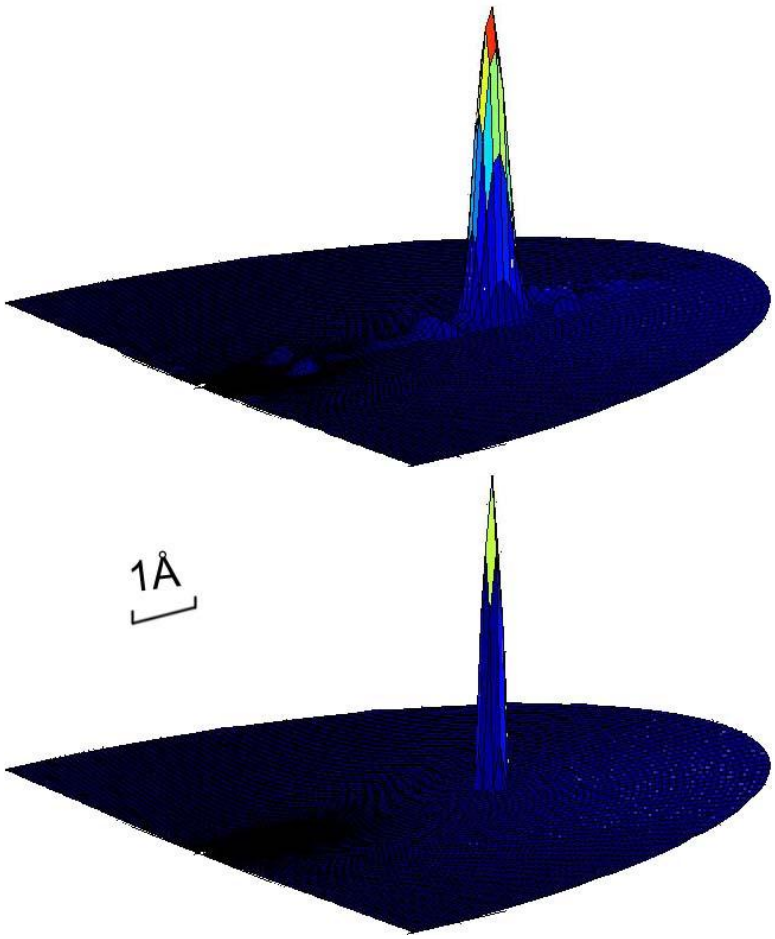

Figure 5.13 The reconstructed electron density function of an iron atom (upper) and the result in Figure 5.11 as a reference (lower) of available resolution. The distance from the atom to the center is 4.0 Å.

5.6.3 Simulation on Mixed Mode XFH Geometry

A special advantage of the SPM method is its ability to handle special XFH geometry. Figure 5.14 is a special XFH measurement geometry that has both detector and incident beam fixed in their position and only the sample is rotated and scanned. Simple set up like this are desirable in experiments but is neither a direct scheme nor inverse scheme. Thus, the hologram from this setup cannot be reconstructed by any Fourier transformation based method. This condition can be easily handled with the least square fitting method.

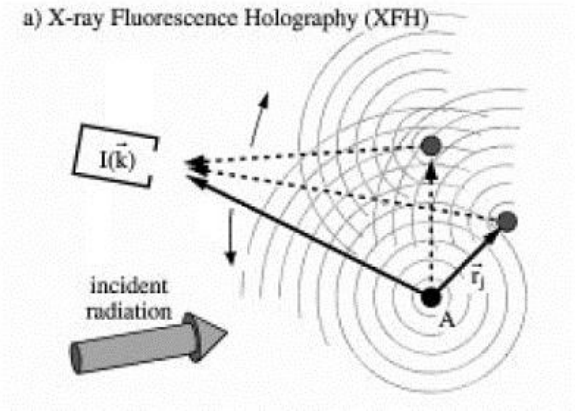

Figure 5.14 A special XFH measurement scheme that results in a mixed holograph. Schematic is modified from [39].

The hologram generated from Figure 5.14 still has the form $\chi(\boldsymbol{k}) = T_{\boldsymbol{r_0}}^{\boldsymbol{k}} \cdot \rho(\boldsymbol{r_0})$ except that, here:

$$T_{\boldsymbol{r_0}}^{\boldsymbol{k}} = Re\left[\frac{r_e}{r_0} Exp(ikr_0 - i\boldsymbol{k}\cdot\boldsymbol{r_0}) L(\boldsymbol{k},\boldsymbol{r_0}) + \frac{r_e}{r_0} Exp(ik_0 r_0 - i\boldsymbol{k_0}\cdot\boldsymbol{r_0}) L(\boldsymbol{k_0},\boldsymbol{r_0})\right] \quad (5.24)$$

where, k is the wave vector of incident X-ray and k_0 is wave vector of the fluorescence X-ray.

Nine holograms with different X-ray energies between 10 keV and 18 keV are simulated with four iron atoms each placed 4 Å from the fluorescent center. The holograms are reconstructed with both Barton's Fourier transform method and the SPM method. Figure 5.15 is a comparison of the reconstructed real space electron density using Barton's Fourier transform method and least square fitting method. The reconstruction with the Barton's method results in images at wrong locations while the SPM method has the image correctly placed.

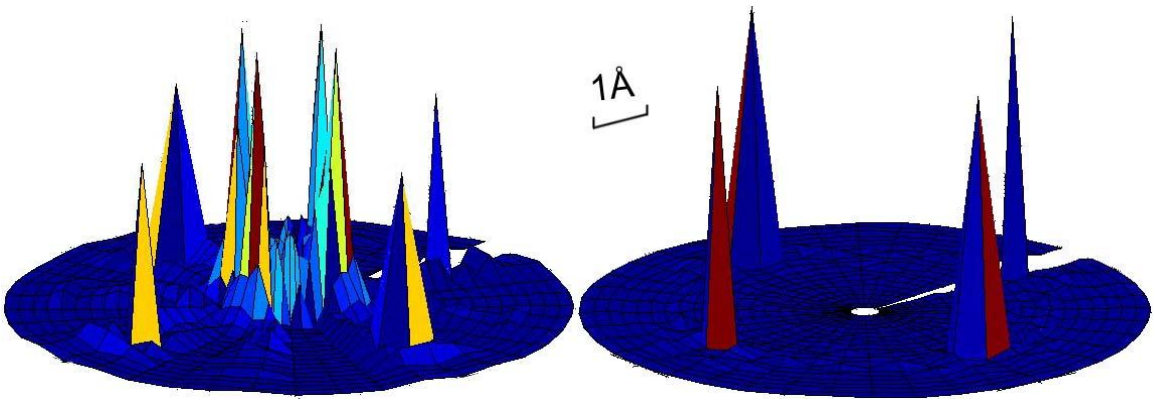

Figure 5.15 Reconstructed real space image with Barton's method (left) and SPM method (right).

5.6.4 Stability and Limitation

The method is stable when noise exists in holograms.

Nine holograms with different X-ray energies between 10 keV and 18 keV are simulated on a iron lattice with different cluster size. Noise was added to hologram.

Figure 5.16 includes holograms and reconstructions with noise added to holograms for simulations on a 5x5x5 unit cell iron cluster simulation. The result for noisy holograms has atomic image with noises added. This result shows that noises in holograms induce noises in the reconstructed image. The more noise present in the holograms, the more noise appears in there constructed image. However, the SPM method is stable to noises in holograms.

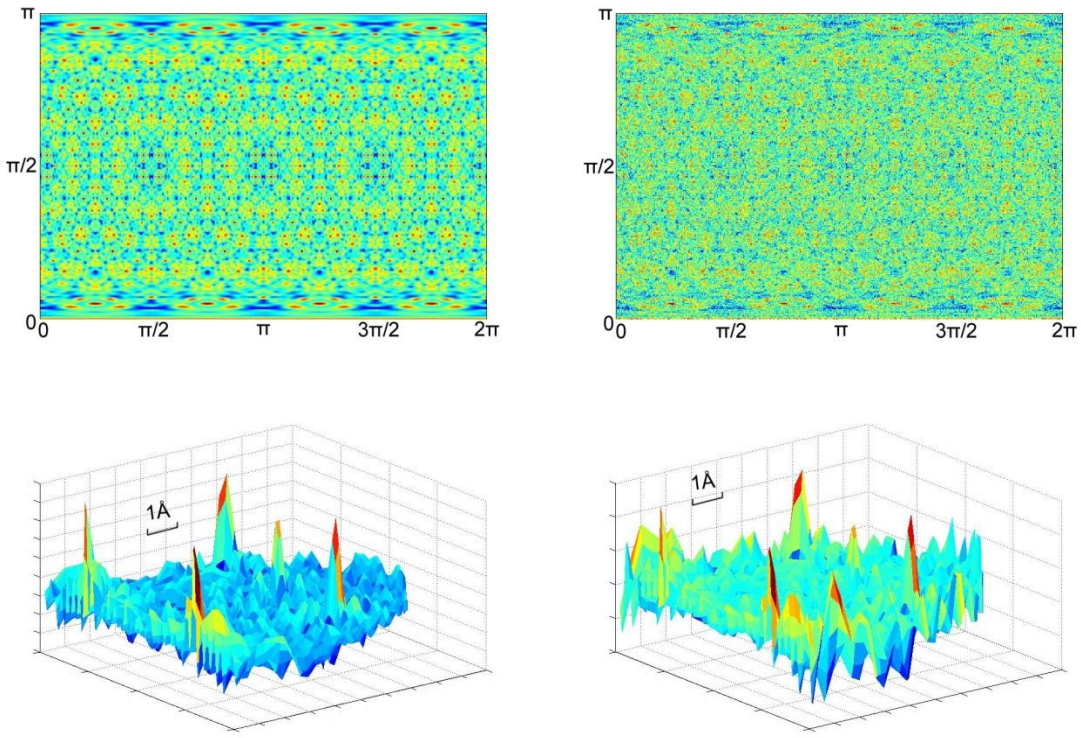

Figure 5.16 Simulated hologram (upper left) and hologram with noise (upper right) and reconstruction result (lower left) with noise added on holograph (lower right).

A limitation of the method is that least square fitting requires a large amount of computation power and always has limited mesh grid to represent real space electron density. The reconstructed electron density function is thus confined to a limited space of around 10 Å. If the holograph one is trying to fit contains signal from atom out of this range, these extra signals not covered by simulation mesh grid will become noise and results in noise in the reconstructed image. Figure 5.17 shows reconstruction results of holograms containing 3x3x3 atom (left), 13x13x13 atom (middle) and 61x61x61 atoms (right). The range of real space mesh grid is 10 Å, corresponding to 2.5 times lattice constant.

The simulation on large cluster size with limited mesh grid leads to more noise than simulation with smaller clusters.

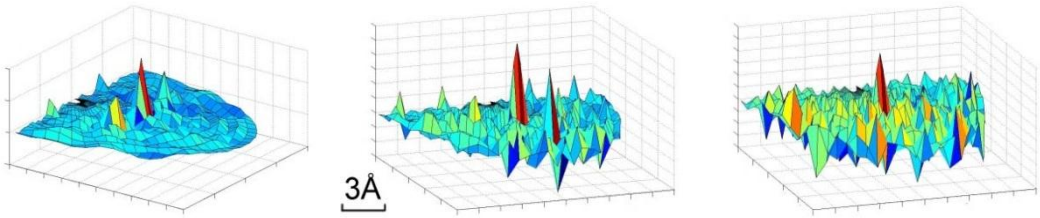

Figure 5.17 Reconstruction result of holograms containing 3x3x3 atoms (left), 13x13x13 atoms (middle) and 61x61x61 atoms (right).

5.6.5 Conclusions

The SPM method is more flexible than a simple Fourier transform method and is capable of handling special XFH measurement schemes. Non-negative constraints can be handled in the SPM method and results in improved real space resolution. The method is stable when noise is imposed on the signal of the holograms. However this method has difficulty handling holograms from large clusters.

CHAPTER 6

PROPOSED FUTURE WORK

6.1 XFH Measurements on Micron-sized Samples

6.1.1 Sample Setup

The HERMES based 384 element detector enables large solid angle acquisition of photons with a large dynamic range (high counting rates). Measuring micron-size samples with reasonable counting rates might be possible with this detector. In order to test the possibility, XFH experiments was performed on a micron-size sample. The PZN-PT sample was chosen for its strong florescence and strong Kossel line intensity.

A micron-size PZN-PT sample was cut from the bulk PZN-PT single crystal and selected under a microscope. The sample size was roughly 50x30x5 μm^3. The single crystal micron-size sample was mounted on a glass fiber with epoxy.

Figure 6.1 is an illustration of the sample location in the X-ray beam spot. The beam is focused to 3.5x1 mm^2 at the X14A beamline.

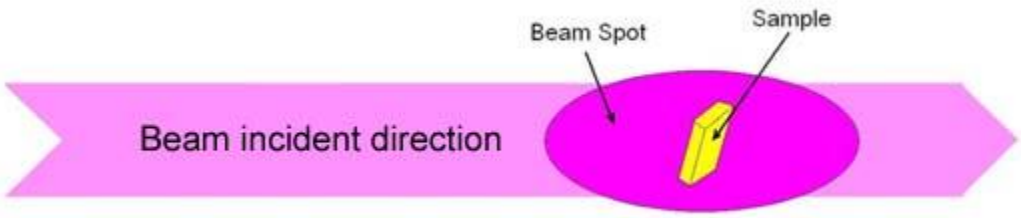

Figure 6.1 The beam spot and size of micron-size sample in the experiment.

6.1.2 Stability Test and Problems

The major difficulty for the XFH experiment on micron-size sample is that the sample is smaller than the beam spot. Unlike standard XFH experiments on bulk samples, the total photon flux incident on the micron-size sample cannot be directly monitored by an ionization chamber.

Figure 6.2 compares the result of a stability measurement on bulk sample Si-$Ge_{10\%}$ and micron sized PZN-PT sample. A noise level of 0.001 is typical for bulk samples when the count rate is around 20,000 cps per element. For micron-size PZN-PT sample, however, noise level is about 0.005 at 8,000 cps per element.

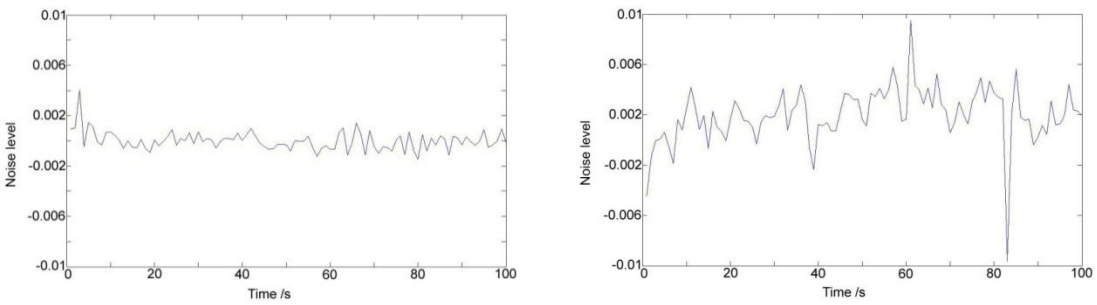

Figure 6.2 Noise level of stability verses time measurement on bulk Si-$Ge_{10\%}$ with 20k cps per element (left) and noise level for stability measurement on micron-size PZN-PT sample where count number is 8k per second per element (right).

Although the low count rate (at 8,000 cps per element) in micron size sample increases statistical noise, the noise level should be less than 0.0015 as postulated from the noise level measured with bulk samples (at 20,000 cps per element). The unexpectedly poor stability for micron-size samples is actually influenced also by the change in total photon flux illuminating the sample. The instability in illumination cannot be removed by normalization with ionization chamber reading.

The 0.005 noise level, however, is low enough to allow for XFH measurements on samples with strong Kossel lines like the PZN-PT sample.

6.1.3 XFH Scan on Micron-sized PZN-PT Samples

Currently, no method of normalization has been successfully performed on micron-size samples. For the time, normalization is not used but it is assumed that the illuminating beam is a stable beam pure random noise only. By taking XFH scans over a long time, and averaging, the influence for all random noise from the illumination, theoretically, the influence can be averaged out and noise level can be reduced.

Eight independent scans have been performed with the same condition with an average count rate of 5,000 cps per element. Note that the scan condition here is not the same scan condition as for the stability test. Slits have been reduced in the eight scans with the hope to reduce the difference between ionization chamber reading and real incident flux. Roughly each pixel in the scan has 0.6 second accumulation time.

Figure 6.3 shows the average for the eight scans that are used to produce the XFH holograms on the micron-size PZN-PT sample. The shape factor in the holograph measurement is considered and removed to the best of our capability. Even after careful shape factor correction, the noise level of the averaged holograph is still 0.01. This noise level is too large for observing Kossel lines. The noise comes from irregular geometry of the micron-size sample which results in random fluctuation of the XFH signal. This clearly suggests that a micron-size sample with very regular shape is required for clean XFH measurement and for removal of shape factor from measured XFH signals. This can be done by careful selection of single crystal grains under a microscope. The grain

can be modified by cleaving them, also under a microscope. Small beams on 3rd generation light sources (~1 μm diameter) may resolve these problems.

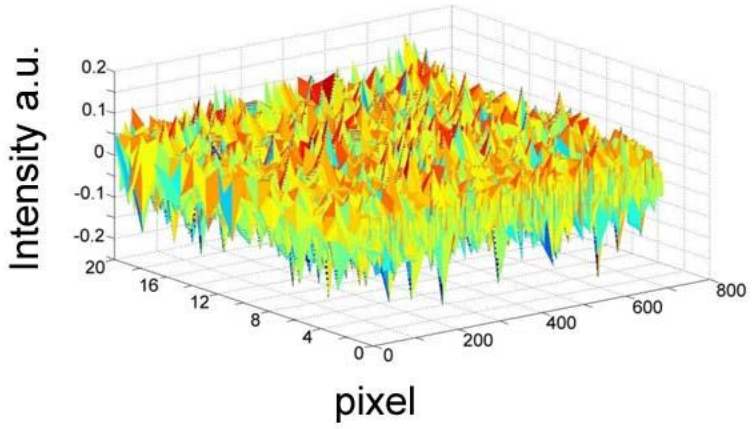

Figure 6.3 The averaged eight XFH scan hologram on micron-size PZN-PT sample with same conditions.

6.2 Suggestions for Future Work

Work in this thesis indicates that the XFH method is a promising experimental method that is capable of investigating sample structural information without prior knowledge. As the XFH method involves multiple technologies under development, some important components are needed for the method to be fully utilized:

A high count rate silicon drift detector (SDD) based multi-element detector should be built. The SDD detector should have ~150 eV resolution to provide cleaner fluorescence-elastic photon separation. The author proposes a 96 element SDD detector array with a total 16 cm^2 detector active area.

The XFH measurement setup should be improved. Better beamline stability is absolutely essential to provide smaller flux fluctuation in the incident beam, I_0, thus reducing noise in measurements. Flux should be monitored with same type of detectors

that monitors the fluorescence rather than ionization chamber. This provides better match in detector response and yields higher level of normalization.

The possibility to measure XFH holograms on micron-size sample should be investigated. A more uniform distribution of flux intensity in the beam spot of XFH measurement is desired because it reduces difficulty in I_0 normalization. Better stability of beamline flux also reduces noise due to I_0 normalization. Vibration isolation is required to provide better beamline optical stability. Using very small crystals at 1μm size should possibly reduce effect of shape factor, however, it also increases the requirement for high beamline photon flux. The author proposes a micron-size sample measurement with 10^{15} cps photon flux that is focused on a uniformly distributed 100μm diameter beam spot in a sample with 5μm diameter crystal size. The shape of the sample should be made close to a sphere.

A theoretical investigation of non-isotropic atomic scattering should be performed. The simulations in this thesis are based on a structure factors that assumes isotropic symmetry of the electron distribution in individual atoms. This is not valid for highly covalent systems such as carbon networks (graphene) and many organic systems. Thus atomic scattering factor, A_{sf}, is independent of orientation but is only a function of scattering angle.

$$A_{sf} = A_{sf}(\mathbf{k} \cdot \mathbf{k_0}) \tag{6.1}$$

Here, the atomic scattering factor is determined by the relative angle between $\mathbf{k}$ and $\mathbf{k_0}$. In the general case, the scattering factor can depend on $\mathbf{k}$ and $\mathbf{k_0}$ vectors and not just on the relative angle.

$$A_{sf} = A_{sf}(\mathbf{k}, \mathbf{k_0}) \tag{6.2}$$

The general case will be used to model highly anisotropic charge distributions such as covalent organic frameworks.

This A_{sf} can be realized numerically in simulations and can be used to simulate a holograph with non-isotropic electron density in atoms to represent inter-atomic interaction. Structure factors can be solved with the same method as in the simulation on isotropic atomic scattering factors and a real space image with inter -atomic interaction can be reconstructed.

APPENDIX A

ALGORITHM FOR BEAMLINE TUNING AND PIEZOELECTRIC ACTUATOR PSEUDO MOTOR CONTROL

The NSLS X14A beamline is configured to automatically tune beamline optics for maximum photon flux. The detailed algorithm for this control is given in this section.

A.1 The Piezoelectric Actuator Pseudo Motor

The piezo-system JENA piezoelectric actuator is remotely controlled by the X14A beamline FOURC [122] pseudo motor utility. The pseudo motor for the piezoelectric actuator is named 'pzo' in the FOURC software interface.

The 'pzon' script, shown in the following Table A.1, is used to turn on remote control of the piezoelectric controller and setup the communication protocol between FOURC and the piezoelectric controller.

Table A.1 'pzon' Script

```
ser_put (0 , ”i1\r” ) ;
cdef ( ”usergetangles” , ”serpar ( 0, \”flush\” ) ; ” , ”pzo” ,0x1 ) ;
cdef ( ”userpostmove” , ”serpar ( 0 , \” flush\” , 1 ) ;
ser_put ( 0 ,sprintf ( \” wr ,%5.2 f \\ r \” ,A[ pzo]+0.2 ) ) ; ” , ” pzo” ,0x1 ) ;
        p  ”piezosystem jena is now online ! ” ;
```

Once remote control of the piezo-system JENA piezoelectric actuator is setup, the 'pzo' pseudo motor in FOURC software will be connected to the real actuator. The operator can move the piezoelectric actuator as any other motors in the X14A beamline.

The ‘pzoff’ script, shown in the following box Table A.2, is used to disable remote control access of the piezoelectric controller and clean up the communication protocol setup between FOURC and the piezoelectric controller.

Table A.2 ‘pzoff’ Script

```
cdef ( ”usergetangles” , ”” , ”pzo” ,0x1 ) ;
cdef ( ”userpostmove” , ”” , ” pzo” ,0x1 ) ;
ser_put ( 0 , ”i0\r ” ) ;
        p ” piezosystem jena is now offline ! ” ;
```

When the connection is turned off, the operator on FOURC system can still execute command on the ‘pzo’ pseudo motor, but the command will have no effect.

The ‘pzhelp’ script, shown in the following box Table A.3, displays help messages for user’s convenience.

Table A.3 ‘pzhelp’ Script

```
p ” pzon / pzoff / pzhelp : the piezosystem jena remote control
    script and help file .  \n
    writen by WANG YUHAO in june 2008 .  email: wy8@njit.edu .  \n \n
    usage in fourc: \n
FOURC> do pzon   :   turn on piezosystem jena remote control.  \n
        FOURC> do pzoff   :  turn off piezosystem jena remote control.  \n ” ;
```

A.2 The Automatic Monochromator Tuning Script

The macro ‘monotune.mac’ (Table A.4) is the macro performing automatic adjustments to align beam optics. This macro scans the piezoelectric actuator to locate the best monochromator crystal position, which gives maximum photon flux. The content of this macro is shown below.

Table A.4 ‘monotune’ Script

```
def monotune ’
chk_beam_off
# cscan_off
plotselect I00
umvr pzo -10
dscan pzo 0.2 20 40 .2
usleep 2.0
p ser_par ( 0 , ” flush” , 2 )
umv pzo pl_xMAX
chk_beam_on 10000
# cscan_on
        plotselect det
```

APPENDIX B

ALGORITHM FOR MONITORING LOCATION OF THE SIMPLE DC MOTOR

Similar to the piezoelectric actuator controller, some codes to communicate between the FOURC main beamline control software and the pulse counter circuit are developed.

The ‘dcon’ script, shown in the following Table B.1, is used to setup communication protocol between FOURC and the counter circuit.

Table B.1 ‘dcon’ Script

```
do DCphiscan.mac ;
cdef ( ”user_scan_loop” , ” DCphiscan ” , ” DCmotor ” ) ;
        p ” DC motor is now online ! ” ;
```

The ‘dcon’ register predefined functions ‘DCphiscan’ to FOURC system’s ‘user_scan_loop’ interface, and then registers the print line to indicate the dc motor is online.

The ‘dcoff’ script, shown in the following box Table B.2, is used to clean up the communication protocol setup by ‘dcon’ script.

Table B.2 ‘dcoff’ Script

```
cdef ( ” user_scan_loop” , ”” , ” DCmotor ” ) ;
        p ” DC motor is now offline ! ” ;
```

The ‘dcreset’ script, shown in the following box Table B.3, resets the counting number in the circuit to zero.

Table B.3 ‘dcreset’ Script

```
port_put ( x37a , 0xf4 ) ;
usleep 0.01
        port_put (0x37a , 0xf3 ) ;
```

A predefined ‘DCphiscan function is included in ‘monotune.mac’ macro. This macro is used as a library file in the ‘dcon’ script. The content of this macro is shown below in Table B.4.

Table B.4 ‘DCphiscan’ Macro

```
long array PHIARRAY[ 4 ] [ 500 ] ;
global PHIARRAY;
def DCphiscan ’
port_put (0x37a , 0xf3 ) ;
local integer i , j ;
local integer raw , angle , angle0 ;
local integer S00 , S30 , S50 ;
local integer CS3 , CS0 ;
PHIARRAY=0;
for ( j =0; j <60; j ++) {
on (DATAFILE) ; offt ;
count_em 1000;
sleep ( 0.5 ) ;
get_counts ;
CS3=S [ 3 ] / 60 ;
CS0=S [ 0 ] / 60 ;
raw = port_get (0x378 ) ;
angle =( ( raw-raw%16) / 16 )%5*100+raw%16*10;
raw = port_get (0x379 ) ;
angle = angle + ( raw - 7) / 8 ;
angle0 =angle ; S30=S [ 3 ] ; S00=S [ 0 ] ; S50=S [ 5 ] * 1000 ;
for ( i =0; i <1000; ){
get_counts ;
```

Table B.4 ‘monotune’ Macro Continued

```
raw = port_get (0x378 ) ;
angle =( ( raw- raw%16) / 1 6 )%5*100+raw%16*10;
raw = port_get (0x379 ) ;
angle =( ( raw-raw%16) / 16 )%5*100+raw%16*10;
raw = port_get (0x379 ) ;
angle = angle + ( raw -7) / 8 ;
if ( ( angle==angle0+1 || angle==angle0-499) && S[5]*1000-S50
<50 && S[3]-S30<CS3*2 && S[3]-S30>CS3/2 && S[0]-S00<CS0*4
&& S[0] -S00>CS0 / 4 ) {
PHIARRAY[ 0 ] [ angle ]=PHIARRAY[ 0 ] [ angle ] + 1.  ;
PHIARRAY[ 2 ] [ angle ]=PHIARRAY[ 2 ] [ angle ] + ( S[3] - S30 ) ;
S30=S [ 3 ] ; S00=S [ 0 ] ; S50=S [ 5 ] * 1 0 0 0 ;
i ++;
angle0 =angle ; }
if ( angle > angle0+1|| angle < angle0 - 100) {
S30=S [ 3 ] ; S00=S [ 0 ] ; S50=S [ 5 ] *1000 ;
i ++;
angle0 =angle ; }
}
}
stop ( 2 ) ;
printf ( ” \n@DET ” )
for ( i =0; i <500; i ++) { printf (”%i ” ,PHIARRAY[ 1 ] [ i ] ) ; }
printf ( ” \n@I0 ” )
for ( i =0; i <500; i ++) { printf (”%i ” ,PHIARRAY[ 2 ] [ i ] ) ; }
printf ( ” \n@HIT ” )
for ( i =0; i <500; i ++) { printf (”%i ” ,PHIARRAY[ 0 ] [ i ] ) ; }
printf ( ” \n ” )
        ont ; off (DATAFILE) ;
```

APPENDIX C

ALGORITHM FOR SOLVING SPHERICAL HARMONIC ANALYSIS MATRIX EQUATION WITH MATLAB

Structure factors can be solved from the spherical harmonic coefficients of the XFH hologram with linear algebra; the algorithm is given in the following code in Table C.1.

The Matlab script first loads pre-calculated matrix elements into the 'Matrix' variable. Then the script loads pre-calculated spherical harmonic coefficients in 'Pa' and 'Pb' variables. A division operation for matrices is performed on selected rows and columns of the matrix to solve structure factor. Finally the result is plotted.

Table C.1 Matlab Script That Solve the Matrix Equation.

```
no_h=678;
Matrix1=load('Matrix_CuAu_rel5550far.txt');
Matrix2=load('Matrix_CuAu_img5550far.txt');
Matrix=[Matrix1(:,1:no_h),Matrix2(:,1:no_h)];
Pa=load('CuAu_Cplx_190A_Pa.txt');
Pb=load('CuAu_Cplx_190A_Pb.txt');
no_l=99;
no_m=20;
Alm=0;
Blm=0;
for i=1:no_l
   for j=1:i
      Alm(i*(i-1)/2+j)=Pa((j-1)*(Pa(1,1))+i+1,3);
      Blm(i*(i-1)/2+j)=Pb((j-1)*(Pb(1,1))+i+1,3);
   end
end
fitting=[Alm(1+no_m*(no_m+1)/2:no_l*(no_l+1)/2),Blm(1+no_m*(no_m+1)/2:
         no_l*(no_l+1)/2)]/[Matrix(11+no_m*(no_m+1)/2:10+no_l*(no_l+1)/2,:);
         Matrix(5001+no_m*(no_m+1)/2:5000+no_l*(no_l+1)/2,:)]';
rho=fitting(1:no_h);
iho=fitting(no_h+1:2*no_h);
         plot([rho;iho]');
```

APPENDIX D

ALGORITHM FOR SIMULATING XFH HOLOGRAM ON KONG CLUSTER

Simulation of a XFH hologram requires long computation times for large crystal sizes. The NJIT Kong cluster is used to make parallel simulations. The following code is the algorithm on Kong cluster that simulates a CuAu hologram.

Table D.1 Simulation Configuration Code Block

```
#include "mpi.h"
#include <math.h>
#include <stdio.h>
#include <string.h>

#define MODEL_X 83
#define MODEL_Y 83
#define MODEL_Z 83
/*model_x,model_y in mpi, model_z inside matrix */

#define LconstX 3.96
#define LconstY 3.96
#define LconstZ 3.67

#define damp -0.000
#define RANGE_S 1.
#define RANGE_L 300.

#define HOLO_phi 1080
#define HOLO_th  1081
        #define HOLO_K   1
```

The above code block in Table D.1 defines the simulation configuration. ‘MODEL_X’, ‘MODEL_Y’ and ‘MODEL_Z’ parameters are the number of unit cells in the simulated cluster. ‘LconstX’, ‘LconstY’ and ‘LconstZ’ are unit cell size in unit of angstroms. ‘damp‘ represent the extinction effect. ‘RANGE_S’ and ‘RANGE_L’ are filters that selects atoms that has distance to fluorescent center within range of ‘RANGE_S’ and ‘RANGE_L’; atoms outside this range are not used in simulation. ‘HOLO_phi’ and ‘HOLO_th’ are resolutions of simulated holograph. ‘HOLO_K’ is the number of various energy values that are used in simulation.

Table D.2 Global Variables

```
const double K_eng[] = {5.55};
int NODES_COUNT;
int PHIOVERNODE;
int numprocs; /* Number of processors */

int MyRank; /* Processor number */
        double Holo[2000][HOLO_th][HOLO_K];
```

The second code block shown in Table D.2 are the global variables in simulation. ‘K_eng[]’ is the array of energies (wave number) of X-ray photons used in the simulation; multiple energy simulations can be defined. ‘NODES_COUNT’ and ‘numprocs-1’ are identically the number of processor nodes allocated to the simulation in the Kong cluster. This determines the degree of parallelization in the numerical simulation. ‘MyRank’ stores the id of the processor which runs the current simulation process. ‘Holo’ is the space where the simulated holograph is stored.

Table D.3 MPI Interface Initialization Subroutine

```
/***********************************************/
int init_const(int argc, char *argv[])
{
        /* Initialize MPI */
        MPI_Init(&argc, &argv);
        /* Find this processor number */
        MPI_Comm_rank(MPI_COmm_WORLD, &MyRank);
        /* Find the number of processors */
        MPI_Comm_size(MPI_COmm_WORLD, &numprocs);
        NODES_COUNT=numprocs-1;
        PHIOVERNODE=HOLO_phi/NODES_COUNT+1;
        return(0);
}

        /***********************************************/
```

The ‘init_const’ subroutine initializes the MPI environment and sets global variables for later reference. This subroutine is run by all processes in the MPI cluster. All processes get the same counts of ‘numprocs’ which is the total number of CPUs available to the simulation. Each individual process of ‘init_const’ gets its own ‘MyRank’ value which is the ID of the processes.

Table D.4 ‘main’ Procedure

```
/***********************************************/
int main(int argc, char *argv[])
{
        /* Initialize MPI */
        init_const(argc, argv);

        /* setting up test holograph */
        Obj2Ptn();
        MPI_Gather(&Holo[MyRank*PHIOVERNODE][0][0],HOLO_th*HOLO_K*PH
IOVERNODE,MPI_DOUBLE,Holo,HOLO_th*HOLO_K*PHIOVERNODE,MPI_DOU
BLE,NODES_COUNT,MPI_COmm_WORLD);
        if (MyRank == NODES_COUNT) { save_holo(); }

        /* Shut down MPI */
        MPI_Finalize();
}

        /***********************************************/
```

The ‘main’ procedure (Table D.4) is the entry point of processes where simulation begins. ‘main’ procedure is dispatched to each allocated processors by MPI environment. It first calls ‘init_const’ to initialize the MPI environment and set global variables. Then the numerical simulation is started in ‘Obj2Ptn’ subroutine to generate the numerical result of the holograph. The ‘MPI_Gather’ system call waits and collects simulation results from all processors and merges them together. Then the merged result is stored to file system within one of the processes. ‘MPI_Finalize’ shuts down the MPI environment.

Table D.5 ‘save_holo’ Subroutine

```
/************************************************/
int save_holo()
{
        int k,th,phi;
        char filename[10];
        FILE * fp[HOLO_K];
        for(k=0;k<HOLO_K;k++)
        {
                sprintf(filename,"ptn%d.txt",k);
                fp[k]=fopen(filename,"w");
                for(phi=0;phi<HOLO_phi;phi++)
                {
                        for(th=0;th<HOLO_th;th++)
                        {
                                fprintf(fp[k],"%e ",Holo[phi][th][k]);
                        }
                        fprintf(fp[k],"\n");
                }
                fclose(fp[k]);
        }
        return(0);
}
        /************************************************/
```

The ‘save_holo’ subroutine saves simulated hologram to file system.

Table D.6 'Obj2Ptn' Subroutine

```
/*************************************************/
int Obj2Ptn()
{
        int fold_i;
        int k,th,phi,x,y,z;
        double rx,ry,rz,r,costh,cosphi,sinth,sinphi,sindelta,AFS,lorenze;

        for (fold_i=0;fold_i<PHIOVERNODE;fold_i++)
        {
                if (MyRank*PHIOVERNODE+fold_i<HOLO_phi)
                {
                        phi=(MyRank*PHIOVERNODE+fold_i);
                                cosphi=cos((phi+1)*3.141592654/2./HOLO_phi);
                                sinphi=sin((phi+1)*3.141592654/2./HOLO_phi);
                        for(k=0;k<HOLO_K;k++)
                        {
                        for(th=0;th<HOLO_th;th++)
                        {
                                sinth=cos((th)*3.141592654/2./(HOLO_th-1));
                                costh=sin((th)*3.141592654/2./(HOLO_th-1));
                        for(x=-MODEL_X;x<=MODEL_X;x++)
                        {
                                rx=LconstX*(x+0.5);
                        for(y=-MODEL_Y;y<=MODEL_Y;y++)
                        {
                                ry=LconstY*y;
                        for(z=-MODEL_Z;z<=MODEL_Z;z++)
                        {
                                        rz=LconstZ*(z+0.5);
```

Table D.6 'Obj2Ptn' Subroutine Continued

```
        r=sqrt(rx*rx+ry*ry+rz*rz);
        if (r>RANGE_S&&r<RANGE_L) {
        sindelta=sqrt(pow(rx/r-costh*cosphi,2)+pow(ry/r-
                        costh*sinphi,2)+pow(rz/r-sinth,2))/2.;
        lorenze=(1+pow(rx/r*costh*cosphi+ry/r*costh*sinphi+rz/r*sinth,2))/2.;
        AFS=12.0658;
        AFS+=16.8819*exp(-0.4611*pow(K_eng[k]/2./3.14159265*sindelta,2));
        AFS+=18.5913*exp(-8.6216*pow(K_eng[k]/2./3.14159265*sindelta,2));
        AFS+=25.5582*exp(-1.4826*pow(K_eng[k]/2./3.14159265*sindelta,2));
        AFS+=5.8600*exp(-36.3956*pow(K_eng[k]/2./3.14159265*sindelta,2));
        Holo[phi][th][k]-=cos(K_eng[k]*(r-rx*costh*cosphi-ry*costh*sinphi-
                        rz*sinth))/r*(AFS)*erfc(r/500000.-3)*lorenze;
        }
}
}
}
}
}
        /***********************************************/
```

Table D.6 is the numberical subroutine 'Obj2Ptn' that calculates the holograph. The algorithm calculates scatter waves for each individual atom on each holograph mesh grid. Different processors are allocated different regions of phi values that are to be simulated. 'fold_i' is the number of phi mesh grids that each processor has to simulate.

The more processors available, the fewer phi mesh grid points have to be simulated in each processor.

APPENDIX E

ALGORITHM FOR FAST SPHERICAL HARMONIC EXPANSION USING SPHEREPACK 3.0

The simulated holograms are expanded in spherical harmonic coefficients using SPHEREPACK 3.0 [136].

Table E.1 Variable Definition Block for 'test1' Program

```
      program test1
      parameter (idp=1801)
      parameter (kdp=3600)
      parameter (lwshp=2*(idp+1)**2+kdp+20,
     1                  liwshp=4*(idp+1),lwrk=1.25*(idp+1)**2+7*idp+8)
      parameter (lwrk1=idp*kdp)
      parameter (lwork = 5*idp*(idp-1),
     1                  lwsha=idp*(idp+1)+3*(idp-2)*(idp-1)/2+kdp+15)
      double precision work(lwrk)
      dimension sx(idp,kdp),sy(idp,kdp),
     1                  wshp(lwshp),iwshp(liwshp),wrk1(lwrk1)
      dimension g(idp,kdp,2),ga(idp,idp,2),gb(idp,idp,2),
     1                  gh(idp,kdp,2),gw(idp,kdp,2),
     2                  wrk2(lwork),wshaec(lwsha),wshsec(lwsha)
            real  r,shia(idp,idp),shib(idp,idp),xua(idp,idp),xub(idp,idp)
      dimension t1(2)
      parameter (mode= 0) ! this is operation mode of spherical harmonics
      parameter (pi = 3.14159265358979323846264338327950 )
      real  E,k0E
      integer nlat,nlon,nt
      common /EKE/ E,k0E,nlat,nlon
```

The SPHEREPACK sample ‘test1’ program is modified to perform spherical harmonic expansion on simulated holographs. Table E.1 is the variable definition block for ‘test1’ program. Most of the variables are defined and used in the spherical harmonic algorithm utility and one does not have to specify the meaning of the variables, as they are self-explanatory. Exceptions are the ‘g(idp,kdp,2)’ array which stores the holograph to be expanded, the ‘ga(idp,idp,2)’ and ‘gb(idp,idp,2)’ arrays which store the results of spherical harmonic expansion.

Table E.2 Algorithm in ‘test1’ Program

```
        call load2d(idp,kdp,g(1:idp,1:kdp,nt))


        write(*,*) 'Program test1, Energy=',E,k0E
        write (*,5) mode,nlat,nlon
5       format(' mode =' ,i5,'  nlat =',i5,'  nlon =',i5)
        pause

        call shaeci(nlat,nlon,wshaec,lwsha,work,lwrk,ierror)
        if(ierror .ne.  0) write(*,70) ierror
70      format('   ierror0' ,i5)


        call shaec(nlat,nlon,mode,nt,g,idimg,jdimg,ga,gb,idimg,idimg,
1                       wshaec,lwsha,wrk2,lwork,ierror)
        if(ierror .ne.  0) write(*,72) ierror
72      format('   ierror2' ,i5)

        call save2d(200,200,Real(ga(1:200,1:200,nt)))
        call save2d(200,200,Real(gb(1:200,1:200,nt)))
        pause
```

The algorithm block is shown in Table E.2. First the holograph is loaded into ‘g(idp,kdp,2)’ array, then the ‘shaeci’ function is called to prepare spherical decomposition. The ‘shaec’ function does the work of spherical decomposition; and, finally, the result in ‘ga(idp,idp,2)’ and ‘gb(idp,idp,2)’ arrays are stored in the file system.

Table E.3 and Table E.4 are subroutines that save and load a 2D array. Note that the data file format for holograph in ‘load2d’ function is different from the data file

format in the holograph simulation. A file format conversion is necessary before putting the holograph into the ‘load2d’ subroutine.

Table E.3 ‘save2d’ Subroutine

```
subroutine save2d(nlat,nlon,g)  ! 2D data save
        integer nlat,nlon
        real g(nlat,nlon),E,k0E
        common /EKE/ E,k0E
        open(2,file='')
        write(2,*) nlat, nlon,E
        k0E =   0.5067738826929*E
        do i = 1,nlat
        do j = 1,nlon
                write(2,*) i,j,g(i,j)
        end do
        end do
        CLOSE(2)
        end subroutine save2d
```

Table E.4 ‘load2d’ Subroutine

```
subroutine load2d(idp,kdp,g)  ! 2D data load
        integer i,j,nlat,nlon,idp,kdp
        real g(idp,kdp),E,k0E,nlat_,nlon_
        common /EKE/ E,k0E,nlat,nlon
        open(2,file='')
        read(2,*) nlat_,nlon_,E
        k0E =   0.5067738826929*E
        nlat=INT(nlat_)
        nlon=INT(nlon_)
        if(nlat.gt.idp.or.nlon.gt.kdp) then
        write (*,*) 'Oops! Holograph size too large!'
        pause
        endif
        do i = 1,nlat
        do j = 1,nlon
                read(2,*) nlat_,nlon_,g(nlat_,nlon_)
        end do
        end do
        CLOSE(2)
        end subroutine load2d
```

APPENDIX F

ALGORITHM FOR MATRIX CALCULATION FOR SPHERICAL HARMONIC ANALYSIS

The matrix of spherical harmonic analysis is given by:

$$c_{lm} = \sum_{h} \left[\frac{16\pi^2 i^l r_e}{2l+1} Y^*_{lm}(\theta_h, \varphi_h) \int j_l(hr) \mathrm{Re}\left(e^{ikr} S_l(kr)\right) \mu(r) r dr \right] \rho(\vec{h})$$

The algorithm that calculates matrix element $\frac{16\pi^2 i^l r_e}{2l+1} Y^*_{lm}(\theta_h, \varphi_h) \int j_l(hr) \mathrm{Re}\left(e^{ikr} S_l(kr)\right) \mu(r) r dr$ is modified from the same 'test1' program. The modified program uses the same variable definition block and 'save2D' and 'load2d' blocks as shown in Table E.1, Table E.3 and Table E.4.

The numerical calculation part of the algorithm is shown in Table F.1. First it loads in the sample k-space structure file with 'load2d' function (Table E.4). Then Simpson integration of each individual *l* and structure factor is performed. The integrand of the integration is stored in the 'J_S_rExp' subroutine that is shown in Table F.2.

The calculated integration is then saved to the file system with the 'save2d' function (Table E.3)

Table F.1 Algorithm that Calculates Matrix Element in Spherical Harmonic Analysis

```
! Load structure file for structure simulation
        call load2d(Nhspace,Hspace(:,1:5))


        write(*,*) 'Program test1, Energy=',E
        write (*,5) mode,nlat,nlon
5       format(' mode =' ,i5,'  nlat =',i5,'  nlon =',i5)
        pause
!simulate Matrix by integration
!*****************************************************************
        do n=1, NHspace
        do l =1,99
        if(Hspace(n,4).ne.Hspace(n-1,4).or.n==1) then
        write(*,*) n,l
        call simpsn(J_S_rExp,l-1,Hspace(n,4),k0E
1                       ,0.05*l,50.0,0.01,1500,g(1,l,2))
        end if
        do m = 1, 1
        g(2,l,2)=g(1,l,2)*(4*pi)**2/(2*l-1)
1                       *plgndr(l-1,m-1,Hspace(n,3)/Hspace(n,4))
        ga(m,l,2)=g(2,l,2)*cos((pi-Hspace(n,5))*(m-1))
        gb(m,l,2)=g(2,l,2)*sin((pi-Hspace(n,5))*(m-1))
        Hspace(n,10+l*(l-1)/2+m)  = ga(m,l,2)
        Hspace(n,5000+l*(l-1)/2+m) = gb(m,l,2)
        end do
        end do
        enddo


        call save2d(Nhspace,10000,Hspace(1:Nhspace,1:10000))
```

Table F.2 'J_S_rExp' Subroutine that Represents Integrand

```
      real function J_S_rExp(l,h,k,ri)
      real h,k,ri
      integer l
      REAL, AUTOMATIC :: J0,Y0,J1,Y1,J2,Y2,J3,Y3,J4,Y4
            call sphbes(l,k*ri,J1,Y1)
            J1=(2*l+1)*J1
            Y1=J1*(-k/ri)                                  !near field
            J1=J1*(1./ri**2+k**2)                          !near field
            call sphbes(l,k*ri,J2,Y2)
            J2=((l+1)**2/(2*l+3)+l**2/(2*l-1))*J2
            Y2=J2*(3*k/ri)                                 !near field
            J2=J2*(-3./ri**2+k**2)                         !near field
            call sphbes(abs(l-2),k*ri,J3,Y3)
            J3=-l*(l-1)/((2*l-1))*J3
            Y3=J3*(3*k/ri)                                 !near field
            J3=J3*(-3./ri**2+k**2)                         !near field
            call sphbes(l+2,k*ri,J4,Y4)
            J4=-(l+1)*(l+2)/(2*l+3)*J4
            Y4=J4*(3*k/ri)                                 !near field
            J4=J4*(-3./ri**2+k**2)                         !near field
            call sphbes(l,h*ri,J0,Y0)
      J_S_rExp=J0*ri*exp(-0.0001*ri**2)*CMPLX(cos(k*ri),sin(k*ri)))
1                 *real(CMPLX(J1+J2+J3+J4,Y1+Y2+Y3+Y4)
      return
            end function J_S_rExp
```

APPENDIX G

PROCEDURE FOR A COMPLETE SPHERICAL HARMONIC SIMULATION

A complete spherical harmonic simulation takes many steps in many different environments. A summary of the procedure is given here:

- Run MPI program on Kong cluster to simulate hologram.
- Run spherical harmonic expansion program to transform the simulated holograph into its spherical harmonic coefficents.
- Run matrix calculation program to produce the matrix file.
- Run the Matlab script that sovle the matrix equation.

REFERENCES

1. Gabor, D., Microscopy by recorded wavefronts. Proc. R. Soc., 1949. 197 p. 454.

2. Odelberg, W., ed. Les prix nobel en 1971. 1972, Nobel Foundation: Stockholm.

3. Denisyuk, Y.N., On the reflection of optical properties of an object in a wave field of light scattered by it. Doklady Akademii Nauk SSSR., 1962. 144 p. 1275-1278.

4. Leith, E.N. and J. Upatnieks, Reconstructed wave fronts and communication theory. J. Opt. Soc. Am., 1962. 52 p. 1123.

5. http://en.wikipedia.org/wiki/Holography, Holography from Wikipedia. 11/10/2011.

6. Francon, M., ed. Holography. 1969, Academic Press, Inc.: New York.

7. Smith, H.M., ed. Principal of holography. 1969, Wiley Interscience: New York.

8. Soroko, L.M., ed. Holography and coherent optics. 1980, Plenum Press: New York.

9. http://www.fou.uib.no/fd/1996/h/404001/kap02.htm, Holographic methods. 11/10/2011.

10. Denisyuk, Y.N., Optika i Spektroskopiya 1963. 15 p. 522.

11. Phillips, N.J. and D. Porter, An advance in the processing of holograms. Journal of Physics E: Scientific Instruments, 1976 p. 631.

12. Dyson, J. and M.E. Haine, A modification to Gabors proposed diffraction microscope. Nature, 1950. 166 p. 315.

13. Parrent, G.B. et al., A readout technique for the laser fog disdrometer. J. Appl. Meteorol, 1966. 55 p. 343.

14. Hart, R.G., Electron microscopy of unstained biological material: the polytrophic montage. Science 1968. 159 p. 1464.

15. Harp, G.R. et al., Atomic-Resolution Electron Holography in Solids with Localized Sources. Phys. Rev. Lett., 1990. 65 p. 1012.

16. Unwin, P.N.T. and R. Henderson, Molecular structure determination by electron microscopy of unstained crystalline specimens. J. Mol. Biol., 1968. 94 p. 425.

17. Midgley, P.A. and R.E. Dunin-Borkowsk, Electron tomography and holography in materials science. Nature Materials, 2009. 8 p. 271

18. Cowley, J., Twenty forms of electron holography. Ultramicroscopy, 1992. 41 p. 335-348.

19. Midgley, P.A., An introduction to off-axis electron holography. Micron 2001. 21 p. 167.

20. Holographic studies on magnetic phenomena in small regions. 1995, Electron Holography Elsevierm: Amsterdam.

21. Tonomura, A., Direct observation of thitherto unobservable quantum phenomena by using electrons. Processings of the National Academy of Science, 2005. 102 p. 14952.

22. Szoeke, A., ed. In short wavelength coherent radiation: Generation and application. 1986, American Institute of Physics: New York.

23. Barton, J.J., Photoelectron holography. Phys. Rev. Lett., 1988. 61 p. 1356.

24. Leibsch, A., Theory of angular resolved photoemission form adsorbates. Phys. Rev. Lett., 1974. 32 p. 1203.

25. Saldin, D.K. et al., Holographic LEED. Phys. Rev. Lett., 1990. 64 p. 1270.

26. Fink, H.W. et al., Holography with low-energy electrons. Phys. Rev. Lett. , 1990. 65 p. 1204.

27. Li, H. et al., Direct experimental identification of the structure of ultrathin films of bcc iron and metastable bcc and fcc cobalt. Phys. Rev. B 1989. 40 p. 10241.

28. Harp, G.R. et al., Scanned-angle x-ray photoemission holography with atomic resolution. Phys. Rev. B 1990. 42 p. 9199.

29. Tong, S.Y. et al., Method for spatially resolved imaging of energy-dependent photo-electron diffraction. Phys. Rev. B, 1992. 46 p. 2452.

30. Thevuthasan, S. et al., Electron emission holography at kev energies: Estimates of accuracy and limitations. Phys. Rev. Lett., 1991. 67 p. 469.

31. Hardcastle, S. et al., X-ray photoelectron holography of ultrathin film and single crystal Cu(111): improving the accuracy of bond-length determination. surf. sci., 1991. 245 p. L190.

32. Tong, S.Y. et al., Phase-shift correction in there-dimensional imaging using forward-scattering photoemission and auger spectroscopy. Phys. Rev. Lett., 1991. 66 p. 60.

33. Tonner, B.P. et al., Scattered-wave intergral-transfrom method of holographic-image reconstruction form forward-scattering diffraction patterns. Phys. Rev. B, 1991. 43 p. 14423.

34. Saldin, D.K. et al., Theoretical principles of holographic crystallography. Phys. Rev. B, 1991. 44 p. 2480.

35. Saldin, D.K. et al., Concentric-shell algorithm for auger and core-level photoelectron diffraction: Theory and applications. Phys. Rev. B 1993. 48 p. 8234.

36. Tegze, M. et al., Atomic-resolution x-ray holography. Europhys. Lett. , 1991. 16 p. 41.

37. Len, P.M. et al., Atomic imaging by x-ray fluorescence holography and electron-emission holography: A comparative theoretical study. Phys. Rev. B 1994. 50 p. 11275.

38. Tegze, M. and G. Faigel, X-ray Holography with atomic resolution. Nature, 1996. 380 p. 49.

39. Gog, T. et al., Multiple-Energy X-Ray Holography: Atomic Images of Hematite (Fe2O3). Phys. Rev. Lett., 1996. 76(17) p. 3132.

40. Tegze, M. et al., Imaging light atoms by x-ray holography. Nature, 2000. 407 p. 38.

41. http://11bm.xor.aps.anl.gov/absorb/absorb.php, Compute X-ray Absorption. 11/10/2011.

42. Omori, S. et al., Resonant x-ray fluorescence holography: Three-dimensional atomic imaging in true color. Phys. Rev. B, 2001. 65 p. 014106.

43. Takahashi, Y. et al., Complex x-ray holography. Phys. Rev. B, 2003. 68 p. 052103.

44. Korecki, P. et al., Extinction effects in x-ray holographic imaging with internal reference. Phys. Rev. B, 2004. 69 p. 1841033.

45. Fanchenko, S.S. et al., Invalidity of low-pass filtering in atom-resolving x-ray holography. Phys. Rev. B, 2004. 66 p. 060104.

46. Faigel, G. et al.., Comment on ’invalidity of low-pass filtering in atom-resolving x-ray holography’. Phys. Rev. B 2004. 70 p. 106101.

47. Fanchenko, S.S. et al., Reply to "comment on 'invalidity of low-pass filtering in atom-resolving x-ray holography' ". Phys. Rev. B, 2004. 70 p. 106102.

48. Tegze, M., Effect of low-pass filtering on atomic-resolution x-ray holography. Phys. Rev. B, 2006. 73 p. 214104.

49. Kopecky, M. et al., X-ray absorption holography. Phys. Rev. Let. , 2002. 88 p. 185503.

50. Tegze, M. et al., Comment on ’x-ray absorption holography’. Phys. Rev. Let. , 2002. 89 p. 279601.

51. Bai, J., Atomic scattering factor for a spherical wave and near-field effects in x-ray fluorescence holography. Phys. Rev. B, 2003. 68 p. 144109.

52. Chukhovskii, F.N. et al., Electron charge density imaging with X-ray holography. Optics Communications, 2002. 209 p. 273.

53. Miller, G.A. et al.., Quantum electrodynamics of the internal source x-ray haplographies: Bremsstrahlung, fluorescence, and multiple-energy x-ray holography. Phys. Rev. B 1997. 56 p. 2399.

54. Len, P.M. et al., Multiple energies x-ray holography: Incident-radiation polarization effects. Phys. Rev. B, 1997. 56 p. 1529.

55. Kusano, S. et al., High sensitive imaging of atomic arrangement of ge clusters buried in a Si crystal by x-ray fluorescence holography. Jpn. J. Appl. Phys., 2006. 45 p. 5248.

56. Adams, B. et al., Atomic holography with x rays. Phys. Rev. B, 1998. 57(13) p. 7526.

57. Busetto, E. et al., X-ray fluorescence holography: A different approach to data collection. Phys. Rev. B, 2000. 62 p. 5273.

58. Matsushita, T. et al., A new approach for three-dimensional atomic-image reconstruction from a single-energy photoelectron hologram. Europhys. Lett. , 2004. 65 p. 207.

59. Takahashi, Y. et al., Reconstruction of atomic images from multiple-energy x-ray holograms of FePt films by the scattering pattern matrix method. Appl. Phys. Lett., 2005. 87 p. 234104.

60. Nishino, Y. et al., Two-energy twin image removal in atomic-resolution x-ray holography. Phys. Rev. B, 2002. 66 p. 092105.

61. Marchesini, S. et al., Direct 3d imaging of al70.4pd21mn8.6 quasicrystal local atomic structure by x-ray holography. Phys. Rev. Lett., 2000. 85 p. 4723.

62. Hayashi, K. et al., X-ray fluorescence holography of 0.078wt copper in silicon steel. Phys. Rev. B 2005. 63 p. 041201.

63. Lechner, P. et al., Pair creation energy and Fano factor of silicon in the energy range of soft X-rays. Nucl. Instrum. Methods Phys. Res. A 1996. 377 p. 206.

64. Takahashi, Y., K. Hayashi, and E. Matsubara, Development and application of laboratory x-ray fluorescence holography equipment. Advances in X-ray Analysis, 2004. 47 p. 110.

65. S. Marchesini, F.S., M. Tegze, G. Faigel, Y. Calvayrac, M. Belakhovsky, Direct 3D Imaging of Al70.4Pd21Mn8.6 Quasicrystal Local Atomic Structure by X-ray Holography. Phys. Rev. Lett., 2000. 85(22) p. 4723.

66. Hayashi, K. et al., Local-structure analysis around dopant atoms using multiple energy x-ray holography. Phys. Rev. B 2001. 63 p. 041201.

67. Chukhovski, F.N. et al., Electron charge density imaging with x-ray holograph. Optics Communications, 2002. 209 p. 273-277.

68. Matsushita, T., A. Agui, and A. Yoshigoe, A new approach for three-dimensional atomic-image reconstruction from a single-energy photoelectron hologram. Europhys. Lett., 2004. 65 p. 207.

69. Takahashi, Y. et al., Reconstruction of atomic images from multiple-energy x-ray holograms of FePt films by the scattering pattern matrix method. Appl. Phys. Lett., 2005. 87 p. 234104.

70. Nakamura, O. et al., Optical microscope tomography. ii. nonnegative constraint by a gradient-projection method. J. Opt. Soc. Am. A, 1988. 5 p. 554.

71. Hosokawa, S. et al., Existence of tetrahedral site symmetry anout Ge atoms in a single-crystal film of ge2 sb2te5 found by x-ray fluorescence holography. Appl. Phys. Lett., 2007. 90 p. 131913.

72. Hayashi, K. et al., 3d atomic imaging of SiGe system by x-ray fluorescence holography. Journal of Material Science, 2003. 14 p. 459.

73. Hayashi, K. et al., X-ray fluorescence holography of 0.078wt copper in silicon steel. Phys. Rev. B, 2005. 63(1-4) p. 041201.

74. Hosokawa, S., N. Happo, and K. Hayashi, Reconciling the Pauling bond length picture and Vegard's law in a mixed crystal: An x-ray fluorescence holographic study. Phys. Rev. B, 2009. 80 p. 134123.

75. Hu, W. et al., Phase transition in Ti50Ni44Fe6 studied by x-ray fluorescence holography. Phys. Rev. B, 2009. 80 p. 060202.

76. Hosokawa, S., et al., X-ray fluorescence holography of In1-xGaxSb mixed crystal. Journal of Crystal Growth, 2009. 311 p. 978.

77. Happo, N. K. Hayashi, and S. Hosokawa, Atomic image around Mn atoms in diluted magnetic semiconductor Cd0.6Mn0.4Te obtained from X-ray fluorescence holography. Journal of Crystal Growth, 2009. 311 p. 990.

78. Happo, N. et al., Lattice distortions in γ-ray detector material Cd0.96Zn0.04Te probed by Zn Kα X-ray fluorescence holography. Journal of Electron Spectroscopy and Related Phenomena, 2010. 181 p. 154.

79. Happo, N. et al., Local Structure around Mn Atoms in IV-VI Ferromagnetic Semiconductor Ge0.6Mn0.4Te Investigated by X-ray Fluorescence Holography. Jpn. J. Appl. Phys., 2011. 50 p. 05FC11.

80. Hayashi, K. et al., Three Dimensional Local Structure Analysis of ZnSnAs2:Mn by X-ray Fluorescence Holography. Jpn. J. Appl. Phys., 2011. 50 p. 01BF05.

81. http://science.hq.nasa.gov/kids/imagers/ems/xrays.html, X-rays. 11/10/2011.

82. Rutherfordand, E. and H. Geigerg, An electrical method of counting the number of - particles from radio-active substances. Proc. R. Soc., 1908. 81 p. 141.

83. http://library.thinkquest.org/C0126323/measure.htm, Measuring radiation. 11/11/2011.

84. Akimov, Y.K. et al.., I.Sov. Phys. JETP, 1965. 21.

85. Dearnaley, G. and D.C. Northrop, eds. semiconductors for nuclear radiation. 1963, Spon: London.

86. Akimov, Y.K. et al., Semiconductor detectors for nuclear radiation and their application. Moscow: Atomizdat, 1967.

87. Akimov, Y.K. et al.., Semiconductor detectors in experimental physics. Moscow: Energoatomiz-dat, 1989.

88. Akimov, Y.K., Silicon radiation detectors. Instruments and Experimental Techniques 2007. 50 p. 5-34.

89. http://nsspi.tamu.edu/nsep/courses/basic-radiation-detection/semiconductor-detectors/introduction/introduction, semiconductor detectors. 11/11/2011.

90. Lechner, P. et al., Ionization statistics in silicon x-ray detectors - new experimental results. Nucl. Instr. and Meth. in Phys. Res. A, 1995. 354 p. 464.

91. Fiebiger, J.R. and R.S. Muller, Pair-Production Energies in Silicon and Germanium Bombarded with Low-Energy Electrons. J. Appl. Phys. , 1972. 43 p. 3202.

92. Pehl, P.H. et al., Accurate determination of the ionization energy in semiconductor detectors. Nucl. Instr. and Meth., 1968. 59 p. 45.

93. Klein, C.A., Bandgap Dependence and Related Features of Radiation Ionization Energies in Semiconductors. J. Appl. Phys., 1968. 39 p. 2029.

94. Lutz, G., ed. Semiconductor radiation detectors. 1999, Springer-Verlag Berlin Heidelberg.

95. Leo, W.R., ed. Techniques for nuclear and particle physics experiments. 1994, Springer: Berlin, Heidelberg, New York.

96. Taylor, J.M., ed. Semiconductor particle detectors. 1963, Butter Worths: London.

97. Mayer, J.W., Performance of germanium and silicon surface barrier diodes as alpha particle spectrometers. J. Appl. Phys., 1959. 30 p. 1937.

98. Miller, G.L. et al., eds. Bell Laboratory-Brookhaven National Laboratory Report 1960, Brookhaven National Lab.: New York. 4662.

99. Jackson, R.S., Improvements in Encapsulated Silicon Junction Alpha Detectors. IEEE Transactions on Nuclear Science, 1961. 8 p. 29.

100. Love, T.A., Proc. Inst. Radio Engrs NS 1961. 8 p. 91.

101. Slrode, A.C., Proc. Inst. Radio Engrs NS 1961. 8 p. 59.

102. Beutenmuller et al., Silicon position sensitive detectors for the Helios(Na34) experiment. Nucl. Instr. and Meth., 1987. A253 p. 500-510.

103. Hoira, A.L., Study of the asymmetrical response of silicon surface barrier detectors to mev light ions. Application to the precise analysis of light ions energy spectra i: helium ions. Nucl. Instr. and Meth. in Phys. Res. A, 1984. 223 p. 336.

104. Gujrathi, S.C. et al., Heavy-ion energy resolution of ssd detectors. Nucl. Instr. and Meth. in Phys. Res. B, 1990. 45 p. 275.

105. Cywiak, M., Surface barrier detector device and its application to alpha spectroscopy. J. Radio. Nucl. Chem. Lett., 1988. 126 p. 145-151.

106. Canberra Industries, I., ed. X-pips detector datasheet. 2010, Canberra Industries, Inc. : Meriden, CT.

107. Spieler, H., ed. Semiconductor detector systems. 2005, Oxford University Press: Oxford, UK.

108. Handkiewicz, A., ed. Mixed-signal systems. 2001, Springer-Verlag Berlin Heidelberg.

109. Geronimo, G.D. et al.., Analog cmos peak detect and hold circuits. part 1. Analysis of the classical configuration. Nucl. Instrum. Methods Phys. Res. A 2001. 484 p. 533-543.

110. Geronimo, G.D. et al.., Analog cmos peak detect and hold circuits. Part 2. the two phase o set-free and derandomizing configuration. Nucl. Instr. and Meth. in Phys. Res. A, 2001. 484 p. 544-556.

111. http://www.tpub.com/neets/tm/111-4.htm, Avalanche Photodiodes. 11/11/2011.

112. PerkinElmerInc., ed. Avalanche photodiodes: a user's guide. 2010, PerkinElmer Inc.: Waltham MA.

113. Smith, W.S.B.G.F., Charge coupled semiconductor device. Bell Syst. Tech. J., 1970. 49 p. 587.

114. Corporation, A.D.S., ed. ADSC product specifications. 2010, Area Detector Systems Corporation: San Diego.

115. Gatti, E. and P. Rehak, Semiconductor drift chamber — An application of a novel charge transport scheme. Nucl. Instr. and Meth. in Phys. Res. A, 1984. 225 p. 608.

116. Lechner, P. et al., Silicon drift detectors for high count rate X-ray spectroscopy at room temperature. Nucl. Instrum. Methods Phys. Res. A, 2001. 458 p. 281.

117. Eggert, T. et al., Nucl. Instr. and Meth. , 2003. 512 p. 257.

118. Canberra Industries, I., ed. X-pips detector (sdd) datasheet. 2010, Canberra Industries, Inc.: Meriden, CT.

119. Belau, E. et al., Charge collection in silicon strip detectors. Nucl. Instr. and Meth. in Phys. Res. B, 1983. 214 p. 253.

120. Freudenreich, K., A Review of Silicon Detectors. Proceedings of the 7th International Conference on Advanced Technology, 2001 p. 103.

121. Conner, P.O. et al., Multichannel energy and timing measurements with the peak detector/derandomizer ASIC. Proc. 2004 Nuclear Science Symp. Rome Italy 2004 p. 138.

122. Software, C.S., ed. SPEC x-ray diffraction software, four-circle reference. 2000, Certified Scientific Software: Cambridge, MA.

123. USDigital.com, ed. E4P OEM optical kit encoder. 2007, USDigital.com: Vancouver, Washington.

124. Xu, G. et al., Anomalous phase in the relaxor ferroelectric Pb(Zn1/3Nb2/3)O3. Phys. Rev. B, 2004. 70 p. 064107.

125. Tegze, M. et al., Three Dimensional Imaging of Atoms with Isotropic 0.5 Å Resolution. Phys. Rev. Lett., 1999. 84(24) p. 4847.

126. Feng, L. et al., VORTEXTM - A New High Performance Silicon Multicathode Detector for XRD and XRF Applications. Hard X-ray and Gamma-ray Detector Physics V, Proceedings of SPIE, 2004. 5198 p. 103.

127. Siddons, D.P. ed. Operating manual for HERMES-based photon-counting silicon microstrip detectors. 2006, NSLS: Upton, NY.

128. Geronimo, G.D. et al., Development of a High-Rate High-Resolution Detector for EXAFS Experiments. IEEE Transactions on Nuclear Science, 2003. 50(4) p. 885.

129. Marchesini, S. and C.S. Fadley, X-ray fluorescence holography: Going beyond the diffraction limit. Phys. Rev. B, 2003. 67 p. 024115.

130. Chukhovskii, F.N. and A.M. Poliakov, X-ray fluorescence holography: a novel treatment for crystal structure determination. Acta Crystallogr. Sect. A, 2003. A59 p. 109.

131. Chukhovskii, F.N. and A.M. Poliakov, Ab initio crystal structure determination using X-ray fluorescence holography for different noise levels: numerical simulation and analysis. Acta Crystallogr. Sect. A, 2004. A60 p. 82.

132. Warren, B.E., ed. X-ray Diffraction. 1969, Addison-Wesley Pub. Co.

133. Tegze, M. and G. Faigel, X-ray holography: theory and experiment. J. Phys.: Condens. Matter, 2001. 13 p. 10613.

134. Heise, B.H., Precision Determination of the Lattice Constant by the Kossel Line Technique. J. Appl. Phys., 1962. 33 p. 938.

135. Munoz, A. et al., Evolution of the Magnetic Structure of Hexagonal HoMnO3 from Neutron Powder Diffraction Data. Chem. Mater., 2001. 13 p. 1497.

136. ADAMS, J.C. and P.N. SWARZTRAUBER, SPHEREPACK 3.0: A Model Development Facility. Monthly Weather Review, 1998. 127 p. 1872.

137. Francis, J.G.F., The QR transformation, I. The Computer Journal, 1961. 4(3) p. 265.

138. Higham, D.J. and N.J. Higham, eds. MATLAB guide. 2005, SIAM: Philadelphia.

139. Cheney, E.W. and D.R. Kincaid, eds. Numerical mathematics and computing. 2007, Cengage Learning: London.

140. Wang, K.F., J.M. Liu, and Z.F. Ren, Multiferroicity: the coupling between magnetic and polarization orders. Adv. Phys., 2009. 58 p. 321.

141. Tikhonov, A.N., ed. Numerical methods for the solution of ill-posed problems. 1990, Kluwer Academic Publishers: London.

142. Vasin, V.V. and A.L. Ageev, eds. Ill-posed problems with a prior information. 1995, Utrecht: The Netherlands.